Silicon Nitride Membranes for Electrical and Thermal Transport Studies of Nanotubes

by

Gavi Elan Begtrup

B.S. (Western Kentucky University) 2002
M.A. (University of California, Berkeley) 2005

A dissertation submitted in partial satisfaction of the
requirements for the degree of
Doctor of Philosophy

in

Physics

in the

GRADUATE DIVISION
of the
UNIVERSITY OF CALIFORNIA, BERKELEY

Committee in charge:
Professor Alex Zettl, Chair
Professor Michael Crommie
Professor Roya Maboudian

Fall 2008

The dissertation of Gavi Elan Begtrup is approved:

Chair Date

Date

Date

University of California, Berkeley

Fall 2008

Silicon Nitride Membranes for Electrical and Thermal Transport Studies of Nanotubes

Gavi Elan Begtrup

Abstract

Silicon Nitride Membranes for Electrical and Thermal Transport Studies of Nanotubes

by

Gavi Elan Begtrup

Doctor of Philosophy in Physics

University of California, Berkeley

Professor Alex Zettl, Chair

There are many basic properties of carbon nanotubes that prove difficult to probe due to their small scale. For example, in order to investigate the geometry dependence of nanotube properties, one must concurrently measure both the precise dimensions and the properties of interest of individual nanotubes, which is a technologically challenging feat. We use a new approach to study the evolution of electrical and thermal transport properties of nanotubes, performing real time *in situ* measurements during high resolution transmission electron microscopy. This is accomplished by employing custom fabricated silicon nitride membrane supports, which we find to be a versatile and robust platform for the study of local properties of individual nanostructures. We have applied this technique to the study of the high bias electrical breakdown of multiwall carbon nanotubes, the role of facets of nanoparticle catalysts in carbon nanotube synthesis, and the electromigration of

metal encapsulated within a nanotube and its application as a multivalue archival memory device.

Professor Alex Zettl
Dissertation Committee Chair

To: Amber

Contents

List of Figures

List of Tables

Acknowledgments

First and foremost, I must thank my professor, Alex Zettl. He has provided some of the great imagination and insight that kept research interesting. He has been a constant source of research ideas, some of which we had time to explore. Above all, I thank Alex for supporting me in my endeavors outside the lab. I believe the Zettl lab will be a launching point for great things in both physics and the world beyond. Alex, I will fondly remember (most of) our trips together.

Thanks to Mike Crommie and Roya Maboudian for taking the time to read through my dissertation and sitting on my quals committee and not failing me. Also to Steven Louie who taught me almost everything I know about solid state physics and also not failing me on my quals.

I have had the pleasure of working with some wonderful people in the Zettl Lab. I would first like to thank those who worked directly on some of my projects. Keith Ray provided manpower for the original membrane projects and really helped get them off the ground. I have many memories of long and late hours with Keith in the dark and sleepy TEM room. Will Gannett is just beginning his PhD journey, but has already taken the reigns on the plethora of membrane projects yet to come. I enjoyed training him and wish him good luck. These two also had the distinct pleasure of reading through my entire dissertation and looking for errors for which I am grateful. I would also like to thanks the many other Zettl group members that I had the pleasure of working with through the years: Henry Garcia, Çağlar Girit, Kenny Jensen, Willi Mickelson, Shaul Aloni, Jannik Meyer, Kwan Kim, Benji Alemán, Andras Kis, David Okawa, Kris Erickson, Mattias Loster, and anyone else I may

have accidentally omitted.

I thank my predecessors for helping me get on track. Early help came from Masa Ishigami, of whom I cannot say enough. He helped me get started in this whole endeavor and even introduced me to a short lived sports career culminating in a national kayak polo championship silver medal. He is on his way up the rocky academic track, and I wish him luck. I also thank Adam Fennimore, who is, as they say, the salt of the earth. Adam is one of the nicest guys I know and smart and funny enough to make up for it. He did most of the hard work on these membrane projects and then dropped it on me to reap all the rewards. He was also smart enough to get a real job to support his army of little Fennimores. Adam knows what he values in life and embraces it. I envy him for that.

Brian Kessler deserves special mention as both a colleague and a bandmate. He was instrumental in understanding many of my projects, but we also collaborated outside the lab in the short-lived bands Tripod (with Benji Alemán) and The Electromagnates. Brian is smarter than he lets on, and I believe he has many tricks up his sleeves. I also had the pleasure of working with him on science policy white papers. He will do great things when he finds the right path.

When struggling to make sense of results, I benefitted greatly from the help of Tom Yuzvinsky. Tom is a great researcher who loves to tease meaning out of observation, great or small. I expect he will be successful in whatever field he ends up in, and I wish him luck should he pursue an academic track. He is a great guy whose friendship over these six years has helped make graduate school bearable. We have traveled the world together and faced death side-by-side more than once.

I would like to thank the members of the most awesome physics rock band of all time, The Thrillionaires. Jess Walter on drums, Ryan Prenger on the mic, Jake Siegel on the bass, and yours truly on guitar. An unforgettable line-up. Our shows and the making of our albums and our three and a half years rehearsing together were some of the happiest times of my life. Thank you also to the Thrillion Man Army, the legions of Thrillionaires fans who made performing so much fun. If it weren't for you, I'd just be a shirtless guy in leather pants.

Thank you to those at the Graduate Assembly, especially Josh Daniels, and to those at the American Physical Society Forum on Graduate Student Affairs. You helped open my eyes to a bigger picture.

Also thank you to Anne Takizawa for being helpful always.

I would like to thank my family for supporting me over the years. Thanks to Mr. Kitty for always being there for me and never judging me as long as there was food in his bowl. The same goes for little Mia.

Finally, I thank the one person who has stood by me even though she knows all my faults, my dearest wife Amber. You have kept me on track even when I wasn't sure which track to follow. This dissertation is dedicated to you, whether that's a compliment or not.

Part I

Introduction and Background

Chapter 1

Carbon Nanotubes

1.1 Introduction

Carbon nanotubes have fueled a nanomaterials revolution. They possess fascinating physical properties due to their intrinsic scale and sp^2 bonding. Their unique properties range from mechanical (high strengths), electrical (high current carrying capacity and tunable electronic structure), and thermal (high thermal conductivity) to chemical versatility. As we show in Chapter 5, this list can be extended to extreme thermal stability as well.

The combination of these properties has yielded a wide variety of potential and realized applications. These include field effect transistor devices as a long overdue replacement for silicon based structures and a horde of nanomechanical devices including the true realization of Richard Feynman's dream from his speech "There's plenty of room at the bottom"[1], the building of a nanoscale motor[2].

Although the properties of carbon nanotubes have been heavily studied since their

discovery in 1991[3], many fundamental questions still remain. These open questions relate to issues such as the electrical transport properties of multiwall carbon nanotubes, the mechanism of their wall by wall breakdown under high bias, their ultimate failure at high temperature, and even the simplest understanding of the role of catalyst particles in nanotube synthesis. The limit of our knowledge may be surprising in light of the incredible amount of interest in and funding for the field (especially since the creation of the National Nanotechnology Initiative), but is indicative of the immense wealth of underlying science at the nanoscale and the difficulty inherent in probing the properties of materials on such a small scale.

1.2 Physical Properties of Carbon Nanotubes

As mentioned previously, there are many interesting characteristics of carbon nanotubes (CNTs). As this introduction is not exhaustive, I recommend "Physical Properties of Carbon Nanotubes"[4], by Saito, Dresselhaus, and Dresselhaus, as a good beginning point for understanding the less disputed properties. I will focus on the properties that are relevant to the experiments described in this dissertation.

Carbon nanotubes can be most simply understood as a rolled up layer of graphene, the two-dimensional sheets that loosely bound together form graphite. This is illustrated in Figure 1.1. The result is a hollow nanometer-scale tube that maintains the hexagonal sp^2 configuration of carbon atoms. Carbon nanotubes are one of four common allotropes of carbon, the other three being graphite and fullerenes (both also sp^2 bonded) and diamond (sp^3 bonded).

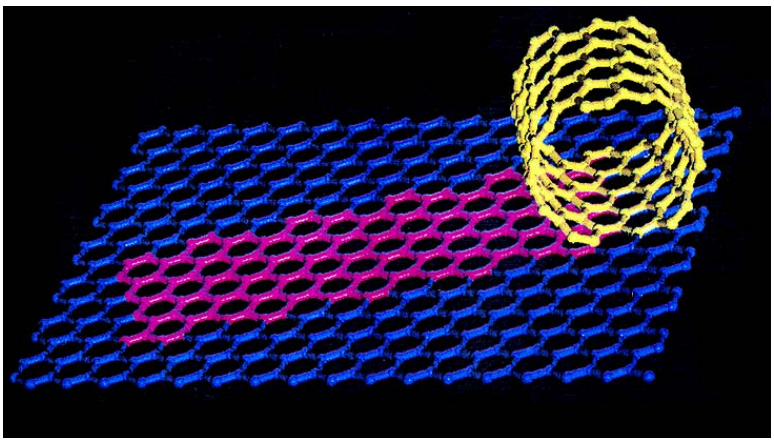

Figure 1.1: Conceptual Formation of a Carbon Nanotube From a Graphene Sheet

There are two basic categories of carbon nanotubes, single walled nanotubes (SWCNTs) and multiwall nanotubes (MWCNT). Although the abbreviation MWNT is sometimes found in the literature, we prefer the MWCNT to distinguish carbon nanotubes from other types of nanotubes, most notably their inorganic analogue, boron nitride nanotubes[5].

SWCNTs consist of a single graphene-based cylinder. The most fascinating aspect of SWCNTs is the strong dependence of their physical properties on the rolling vector (chirality). Beyond simple considerations of induced strain, the quantization of allowed k vectors caused by periodicity introduced from rolling determines the electrical properties of SWCNTs. A slight change in the chirality can create either a metallic nanotube with four ballistic channels or a small band gap semiconductor. In fact, defects can cause a change in chirality in an individual nanotube, forming an interesting junction between nanotubes with different electronic properties[6].

Semiconducting nanotubes are sensitive to electrical and chemical gating. Combined with high surface-to-volume ratio, this allows application as chemical sensors[7]. The

richness of the well established field of organic chemistry promises a wealth of chemical specific sensors. Additionally, the promise of semiconducting nanotubes as transistors has led to hundreds of publications, and has produced devices with the highest mobility values for any known semiconductor[8].

Similar to the analogy of a SWCNT to a single graphene layer, MWCNTs can be thought of as multiple graphene sheets rolled up to form many concentric carbon shells or walls. The number of walls can range from two, so-called double wall carbon nanotubes (DWCNT), to many with no theoretical limit on the maximum. Due to many interacting walls, and usually large diameter, MWCNTs do not generally share the electrical versatility of SWCNTs, with the possible exception of DWCNTs[9]. However, the properties of MWCNTs do depend on their geometry (e.g. diameter and number of walls). The interaction between nanotube walls and its effect on MWCNTs conduction is still debated.

1.3 Synthesis of Carbon Nanotubes

The strong dependence of the physical properties on chirality and diameter is generally described as an amazing 'feature' of carbon nanotubes. However, difficulty in controlling the chirality through synthesis poses the greatest challenge for implementation of nanotubes in many high tech applications.

Although control of carbon nanotube synthesis has not yet been perfected, SWCNTs are typically grown with diameters ranging from 1 - 2 nm. Large diameter SWCNTs can be synthesized, but are often not desirable as they do not possess the same strengths and electronic properties of smaller nanotubes. Small diameter nanotubes, down to the

theoretical limit of stability at 4Å, have also been observed[10] and may possess interesting properties such as superconductivity[11].

There are three typical methods of nanotube synthesis: laser ablation[12], arc discharge[13], and chemical vapor deposition (CVD)[14]. Laser ablation was explored for high yield synthesis but has largely lost popularity, likely due to the great expense and difficulty of operating the laser system. Arc discharge is favored for the high quality of MWCNTs, which can be produced without catalysts and therefore avoids transition metal contamination. Alternatively, SWCNTs can be synthesized with the introduction of metal catalysts[15]. CVD methods are favored for the scalability of the synthesis processes to produce high yield and the ability to grow aligned nanotubes directly on devices in controlled locations. In addition, there are many tunable parameters of CVD growth, such as growth temperature, catalyst, carbon feedstock, and the introduction of oxidizing and/or reducing gasses. These pararmeters allow more precise control of the product, creating on demand predominantly single, double, or multiwall nanotubes or nanotubes with encapsulated materials. Recent advances in CVD techniques have allowed the growth of incredibly long nanotubes[16], currently reaching centimeters with no theoretical limit. Millimeter high vertical forests of nanotubes have also bee produced[17]. Control over the CVD catalyst promises the greatest possibility of controlling nanotube chirality.

1.4 Applications of Carbon Nanotubes

Carbon nanotubes have many potential applications, including transistors[18], light sources[19], electron field emitters[20] and displays[21], chemical sensors[7], rotational

actuators (motors)[2], high frequency and tunable resonators[22, 23, 24], mechanical memory elements[25], etc. These are only some of the 'high tech' applications, not including their use in polymers and materials. Due to their intrinsic size and variety of properties, carbon nanotubes are beginning to show promise in an entirely new field, that of the intersection of nanotechnology, biology, and medicine, so called "nano-bio" or "nano-medicine".

Chapter 2

Introduction to Previous *In Situ* Measurements

2.1 Introduction

As mentioned in Chapter 1, there are limits on our understanding of some fundamental properties of carbon nanotubes. Our understanding is limited primarily due to the difficulty of probing such small samples. Studies as simple as the thermal and electrical transport properties of nanotubes are complicated by the difficulty in addressing single nanotubes. Although experiments can be performed on ensembles of nanotubes, usually in the form of mats or bundles[26], these measurements probe only the average properties of CNTs, and cannot probe their most interesting properties, namely their chirality dependence. Additionally, devices made from such ensembles do not take full advantage of the high surface area of individual CNTs.

Although measurements of individual CNTs were eventually performed on MWCNTs[27, 28, 29] and SWCNTs[30, 31], a careful observer would have questioned the conclusion that these early studies were indeed performed on individual nanotubes. Unfortunately, none of the techniques used to image these nanotubes, atomic force microscopy (AFM), scanning electron microscopy (SEM), or focused ion beam microscopy (FIB) have resolution capable of discriminating between individual nanotubes and small bundles. Even if one were certain of the number of the nanotubes in these devices, there was no way to measure their chirality or even precisely measure their diameter. Therefore, the ultimate goal of confirming the link between nanotube geometry and physical properties was not possible.

Determining the chirality concurrent with other physical properties, such as electrical and thermal transport properties, of an individual nanotube is a difficult goal. Even unambiguously measuring the chirality of a CNT is nontrivial. Scanning tunneling microscopy (STM), for example, can be used to determine the chirality and, through spectroscopy, the local density of states of individual nanotubes[32], but requires a conducting substrate and is therefore difficult to combine with transport and other measurements on a single nanotube. Some progress in this direction has recently been made[33] but requires complicated device geometries that are not easily generalized. Recent advances in other forms of spectroscopy, such as Raman[34] and spectrofluorimetry[35] have shown promise for determining the chirality of nanotubes on a surface.

Another approach utilizes transmission electron microscopy (TEM), which is a powerful diagnostic tool for nanomaterials. TEM can be used to provide structural information via high resolution imaging and electron diffraction. TEM diffraction can pro-

vide enough information to directly determine the chirality of small diameter (<4nm) SWCNTs[36, 37] and DWCNTs[38]. Advances in aberration-corrected TEM have recently allowed the direct observation of carbon atoms in a nanotube lattice[39] and even the identification of topological defects[40, 41]. Such resolution provides unmistakable assignment of nanotube chirality.

Unlike any of the other imaging methods previously mentioned, TEM allows direct imaging through the sample, such that the internal structure of the nanotube can be determined. This is of particular use when studying MWCNTs, so that the multiple walls can be imaged, or when studying filled nanotubes, such as peapods[42] (fullerene filled CNTs) or metal encapsulated CNTs. Additionally, TEM imaging can be performed in real time, which is necessary for observation of transient behaviors.

Unfortunately, TEM is only possible on thin samples, and therefore cannot be performed on standard planar devices, such as typical CNT field effect transistors. The ultimate goal of our studies is to combine the high resolution capabilities of TEM with standard device geometries, as will be discussed herein.

2.2 Previous *In Situ* Measurements

There have been a few approaches to combining TEM with *in situ* transport and electromechanical measurements on nanotubes. These can be classified in three categories: nanomanipulation stages, microfabricated devices, and membranes. We have pioneered the use of silicon nitride membranes, as will be discussed in the following chapter.

2.2.1 Nanomanipulation Stages

The use of nanomanipulation stages inside the TEM has been explored by the Zettl group and specifically by John Cumings. These studies utilize an *in situ* piezo-driven manipulation stage to contact or otherwise address individual nanotubes. Typically a sample of nanotubes affixed to a wire is loaded in close proximity to the probe, which may be a sharp metallic tip similar to an STM tip, or a silicon cantilever (AFM tip) for performing force measurements. Both sides can be electrically contacted.

These manipulation stages can be used for a variety of studies, such as electrical and mechanical properties as well as the controlled engineering of nanostructures. Specifically, electrical tips in contact with nanotubes have been used to study the peeling and sharpening[43], linear friction[44], electrical resistance as a function of telescoping[45], and vacancy migration[46] in nanotubes as well as to create tunable nanoresonators[47]. Nanoscale mass transport devices have been fabricated with externally deposited[48] or encapsulated metals[49, 50]. Transport of encapsulated metals has also been used for nanotube zone refinement[51] and nanoscale soldering [52, 53]. With an electrical tip not in contact, field emission properties of nanotubes have been studied[54]. With an AFM tip, ultralow sliding friction in MWCNT walls has been explored carefully[55].

Such a wealth of studies has contributed greatly to the understanding of electromechanical properties in MWCNTs and has shown some promising applications. However, these studies can be of limited use for the study of electrical and thermal transport due to the poor quality of the contacts to the nanotube. On the sample side, the nanotube is generally connected to the source through bundles of other nanotubes that are themselves

poorly connected to a metallic wire. On the probe side, the nanotube is contacted by spot welding to the metal tip. These contacts are not ideal as they often offer high resistance and poor clamping. Due to bundling on the sample side it can be difficult to isolate the transport properties of a single nanotube. Additionally, the resolution of the TEM is hindered by vibrations of the sample. Finally, it is impossible to incorporate the nanotube into a device orientation, with the possible addition of electrical gates, heaters, thermometers, or actuators.

2.2.2 Microfabricated Devices

An alternative method to performing *in situ* TEM measurements on nanomaterials is the use of microfabricated support structures. Jannik Meyer has performed many experiments with undercut freestanding devices. These devices are fabricated on a chip that is cleaved near the device to facilitate etching of the supporting substrate. With this basic architecture, he has been able to create a torsional pendulum[56] that can be actuated by application of an electric field, similar to the nanomotor[2]. Additionally, he is able to identify the chirality of individual nanotubes via electron diffraction and correlate his results to Raman spectroscopy of the same nanotube[57].

Although electrical measurements were not performed *in situ*, Meyer was able to perform electrical transport measurements on a nanotube before suspending it, thereby finally reaching the goal of correlating transport properties unambiguously to chirality[58].

Jim Hone's group has developed a method of placing nanotubes, achieving the goal of "what we want, where we want it."[59] By growing long nanotubes across slits,

he is in principle able to characterize a single nanotube by any number of techniques, including Rayleigh scattering[60], Raman scattering, spectrofluorimetry, TEM, and electron diffraction. He can then controllably place the nanotube on a surface and proceed to wire it up for electrical characterization. Chirality measurement correlated with transport has been performed by Chandra et al.[61]

Although this technique is a great step in comparing many of the individual characterization methods for nanotubes, it requires suspension over large trenches that are not generally compatible with nanostructures. Additionally, none of these approaches allow *in situ* high quality electrical transport concurrent with TEM imaging and therefore cannot be used to measure transient behaviors of nanomaterials under electrical bias.

Chapter 3

Introduction to Silicon Nitride Membranes

3.1 Introduction

In situ measurements of nanostructures during TEM observation offer invaluable insight into many of their properties. Previous measurements have largely relied on nanomanipulation stages and have produced many interesting results. However, this approach faces certain limitations, such as the poor quality of electrical contacts, limited resolution due to vibration of the sample, and the difficulty of introducing gate electrodes or other useful probes. Additionally, it would be extremely difficult to apply this approach to such small samples as individual SWCNTs.

We have developed a different approach that addresses these issues, the use of custom fabricated thin silicon nitride membranes. These membranes allow high resolution

Figure 3.1: The *In Situ* Biasing Stage for the TEM
This stage was custom designed for the JEOL 2010 TEM. The inset shows four wires that contact the contact pads on the membrane. A replaceable blade allows eight contacts or other configurations as desired.

imaging inside a TEM and are compatible with standard lithographic techniques. Combined with a custom designed biasing stage (shown in Figure 3.1) for our JEOL 2010 TEM, the membranes allow real time electrical probing of nanostructures concurrent with TEM imaging. The membranes are very robust and can withstand many types of processing, such as reactive ion etching of holes in the membranes for higher resolution imaging or high temperature CVD growth of nanostructures directly on the membranes. Compatibility with electron beam lithography allows the fabrication of devices on the membrane that are nearly identical to typical planar devices, such as field effect transistors. In addition to high quality electrical contacts, any number of other devices could be integrated onto the membrane, such as microfabricated heaters and thermometers.

The silicon nitride membranes are an extremely versatile diagnostic tool. We have applied them to the study of the local thermal properties of the electrical breakdown of MWCNTs and the role of transition metal catalysts in carbon nanotube growth. Additionally, we have created a nanoparticle shuttle memory device that can be observed in real time. These experiments have only begun to scratch the surface of various measurements possible with these membranes.

3.2 Silicon Nitride

Silicon nitride is an attractive material for microfabriation as it can be easily processed in many ways. The dielectric can be deposited on silicon by chemical vapor deposition techniques, or on any material via sputtering. It can also be selectively etched with reactive ion etching or sculpted via ion milling or focused ion beam. This has led to the use of silicon nitride in many applications, such as sensors[62], stencils[63], nanosieves[64], and nanopores[65]. It is also used for atomic force microscope cantilevers due to the material's hardness.

Silicon nitride membranes are particularly useful for TEM studies, especially if combined with *in situ* electrical measurements, as discussed. Previous attempts at *in situ* transport measurements on silicon nitride membranes were limited, as functional electrical contacts were not achieved[66, 56]. Although silicon nitride membranes can be purchased commercially (e.g. from Structure Probe, Inc.) with membrane thicknesses as low as 20 nm, these membranes have historically been limited in their use for lithography as the membranes were too wide (typically 1 mm) and would tear during processing. However, 50 μm

wide (20 nm thick) silicon nitride membranes are now commercially available. These new membranes may be compatible with standard lithography and processing.

The early design of our silicon nitride membranes were made by Adam Fennimore and continued by Steve Konsek. These original membranes were somewhat unreliable and would often tear due to a flaw in the fabrication process, as discussed in Appendix A. However, they were sufficiently stable to be used in the initial experiments, outlined in Chapter 4.

3.3 Design

The full design and fabrication of the membranes is discussed in Appendix A. In brief, they consist of a thin silicon wafer with an oxide and thin (∼10 nm) nitride layer. The supporting silicon and oxide layers are selectively etched to release a freestanding window of silicon nitride that is ∼15 μm wide.

Commercial silicon nitride windows are available for use as TEM substrates, but are not robust enough to survive lithography and therefore cannot easily support electrical devices. Due to the small dimension of our membranes, they are extremely robust and handle many types of processing, including high temperature (limited by the melting of silicon at 1400°C), wet processing without the need for critical point drying (CPD), and multiple lithography steps.

Figure 3.3 shows how the membranes can be used for *in situ* electrical measurement of a nanotube in a TEM. The SEM image shows electrical contacts to nanotubes on the thin membrane (the dark region in the center). The inset shows a low magnification TEM

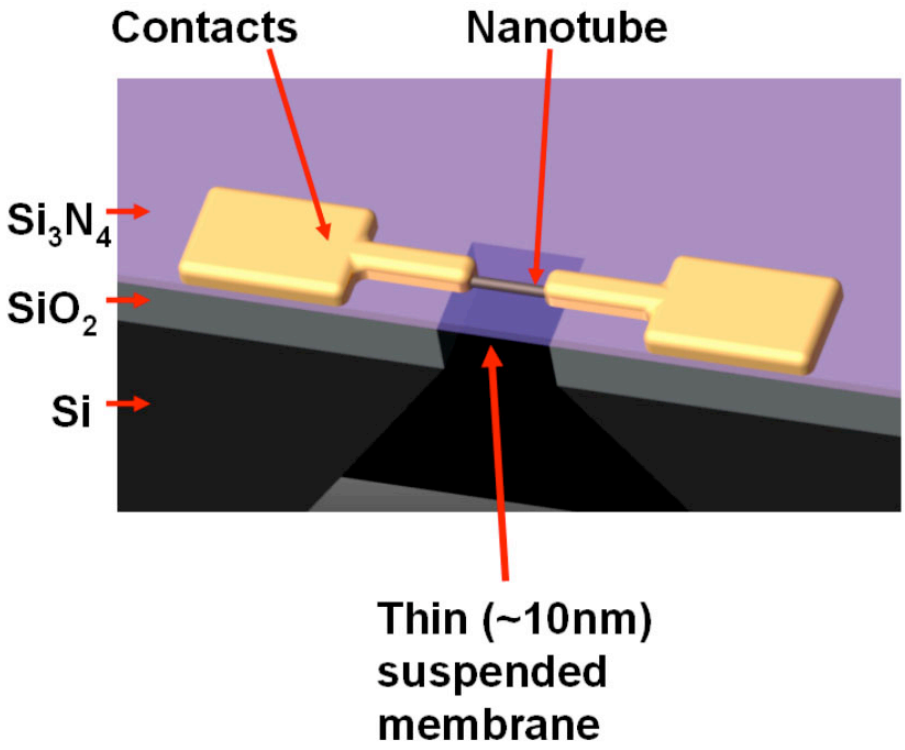

Figure 3.2: Artistic Schematic of Silicon Nitride Membrane
A suspended Silicon Nitride membrane shown with an electrically contacted nanotube device.

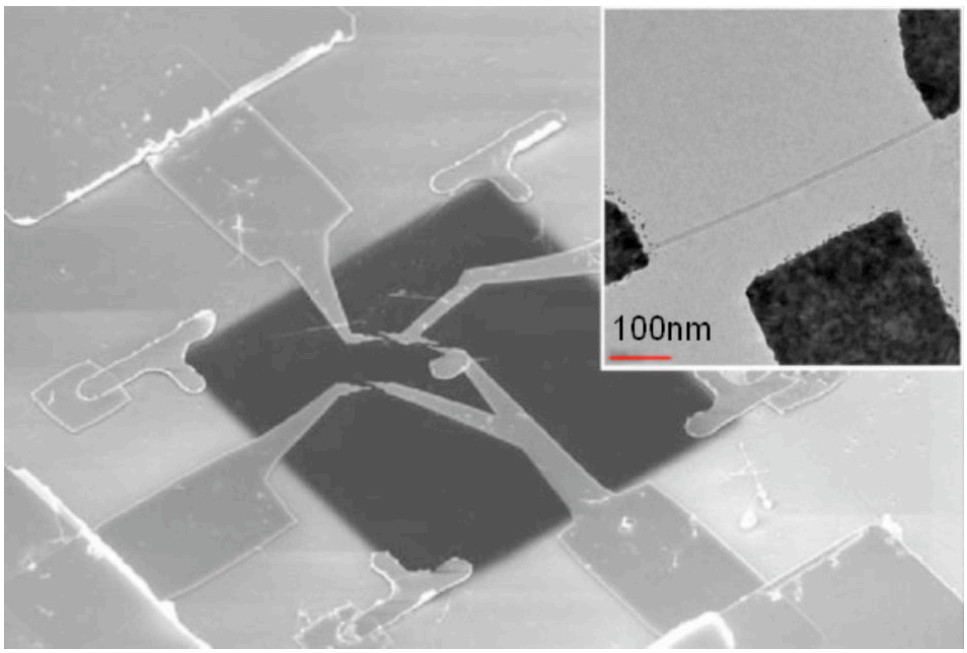

Figure 3.3: SEM and TEM of a Silicon Nitride Membrane Device
An SEM image of a silicon nitride membrane device. The membrane is ∼15 μm wide. The insert shows a TEM image of a nanotube device supported by a membrane. This is a three-terminal device, with a source, drain, and gate electrode.

image of a MWCNT device with two electrical contacts and a side gate electrode.

One of the great advantages of the silicon nitride membranes is their compatibility with high resolution TEM. Figure 3.4 below shows high resolution images of an indium nanoparticle and a MWCNT. Lattice fringes are clearly visible in the In particle. The individual walls of the MWCNT can be observed and counted. We are able to record high resolution images in real time using a video camera in the TEM. This allows the observation of real time effects, such as changes in state, movement, or breakdown of nanostructures.

For even higher resolution, holes of any shape and diameter (>∼10 nm) can be etched in the membranes via standard lithography and reactive ion etching. These devices are still compatible with lithography, but allow freestanding structures for unimpeded

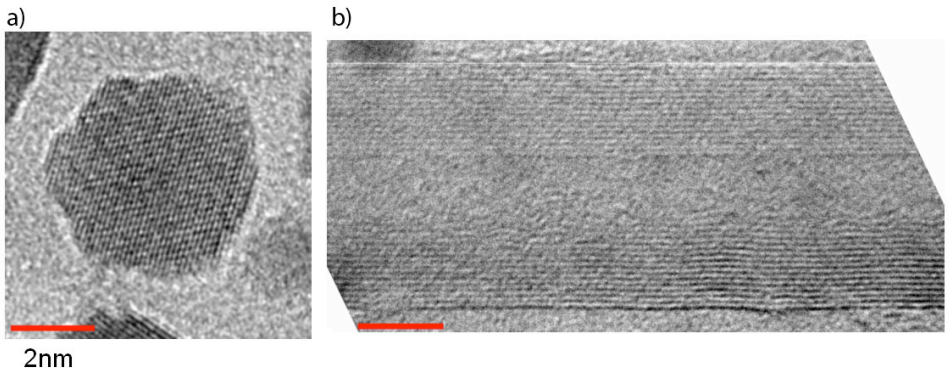

Figure 3.4: High Resolution Imaging of Nanostructures on a Silicon Nitride Membrane (a) An indium nanoparticle showing lattice fringes. (b) A MWCNT showing individual nanotube walls.

resolution as well as the study of mechanical properties.

Part II

In Situ Measurements of Multiwall Carbon Nanotubes

Chapter 4

Breakdown and Tailoring of Carbon Nanotubes

4.1 Introduction

We have performed two preliminary experiments utilizing the silicon nitride membranes for *in situ* electrical measurements of MWCNTs. Both focus on the high bias properties of nanotubes, specifically their electrical breakdown and the ability to engineer their geometry with applied bias and electron irradiation. These are detailed in the dissertation of Thomas Yuzvinsky, entitled "Carbon nanotubes for nanoscale electronics and nanoelectromechanical systems."[67]

4.2 Electrical Breakdown of MWCNTs

The electrical breakdown of MWCNTs was first reported by Collins et al.[68] High bias applied to a MWCNT caused the current through the nanotube to decrease in discrete steps. Atomic Force Microscopy (AFM) of the nanotube devices found coinciding thinning of the nanotube. It was assumed that the steps in the current corresponded to failure of individual nanotube walls and that each wall had a similar current carrying capacity, leading to equidistant steps. However, the mechanism for breakdown was unclear.

By measuring the transport properties of an individual MWCNT while observing it in real time in the TEM, we were able to show conclusively that each step in the current corresponded to the failure of an individual nanotube wall. However, the steps in the current were not generally observed to be equidistant. This could be explained by the observation that that the failed nanotube walls did not peel back completely from the center of the device and therefore still contributed to the current carrying capacity of the entire device. Their contribution at high bias was found to be related to their geometry, as would be expected for a classical metal wire. Precision control of the nanotube geometry can be achieved as the nanotube can be tailored by removing one wall at a time. These results are summarized in Figure 4.1 and detailed in the paper by Yuzvinsky et al.[69]

4.3 Shrinking a Carbon Nanotube

While exploring the high bias properties of nanotubes, we discovered the ability to control the diameter of an individual nanotube. The combination of electron irradiation

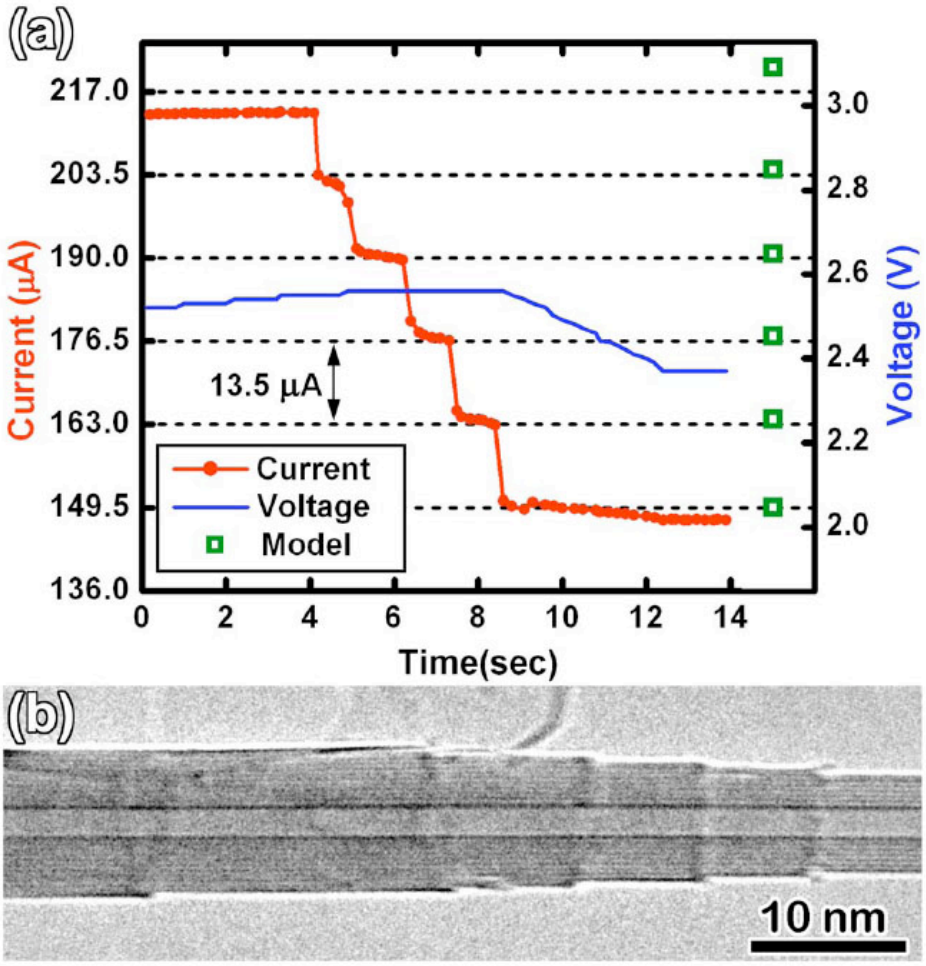

Figure 4.1: High Bias Wall-by-Wall Breakdown of MWCNTs[69]
(a) Steps in the current carrying capacity of the MWCNT caused by individual wall failure. The size of the steps can be understood by considering the resulting geometry of the nanotube. (b) High resolution TEM image showing wall breakdown.

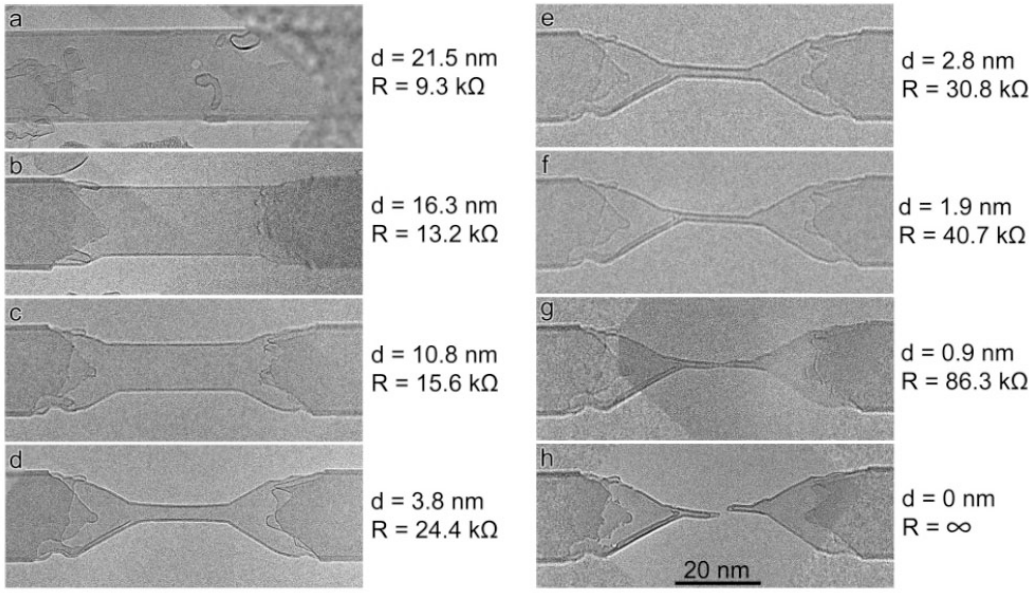

Figure 4.2: Shrinking a Carbon Nanotube[70]
. (a-e) Successive TEM images of a large diameter nanotube shrinking under electron irradiation and high bias. The process can be controlled and stopped by adjusting the bias, creating a nanotube with arbitrary diameter. The electrical properties are strongly dependent on the geometry.

induced defects, Joule heating, and electromigration causes a large diameter nanotube to continuously reform. The process can be controlled by adjusting the applied bias, and a nanotube of any diameter can be created. Consistent with our previous observations, the electrical transport properties of the nanotube are highly dependent on their geometry. As the diameter of the nanotube approaches zero, the system acts like a carbon chain and we observe negative differential resistance. These results are summarized in Figure 4.2 and detailed in the paper by Yuzvinsky et al.[70]

Chapter 5

The Extreme Thermal Stability of Carbon Nanotubes

5.1 Forward

Although wall-by-wall failure of MWCNTs had been observed (see Chapter 4, the failure mechanism had not been deduced. Many attributed this breakdown to oxidation, even though the effect was observed in vacuum as well as air. Knowledge of the temperature at which this effect occurred would be key to understanding the mechanism, but there existed no direct measurements of the temperature.

There was no consensus on the breakdown temperature, with some assuming that the breakdown occurred at 700°C, the approximate oxidation temperature of MWCNTs in air[71]. This assumption was not based on empirical observation, and I questioned it, especially since many of these breakdown experiments were performed in vacuum, not air.

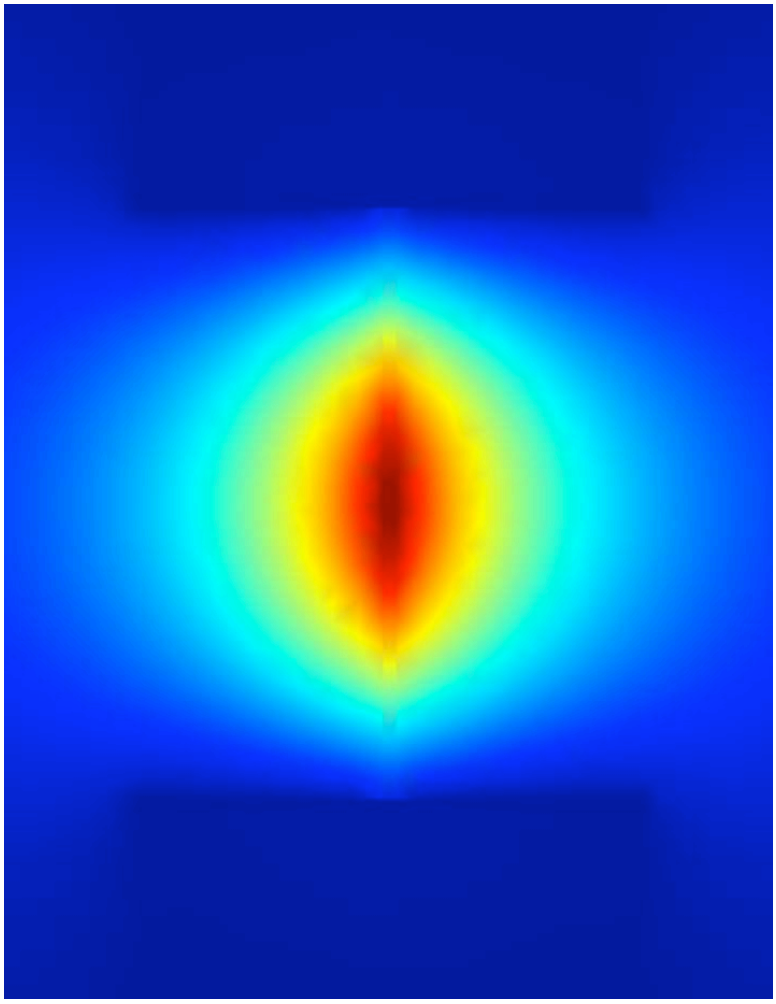

Figure 5.1: Simulation of the Temperature of a Nanotube Device

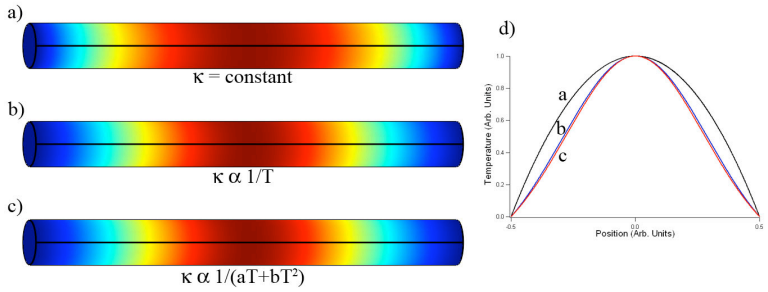

Figure 5.2: Effect of Temperature Dependence of Thermal Conductivity on Temperature Distribution
A cylinder is uniformly heated, as by Joule heating, and has thermal sinks at both ends. Three forms of the thermal conductivity are considered, (a) constant, (b) inversely proportional to T, and (c) inversely proportional to a function of T and T^2. The graph shows the temperature distribution along the cylinder. Note that the addition of temperature dependence of the thermal conductivity changes the shape of the temperature distribution.

This lack on understanding was a serious concern, as the interpretation of some experiments relied on these faulty numbers[72].

Much of this confusion was based on the original report of MWCNT breakdown by Phil Collins[68]. In this paper, the breakdown temperature was estimated based on a simple model of Joule heating with a static thermal conductivity. Unfortunately, the value of the thermal conductivity of carbon nanotubes is highly disputed, with estimates varying over many orders of magnitude. A greater problem, as is addressed in this chapter, is that thermal conductivity is not static but rather a function of temperature. Figure 5.2 illustrates the effect of temperature dependence of thermal conductivity on the thermal profile of a device. As a device heats, the thermal conductivity drops and thus the ability to dissipate heat is reduced. This results in the temperature peaking more sharply around hot spots.

In order to determine the temperature of MWCNT breakdown, we must be able

to measure the temperature of the nanotube locally on the nanoscale, as opposed to using a microfabricated thermometer located microns away. However, such a measurement is difficult to perform. We use a novel approach, employing gold nanocrystals as local thermometers on our thin membranes. This work was performed with the help of Keith Ray, Brian Kessler, and Tom Yuzvinsky. The MWCNTs used were synthesized by Henry Garcia.

5.2 Abstract

We report a novel nanoscale thermal platform compatible with extreme temperature operation and real-time high-resolution transmission electron microscopy. Applied to multiwall carbon nanotubes, we find atomic-scale stability to 3200 K, demonstrating that carbon nanotubes are more robust than graphite or diamond. Even at these thermal extremes, nanotubes maintain 10% of their peak thermal conductivity and support electrical current densities $\sim 2 \times 10^8 A/cm^2$. We also apply this platform to determine the diameter dependence of the melting temperature of gold nanocrystals down to three nanometers.

5.3 Introduction

The versatility of carbon-carbon bonding underpins a wealth of extraordinary physical properties. Of the two common allotropes of carbon, sp^3-bonded diamond is electrically insulating and displays exceptional hardness and thermal conductivity, but it is meta-stable and spontaneously reverts to graphite at elevated temperatures[73]. sp^2-bonded graphite is electrically conducting and very stiff in the sheet direction, but it sublimes at temperatures as low as 2400 K[74]. Carbon nanotubes, which can be grown with near

atomic perfection, capitalize on the extraordinary strength of the sp^2 hybridized carbon-carbon bond (one of the strongest in nature), and at room temperature exhibit phenomenal electrical and thermal conductivity as well as outstanding mechanical properties. Furthermore, theoretical studies[75] indicate that nanotubes should withstand extreme temperatures, perhaps as high as 4000 K.

Although theoretical studies suggest that nanotubes are surprisingly stable at thermal extremes, the breakdown temperature of MWCNTs in vacuum has not been directly determined[76, 77]. Although the temperature-dependent thermal conductivity κ of MWCNTs is well established below room temperature[78], κ in the extreme high-temperature limit remains largely unexplored.

Probing the thermal properties of nanoscale systems at very high temperature is technically challenging due to a variety of complications including the breakdown of supporting materials and calibration uncertainties. Something as seemingly straightforward as measuring local temperature becomes problematic on the nanoscale, especially at high temperature. We have developed a thermal test platform capable of operating at extreme temperatures while providing local temperature information with nanoscale resolution. We apply this platform to an investigation of the high temperature properties of MWCNTs and probe the limits of nanotube breakdown in vacuum and the thermal conductivity of nanotubes in the extreme high temperature limit. In addition, we combine this new technique with calibrated MWCNT heaters to address the size-dependence of the melting point of metallic nanocrystals.

5.4 The Thermal Test Platform

Figure 5.3 shows a schematic of the thermal test platform in different stages of construction and operation. Figure 5.3a shows an electrically conducting sample mounted on a custom-fabricated thin silicon nitride (Si_3N_4) membrane[69] that is transparent to high energy electrons, allowing real time observation in a transmission electron microscope. As shown in Figure 5.3b, a two-dimensional array of single-shot nanoscale thermometers is formed by subsequently depositing metallic nanoparticles onto the sample and membrane. As electrical current is driven through the sample, Joule heating causes the temperature of the sample (and supporting membrane) to increase. The temperature of different portions of the sample is determined locally by observing the onset of local melting and evaporation of the nanoparticle thermometers. Figure 5.3c shows the sample heated with a higher bias. As the temperature continues to increase, the single-shot thermometers show a "melting front" receding from the sample and forming a distinctive pattern on the membrane. This front corresponds to an isothermal line that, by employing finite element analysis to solve the heat distribution profile, can be used to extract the position-dependent temperature of the sample. As we demonstrate below, this nanoparticle thermometry method allows not only the local temperature of the sample to be determined (even when it greatly exceeds the melting point of the thermometers), but also its temperature-dependent thermal conductivity.

In the study of MWCNTs, we use a single nanotube as both the heater and the sample. For the study of other materials, a MWCNT or other nanoscale conductor could be applied as a heater for a nearby nanostructure of interest.

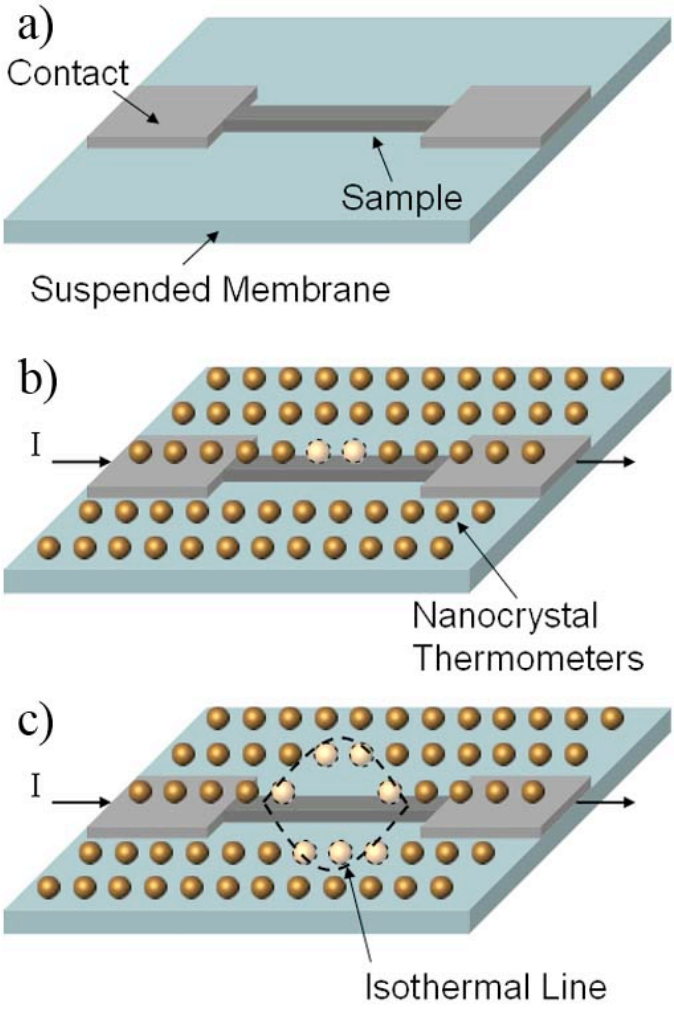

Figure 5.3: Design and Operation of the Thermal Test Platform
(a) A nanoscale sample is electrically contacted on a suspended membrane. (b) Nanocrystal thermometers are deposited on the sample. The sample is resistively heated via an electrical current, I, causing the nanocrystals to melt, yielding the temperature of the sample. (c) At higher bias, the melting nanocrystals yield an isothermal line which fans out across the membrane.

The fabrication of these devices is detailed in Appendix B. In brief, high quality arc discharge MWCNTs are ultrasonically dispersed in IPA and spin cast onto the membranes. These nanotubes are contacted using EBL and Pd contacts are evaporated via electron beam evaporation. The nanoparticle thermometers are applied by e-beam evaporating a thin (<10 Å) layer of gold. At this nominal thickness, the gold agglomerates into small nanoparticles instead of forming a continuous layer.

5.5 Heating an Individual MWCNT

Figure 5.4 shows a series of TEM images of a MWCNT mounted on the thermal test platform, together with nanoparticle thermometers. Small gold nanoparticles (typically <10 nm diameter) comprise a reliable and easy to read local temperature probe since they evaporate immediately upon melting (unlike indium, for example, which has a much lower vapor pressure at melting and electromigrates along nanotubes under similar conditions[48]). Since the melting temperature of gold nanoparticles is diameter dependent, we focus for the moment only on particles with diameter ∼6 nm, which have a well-established melting temperature of 1275 K[79]. The MWCNT sample is electrically contacted using palladium, which yields reliable low resistance electrical contacts (total sample resistances are typically ∼10 kΩ in the low bias regime).

Figure 5.4 shows the MWCNT device under zero electrical bias conditions. As the bias is increased, the Joule heating causes the temperature of the MWCNT and membrane to increase. Figure 5.4b demonstrates that the MWCNT becomes hottest in the center; the nanoparticle thermometers near the center of the tube are the first to melt and evaporate

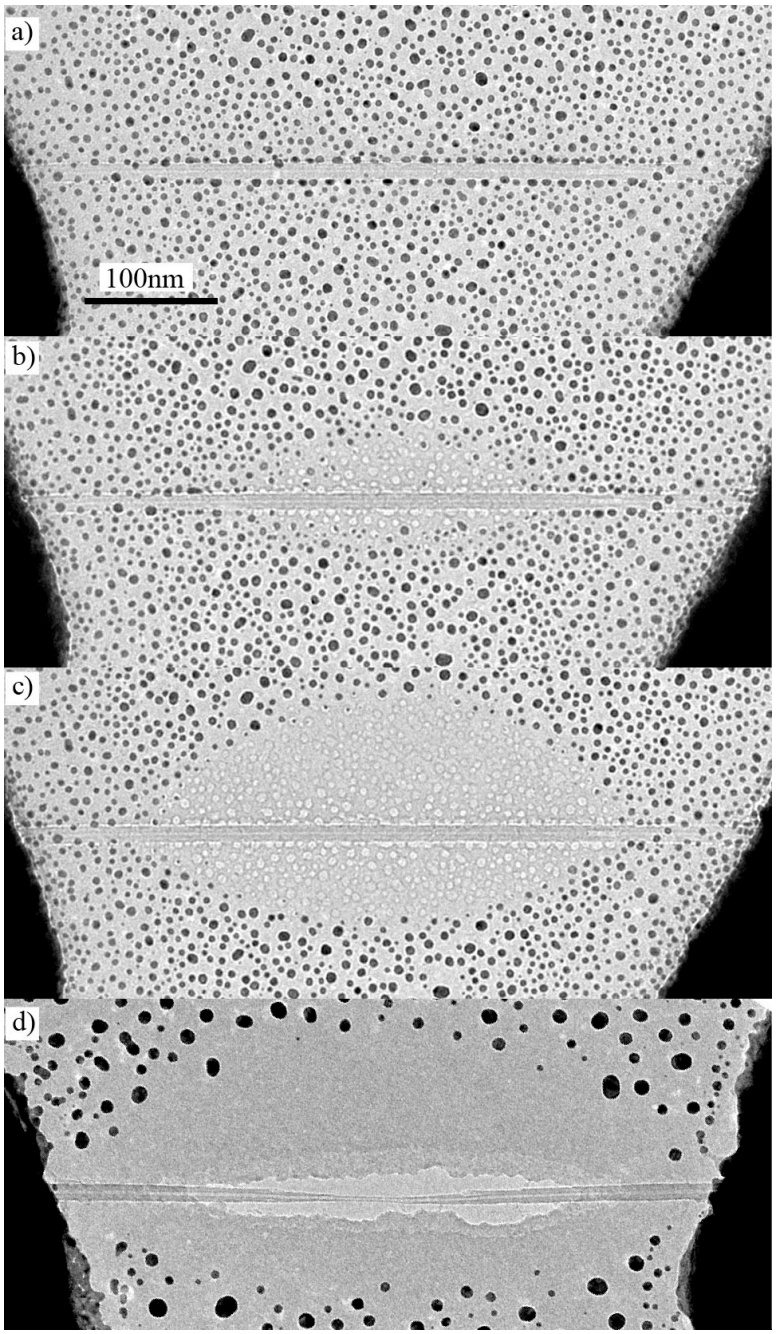

Figure 5.4: High Bias Operation of a MWCNT Device
(a-d) TEM images of MWCNT devices (a) Zero bias. (b, c) Same device operating at biases above the threshold for melting of the gold nanoparticles. (d) A different MWCNT (chosen for image clarity) beginning to break down. The light area near the center of the nanotube shows the membrane failure.

(the light colored spots on the central part of the membrane are signatures of the evaporated thermometers, not holes in the membrane). This is due to the diffusive nature of the electrical conductance in this high bias regime. As the bias is increased further, the thermometer melting/evaporation front continues to fan out from the center of the nanotube, both along the axis of the nanotube and on the surrounding membrane (Figure 5.4c). Eventually, at sufficiently high bias, the Si_3N_4 membrane directly underneath the MWCNT becomes so hot that it begins to disintegrate. This disintegration provides a second independent calibration point, at 2173 K, the breakdown temperature of Si_3N_4[80]. As the bias is still further increased, continued disintegration causes the membrane to peel back from the nanotube, decreasing the heat loss to the substrate and allowing the nanotube to heat even more effectively for a given electrical power input. The MWCNT is stable after suspension under increased bias, immediately indicating survival at temperatures well above that of Si_3N_4. At extreme temperatures the MWCNT eventually becomes fully suspended, and ultimately it catastrophically fails. Figure 5.4d shows (for a different MWCNT chosen for image clarity) the nanotube just prior to failure. The electrical current density prior to failure for the MWCNT of Figure 5.4d (with inner diameter 4.8 nm and outer diameter 14.7 nm) is $1.7 \times 10^8 A/cm^2$; other devices show comparable current-carrying capability at the stability threshold.

5.6 Modeling Nanoscale Temperature

The local nanotube temperature is determined by applying finite element analysis which requires a discussion of the thermal conductivity of MWCNTs. κ for nanotubes below

room temperature has been extensively probed, with measurements[81] and simulations[82] showing an increase in κ with increasing temperature. At high temperatures, increased phonon scattering should cause a decrease in the thermal conductivity with a peak expected near room temperature[78, 82, 83]. Despite great scientific and practical interest in the high temperature thermal conductivity of nanotubes, no reliable experiments have been performed in the extreme high temperature limit.

To determine κ of MWCNTs at high temperature, we use the thermal test platform configuration and employ finite element analysis to solve the heat equation at a given applied bias to determine the temperature distribution of the system. As a diffusive conductor in this regime, demonstrated by the shape of the isotherms peaking in the center of the device, the MWCNT obeys the classical heat equation with Joule heating. Treating the nanotube as a one-dimensional system with cross-sectional area A yields the heat equation:

$$A\nabla(\kappa\nabla T) + \frac{I \cdot V}{L} = 0 \tag{5.1}$$

where κ is the temperature dependent thermal conductivity, T the temperature, I the electrical bias current, V the voltage across the tube, and L the length of the tube.

We model the system in three dimensions using COMSOL Multiphsyics, a finite element solver. Figure 5.1 illustrates the model. We apply Equation 5.1 to create a finite element model of the entire system. The thermal and electrical properties of the Si_3N_4 substrate and Pd contacts are known and appropriate boundary conditions are employed. The electrical resistance of the nanotube is experimentally determined. The only free parameter of the system is the temperature dependent thermal conductivity, κ(T). For conditions up

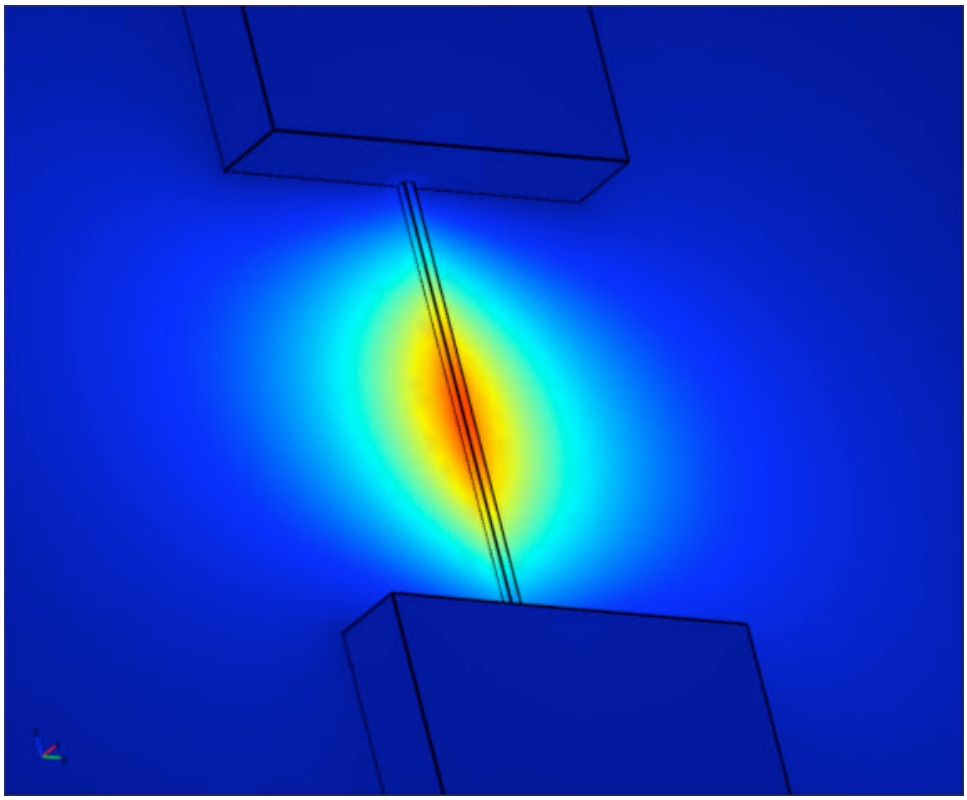

Figure 5.5: A 3D Model of the Joule Heated Nanotube System

to the failure of the Si_3N_4, we self-consistently solve the system for each dissipated power to reproduce the temperature profiles experimentally determined from the nanoparticle thermometers and the breakdown of Si_3N_4. We vary the functional form and value of κ(T) to produce a best fit for all dissipated powers of multiple device data. We find that the most appropriate functional form of κ(T) in the high temperature limit incorporates both Umklapp and second-order 3-phonon processes[84] and is expressed as

$$\kappa(T) = \frac{1}{\alpha T + \beta T^2} \tag{5.2}$$

with the linear term representing Umklapp (two-phonon) scattering and the quadratic term representing 3-phonon processes.

For each device, we determine the fit parameters α and β for the thermal conductivity. For the nanotube shown in Figure 5.4d, we find κ to be 150 W/m·K at 1275 K, with $\alpha = 4.8 \times 10^{-6}$ m/W and $\beta = 4.3 \times 10^{-10}$ m/W· K. Hence, the contribution of 3-phonon scattering modes becomes non-negligible at temperatures exceeding 1100 K.

Once κ(T) is known, the system is fully characterized, such that the local temperature can be determined for any given dissipated power. We now apply finite element analysis to determine the nanotube temperature beyond the local failure of the Si_3N_4 membrane. The model is adjusted to reflect the missing center of the membrane with heat still flowing through the remaining edges of the Si_3N_4. We solve the system with the determined κ(T) and the measured dissipated power immediately prior to nanotube failure, yielding the measured onset temperature for MWCNT sublimation, the highest temperature at the center of the nanotube, to be 3200 K. This temperature approaches theoretical predictions

for nanotube stability[75] and is 800 K higher than the onset temperature of sublimation of graphite[74]. Nanotubes are thus the most robust form of carbon. The exceptional mechanical stability is attributed to the strength of the sp^2 bond and the relatively defect-free geometry of MWCNTs.

Figure 5.6 shows the heating of the nanotube from Figure 5.4 with false color overlay of the temperature derived from finite element analysis. In Figure 5.6a, with no applied bias, the nanotube is at fully isothermal conditions with T=300 K (blue). Figure 5.6b shows the nanotube heating becomes hottest in the center as described previously. As the bias is increased further, the thermometer melting/evaporation front continues to fan out from the center of the nanotube, both along the axis of the nanotube and on the surrounding membrane (Figure 5.6c). Eventually, at sufficiently high bias, the Si_3N_4 membrane directly underneath the MWCNT becomes so hot that it begins to disintegrate. Figure 5.6d shows (for a different MWCNT chosen for image clarity) the thermal profile just prior to failure; the center portion of the nanotube is at T=3200 K.

5.7 Thermal Conductivity of MWCNT Over Full Temperature Range

Figure 5.7 shows the full temperature dependence of κ(T) from 10 K to nanotube failure at 3200 K. Low temperature data, up to 410 K, are taken from the literature[85, 86, 87]. The solid line shows the high temperature κ obtained from the experiment given by Equation 5.2 with parameters α and β obtained above. All values are normalized at 300 K. This curve is representative of all the nanotubes probed in this study. Importantly,

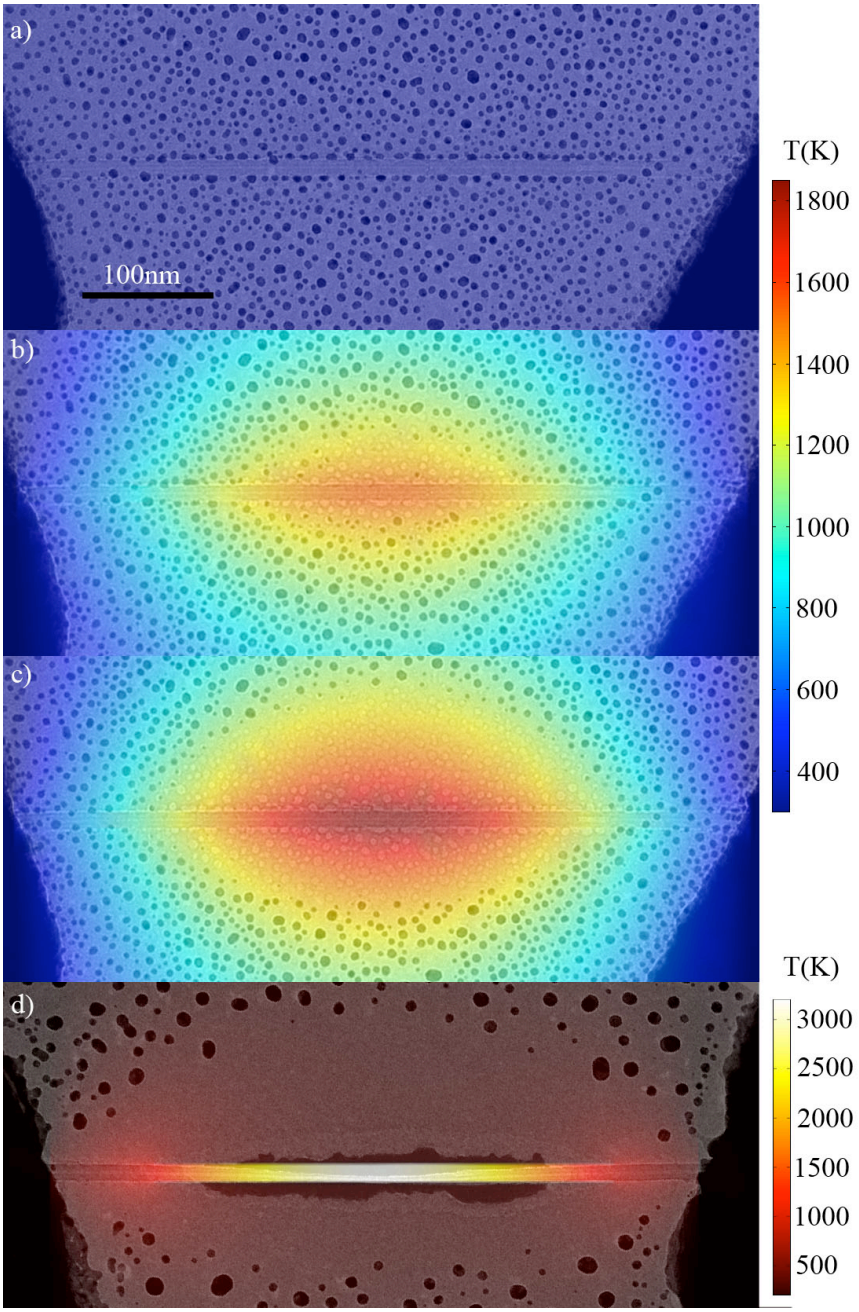

Figure 5.6: High Temperature Breakdown of a MWCNT Device
(a-d) TEM images of MWCNT devices with color overlays to indicate local temperature (note (d) uses a different color scale). (a) Zero bias, isothermal (T=300 K) conditions. (b, c) Same device operating at biases above the threshold for melting of the gold nanoparticles. (d) A different MWCNT (chosen for image clarity) operated close to the breakdown temperature of 3200 K. The darker area near the center of the nanotube shows the membrane failure.

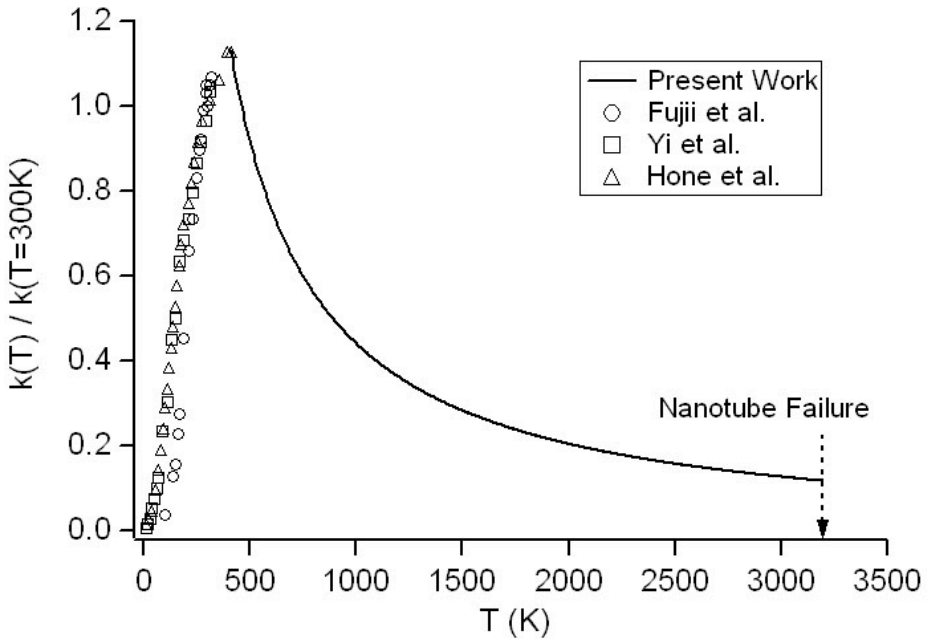

Figure 5.7: High Temperature Thermal Conductivity κ of MWCNTs
Experimentally determined high temperature κ reflecting Umklapp and 3-phonon processes (Equation 5.2) is plotted as a solid line. Also plotted are literature results for κ of various carbon nanotubes at low temperatures.[85, 86, 87]

at T=1000 K the MWCNT retains 50% of its peak thermal conductance, and at T=3000 K it still displays 10% retention. Even at temperature extremes, MWCNTs are impressive thermal conductors.

5.8 Melting Temperature of Gold Nanoparticles

By using MWCNTs as ultra-high temperature heating elements, our calibrated test platform can probe the high temperature properties of other nanoscale systems, including nanocrystals of various sizes. The melting point of our gold nanoparticle thermometers is well-established at particle size d=6 nm, but the melting point is known to be highly diameter dependent, a phenomenon first described by Pawlow in 1909[88]. Surprisingly,

the melting point of gold nanoparticles has not been experimentally mapped out in the ultra-small particle regime[79]. We here determine the melting point of gold particles down to 3 nm in diameter.

Figure 5.8a-e shows TEM observations of the melting point of gold nanoparticles, employing the now calibrated test platform with a MWCNT heater. Gold nanoparticles of various sizes reside directly atop the heater. We step the bias applied to the heater and determine the temperature at each steady state plateau. As anticipated, smaller gold nanoparticles melt at lower temperatures due to an enhanced surface-to-volume ratio. Figure 5.8f shows the resulting melting temperature, T_m, as a function of gold nanoparticle diameter d. The dashed line is a fit to the data of the liquid shell model[89] with a shell thickness of 0.5 nm. T_m of gold nanoparticles, and the applicability of the liquid shell model, are thus experimentally established to d=3 nm.

5.9 MWCNT Breakdown in Air

We also observed the breakdown of MWCNTs in air to compare the temperature and mechanism to breakdown in vacuum. This experiment could not be performed *in situ* in the TEM without the use of a secondary containment cell. Therefore the breakdown was performed while monitoring the current with TEM imaging performed subsequently. The experiments were performed on samples similar to those described above.

High bias was applied in air to Au nanoparticle thermometers decorated MWCNT devices. The bias was increased until electrical breakdown was initiated, as evident by rapid step decreases in the current. At this point, the bias was quickly turned off to stop the

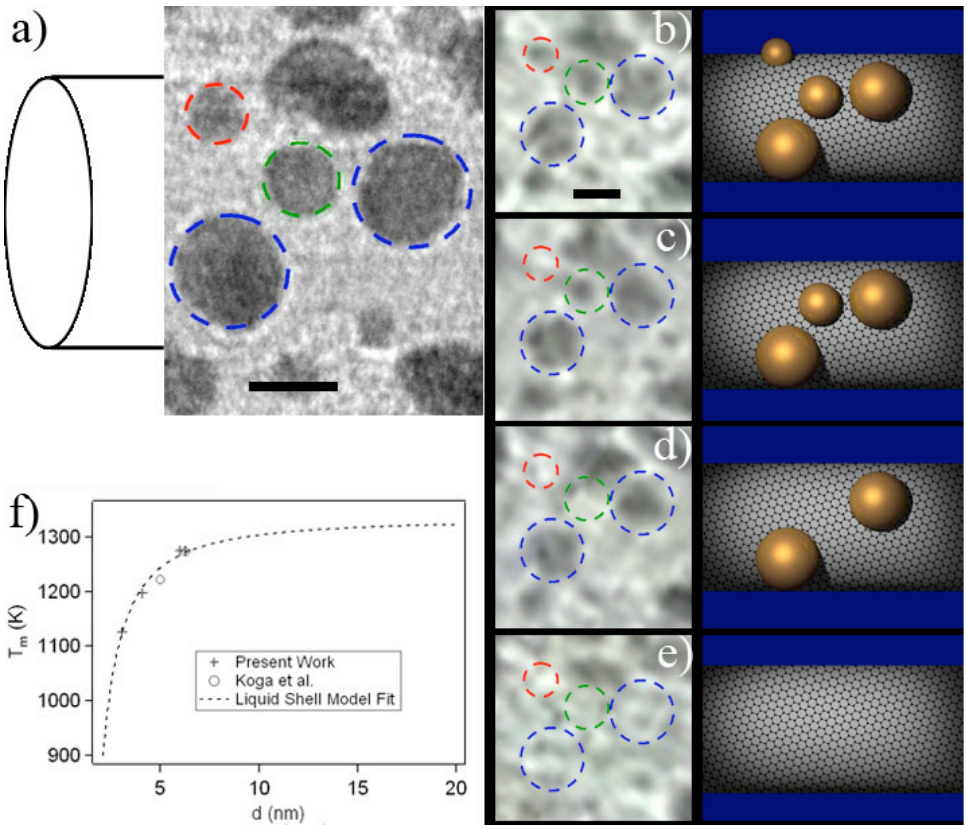

Figure 5.8: Diameter Dependence (d) of the Melting Point (T_m) of Gold Nanoparticles (NPs)
(a) TEM image of MWCNT heater with gold nanoparticles (lines indicate MWCNT outer wall). Selected NPs on the heater are outlined in color: red (d=3 nm), green (d=4 nm), and blue (d=6, 6.5 nm). (b-e) TEM video images as heater bias is increased with rendered models of system. (b) T=1065 K, no NPs have melted. (c) T=1130 K, 3 nm NP melts and evaporates. (d) T=1200 K, 4 nm NP evaporates. (e) T=1275 K, 6, 6.5 nm NPs evaporate. (f) T_m vs. d. Data from this study (+) show strong diameter dependence, with experimental results of Koga et al.[79] (○). The liquid shell model (dashed line) provides an excellent fit to the data.

breakdown process. We then loaded the membrane devices into the TEM to observe the nanoparticle thermometry array.

Figure 5.9 shows a nanotube that has been thinned by electrical breakdown in air. The heat generated by the nanotube causes the Au nanoparticles near the nanotube to agglomerate. This can be observed by comparing the larger size of the particles near the nanotube to those far away. This indicates that the breakdown in air occurs at a temperature below or near the melting temperature of gold, ∼1300 K. This implies that the nanotube walls burn in air under high electrical bias, which is a different mechanism than their sublimation in vacuum. We note, however, that the temperature profile of the device is similar, creating a hot spot in the middle. This leads to breakdown initiating in the center of the MWCNT, consistent with breakdown in vacuum.

5.10 Conclusion

Our thermal test platform has obvious application for the testing of high temperature properties of a broad range of other nanoscale particles and device structures. Of great practical importance is the unprecedented extreme thermal stability of MWCNTs, which surpasses the stability of other forms of carbon. The combination of high strength, high thermal (and electrical) conductivity, low weight, and exceptional thermal stability presents exciting opportunities for the use of MWCNTs under extreme conditions.

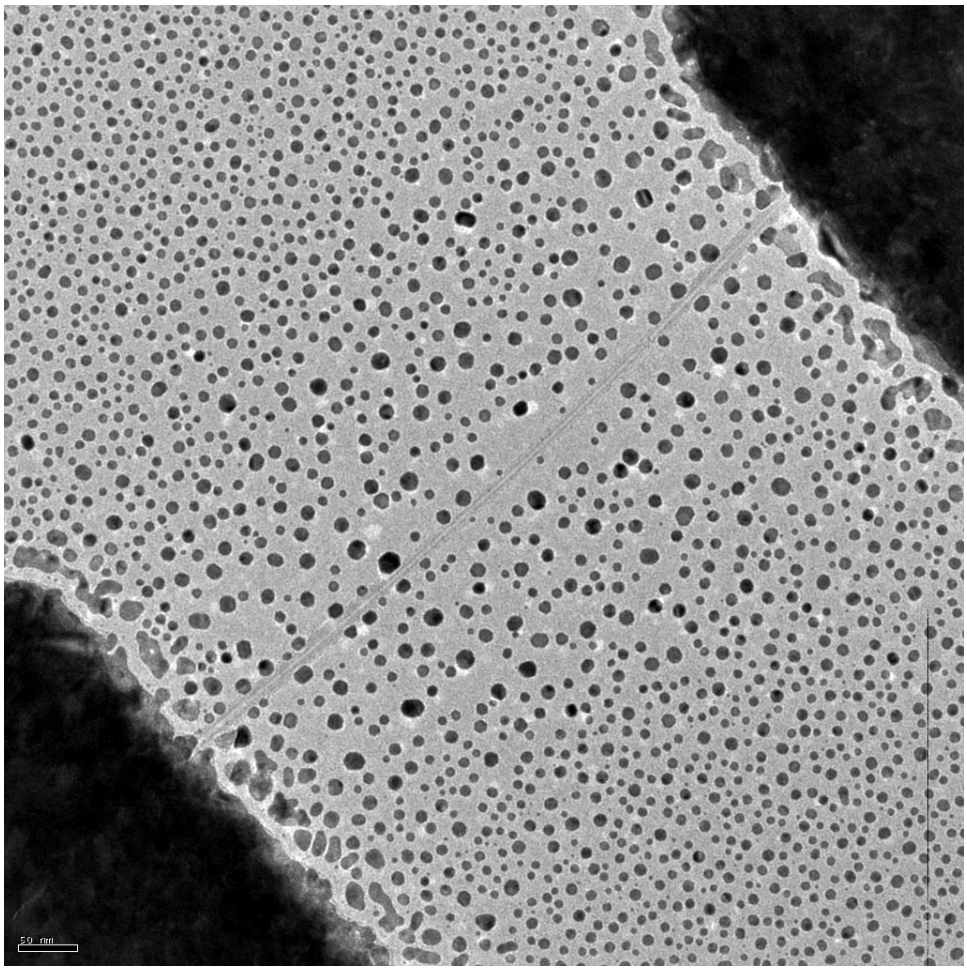

Figure 5.9: Breakdown of a MWCNT in Air.
This nanotube was driven at high bias in air. The thinning of the MWCNT in the center of the device indicates unambiguously that breakdown has occurred. The Au nanoparticle thermometers have begun to agglomerate near the center of the device, indicating that the nanotube heats from the center outward and begins failure near the melting temperature of the nanoparticles, ∼900 - 1000°C.

Chapter 6

In Situ Growth of Nanotubes: the Hidden Role of Facets

6.1 Forward

In this chapter we explore the role of crystal facets in the catalysis of carbon by iron for nanotube growth. We do this by observing the shape and state of an iron nanoparticle catalyst during *in situ* growth. We observe growth in a low carbon solubility metal and attribute the carbon diffusion to surface or subsurface diffusion. We perform *ab initio* calculations to explain our findings.

This work was performed with the help of Will Gannett. I thank Tom Yuzvinsky for help in interpreting the results and Elif Ertekin and Jeffrey Grossman for assistance with the theoretical calculations.

6.2 Abstract

The unique physical properties of carbon nanotubes suggest a broad range of applications in electronic, phononic, optical, and mechanical systems. Since small variations in nanotube geometry can strongly affect these properties, the successful realization of many nanotube-based technologies will require precise control over large-scale synthesis. However, the development of synthesis processes which yield nanotubes with pre-determined defect structure, diameter, and chirality has been hindered by the lack of understanding of the catalysis in transition-metal mediated growth. Fundamental questions remain regarding the physical state of the catalyst, the mode of carbon diffusion along or through the catalyst, and the means by which feedstock organic compounds are converted into atomic or molecular carbon during nanotube synthesis. Here we show the formation and dynamics of catalyst crystal facets during synthesis by observing fully-controlled solid state nanotube growth in real-time. Our observations reveal details of the synthesis process otherwise unattainable and yield insight into controllable nanotube synthesis.

6.3 Introduction

A powerful technique for the study of carbon nanotube (CNT) growth employs *in situ* environmental transmission electron microscopy (TEM)[90, 91, 92], where CNT growth occurs within a sealed, secondary compartment placed within the microscope. In the experiments here described, we employ a large-diameter multiwalled carbon nanotube[51, 93, 50] as a nanoscale reaction chamber. In addition to increasing resolution, this configuration al-

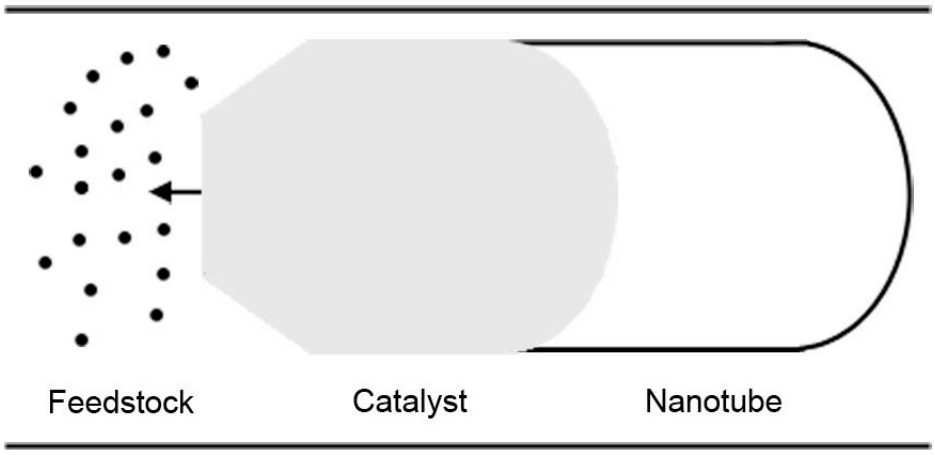

Figure 6.1: Solid State Growth of a CNT
A faceted catalyst particle removes carbon from a feedstock. The carbon surface diffuses to the opposite end of the catalyst and precipitates as a nanotube. The arrow shows the direction of motion of the catalyst relative to the feedstock.

lows precise control of the reaction temperature, the geometry of the catalyst particle, and the source rate of feedstock material during CNT growth. Figure 6.1 shows the synthesis configuration in simplified schematic form. Carbon feedstock, consisting of carbon organic molecules, amorphous carbon, or graphitic carbon is located within the growth chamber in close proximity to the catalytic iron nanoparticle. The reaction temperature is controlled by Joule heating via an applied electrical current through the walls of the chamber. The entire system is mounted on a specially fabricated electron-transparent silicon nitride membrane (see Methods), and imaged with a high resolution TEM (JEOL 2010, operated at 100 keV).

Iron nanocrystal encapsulated CNTs used for this experiment were synthesized via pyrolysis of ferrocene (see Appendix B). The CNTs are ultrasonically dispersed in isopropanol and spin cast onto prefabricated silicon nitride membrane structures. The samples are imaged in a scanning electron microscope and CNTs with appropriate iron filling are

selected. The samples are then patterned with electron beam lithography and Pd contacts are deposited via electron beam evaporation.

In practice, we find it advantageous to immobilize solid state carbon feedstock with respect to the reaction chamber and, using an electrical-current induced electromigration mechanism, move the catalytic particle with respect to the reaction chamber into the feedstock. In this way, encapsulated amorphous carbon, or even the innermost walls of the nanotube reaction chamber itself, can be consumed as source material for CNT growth. Catalyzed carbon diffuses along the catalyst in the direction of the current, consistent with electromigration of carbon in bulk iron[94]. As the carbon diffuses and the CNT grows from the trailing edge of the catalyst particle, the catalyst is displaced in the direction opposite the current, driving it into further carbon feedstock and continuing the growth. The direction of the applied current can be reversed at any time, thus reversing the direction of catalyst motion and CNT growth. Thus a newly grown nanotube can be deconstructed, atom-by-atom.

6.4 *In Situ* Growth of Carbon Nanotubes

Figure 6.2a shows a TEM image for a selected experiment. The horizontal striations running left to right across the upper and lower portions of the image represent concentric shells of the multiwall nanotube reaction chamber. The large dark object covering much of the right half of the image is the encapsulated iron catalyst particle. The smaller circular and oblong dark spots randomly distributed over the image represent gold nanoparticles intentionally deposited over the outside of the reaction chamber; these serve as absolute

position markers and also as local thermometers for high temperature measurements[95].

The state of the catalyst particle is of primary interest, both during hot CNT growth and in quiescent quench mode (with the drive current set to zero and the reaction chamber at room temperature). We employ nanobeam (∼100 nm beam size) electron diffraction in the TEM to characterize the catalyst. Figure 6.2c shows diffraction data, which are consistent with solid iron in the α phase (bcc crystal structure). The [100] axis of the iron crystal is aligned with the longitudinal axis of the reaction chamber. In addition, close examination of the catalyst in Fig. 2a shows that the left (leading) edge of the crystal is distinctly faceted. Figure 6.2b shows a tracing of the facet structure, with different crystallographic faces identified. As we discuss below, this facet structure is a key element in the functionality of the catalyst particle during CNT growth.

By precisely controlling the applied electrical drive current, we observe the atomic structure of the catalyst throughout different stages of CNT growth. From real time diffraction patterns and dark field imaging we find that the catalyst particle remains *solid and crystalline* throughout the CNT growth process. This is not to say, however, that the *shape* of the catalyst particle remains unchanged. Indeed, during CNT growth, the facet structure of both the leading and trailing edges of the catalyst evolves (via solid state transformation) in response to varying availability of feedstock material. The catalytically-active leading edge (the one receiving and disassembling sufficient carbon feedstock) is always found to be highly faceted, while the trailing edge (where the CNT is atomically assembled) has no observable facets. When we reverse the growth direction, the leading and trailing edges of the catalytic particle interchange, and the facet structure switches concomitantly from one

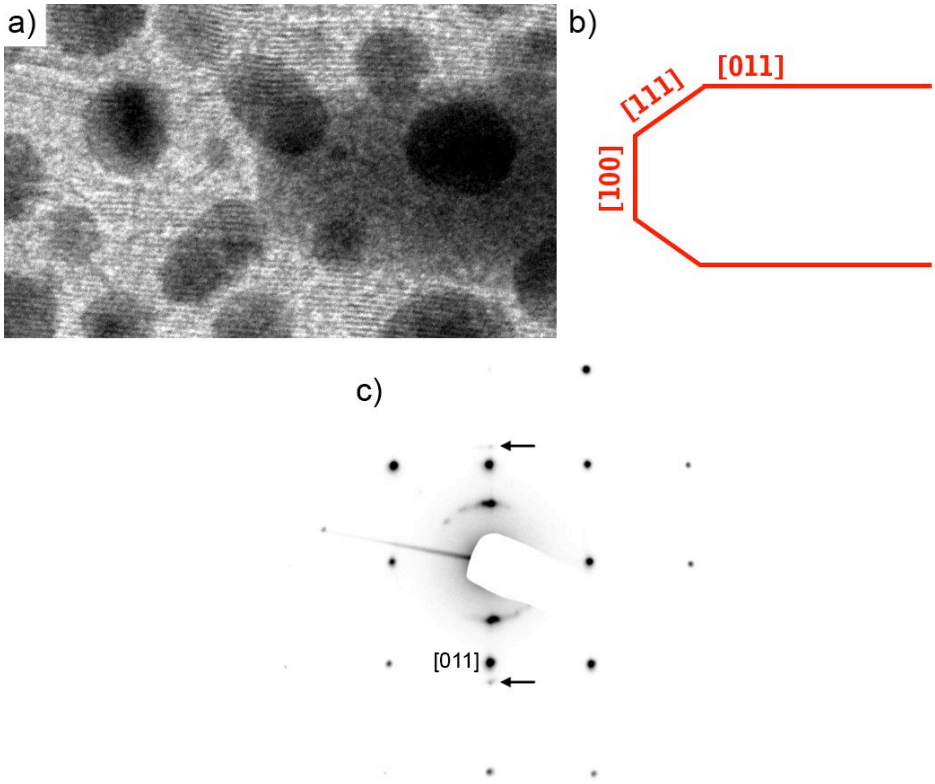

Figure 6.2: Orientation of the Catalyst Facets
(a) A typical leading edge of the iron catalyst in contact with the inner nanotube walls during the synthesis showing the flat front and angled facets. The dark round objects are gold markers deposited externally position markers. The angle between the front and angled facets is 55°, close to the expected 54.75° between (100) and (111) planes of α-iron. (b) A drawing indicating the labeling of the facets in a. (c) Nanobeam diffraction of a typical encapsulated iron particle indicating bcc crystal structure. The nanotube wall spacing is indicated by the arrows and is parallel to the labeled [011] iron diffraction peak.

end of the catalyst to the other.

Figure 6.3 shows details of the facet geometry of the catalyst's leading edge during different stages of the CNT growth process (complementary details of CNT growth at the catalyst's trailing edge are shown in Figure 6.4). In Figure 6.3a, during initial stages of movement, large (111) facets and strong catalytic activity result in CNT growth (this occurs to the right and is not shown in these images). The (111) facets are present in response to the the abundance of carbon feedstock, in the form of graphitic layers. As feedstock becomes less abundant, the (111) facets adjust accordingly, successively shrinking in size (Figure 6.3b-d). When all carbon feedstock is exhausted (Figure 6.3e), the (111) facets disappear altogether, and CNT growth ceases.

Figure 6.5 schematically summarizes our observations of facet evolution and nanotube growth. Figure 6.5a shows the unfaceted iron catalyst in the as-prepared system. Application of current causes (111) facets to form at the leading (left) edge of the iron (anode), where catalysis of the carbon feedstock occurs (Figure 6.5b). Catalyzed carbon diffuses along the catalyst in the direction of the current and coats the opposite trailing end of the catalyst (the cathode). The iron catalyst is displaced in the direction opposite the current, driving it into further carbon feedstock and further loading it with carbon. Excess carbon is released via growth of a carbon nanotube at the trailing (right) edge of the catalyst (Figure 6.5c). While the carbon quantity is conserved, the newly synthesized nanotube may be of a different geometry than the carbon feedstock and thus may be both longer and of fewer walls, as portrayed here. Reversal of the applied current (Figure 6.5d) causes facets to form on the opposite end of the catalyst (the new anode) as the iron consumes the newly

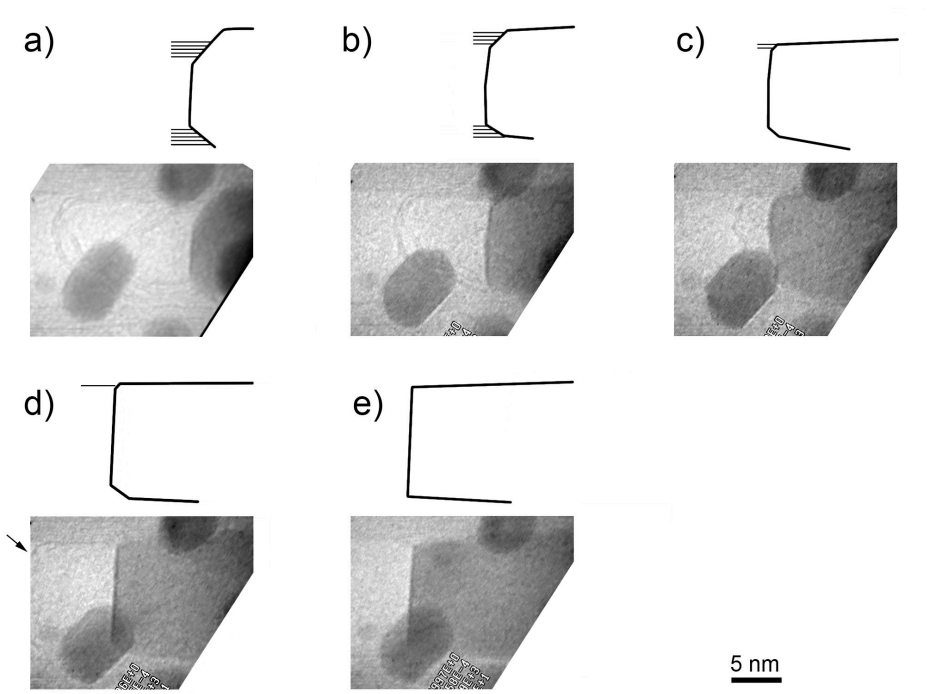

Figure 6.3: Tracking Facet Structure
Frames from video of the leading edge of the catalyst accompanied by outlines of the catalyst and incoming carbon source in the form of graphitic layers. Note that some layers are obscured by gold markers. Current is applied from left to right in the images. (a) The catalyst begins moving forward (left) with many feedstock layers interacting with the angled (111) facets. (b-d) The innermost layers of the source become absorbed as the catalysts progresses and the (111) facets decrease in size. (d) An arrow points to the last source layer. (e) The source is completely exhausted and the (111) facets disappear. Nanotube growth is no longer possible.

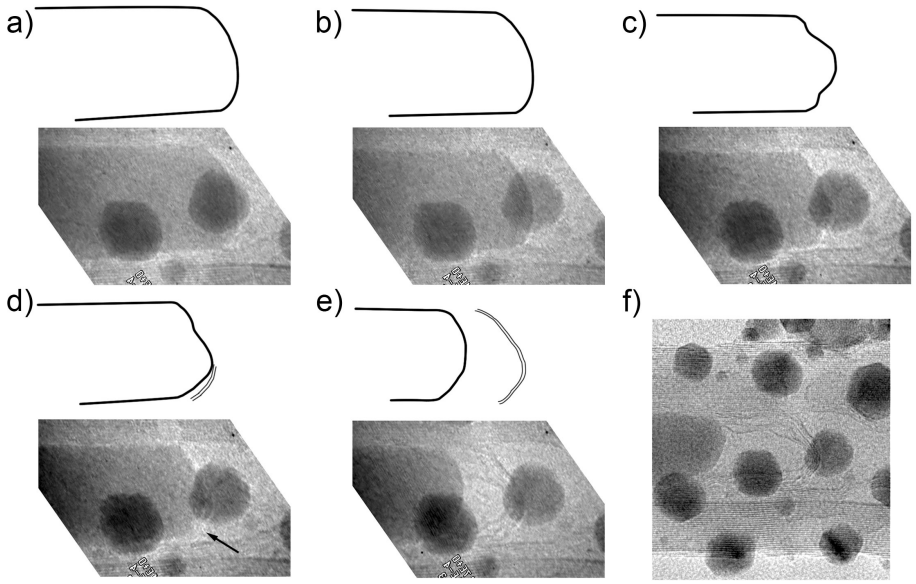

Figure 6.4: In Situ Nanotube Growth
(a-e) Frames from video of the in situ nanotube growth at the trailing edge of the catalyst accompanied by outlines of the catalyst and parts of the extruded nanotube. Note that some layers are obscured by gold markers. Current is applied from left to right in the images. (a) The iron nanoparticle catalyst prior to application of current. (b) The catalyst begins to move right. (c) Carbon begins to cover the trailing edge (right, cathode), causing the shape to change. (d), CNT walls begin to lift off of the catalyst. The Arrow indicated the first walls to lift off. (e) A MWCNT is grown off of the catalyst. The observations of this growth process are consistent with theoretical predictions of carbon surface saturation and endcap formation on the surface of a catalyst[96]. (f) A high resolution image of the nanotube after growth.

formed nanotube and precipitates a multiwall nanotube at the left end (new cathode).

6.5 Understanding the Role of Facets

Due to their extremely high surface-to-volume ratios, catalyst nanoparticles are highly susceptible to environmental changes which affect the relative stabilities of their different surfaces. During synthesis, we observe in the leading edge of the catalyst that the iron (111) facets grow (or shrink) to accommodate larger (or smaller) numbers of internal nanotube wall feedstock. In order to understand this change, we have performed *ab initio* calculations based on density functional theory (DFT) of the relative energies of different α-iron surfaces. Binding energies of single carbon atoms to the surfaces as well as the surface energies of fully carbon-saturated iron surfaces are shown in Table 6.1 (binding sites shown in Figure 6.6). Our calculations are in good agreement with previous theoretical work[97].

Surface	**Geometry**	**Site**	**Binding Energy (eV)**	**Compare to Hong[97]**
bcc 100	[3x3x3]	A	8.46	–
bcc 100	[3x3x3]	B	10.58	–
bcc 100	[1x1x3]	B (saturated)	8.09	8.17
bcc 111	[3x3x3]	A	8.84	–
bcc 111	[3x3x3]	B	2.83	–
bcc 111	[3x3x3]	C	8.65	–
bcc 111	[3x3x3]	D	8.84	–
bcc 111	[1x1x3]	D (saturated)	7.53	7.67
bcc 110	[2x3x3]	A	9.21	–
bcc 110	[2x3x3]	B	8.20	–
bcc 110	[1x1x3]	B (saturated)	7.80	7.89

Table 6.1: Carbon Binding Energies on α-Fe Surfaces Sites are illustrated in Figure 6.6.

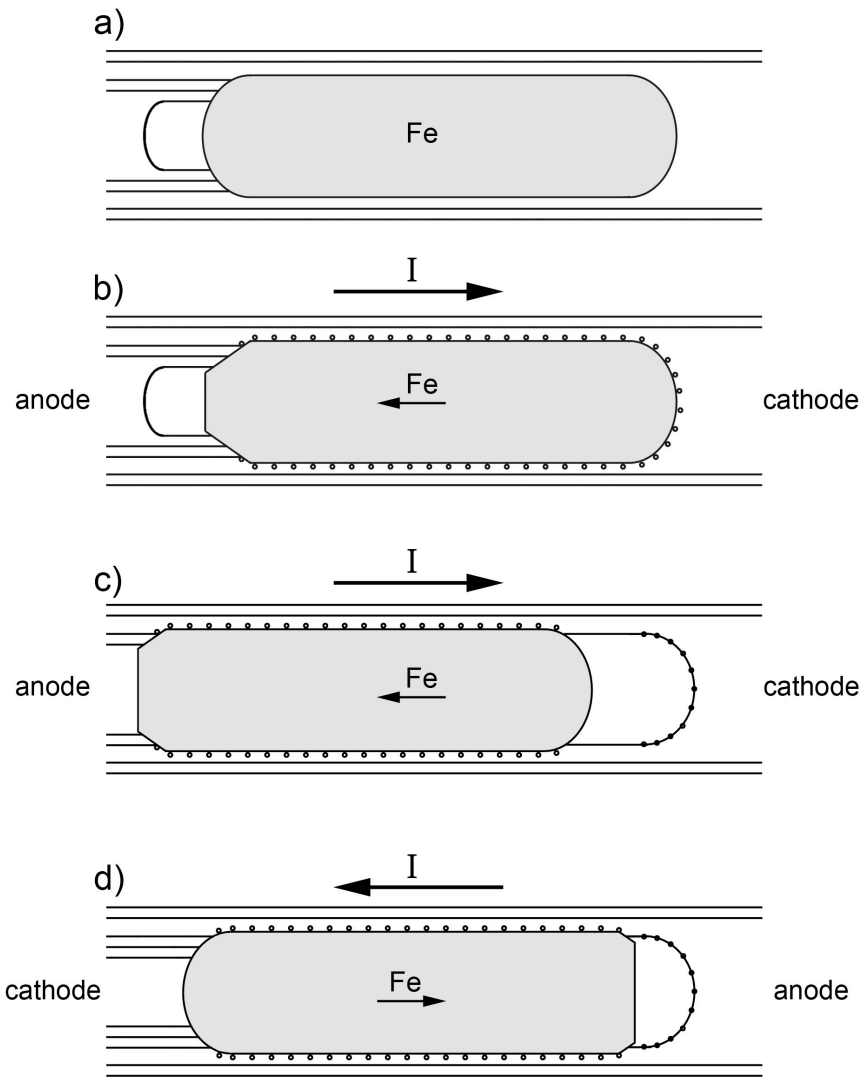

Figure 6.5: Schematic of *In Situ* Nanotube Synthesis
A metal encapsulated MWCNT with the outer nanotube walls as the synthesis chamber, the encapsulated metal (gray) as the catalyst, and the internal walls of the MWCNT or amorphous carbon as the source. (a) The system as synthesized. (b) As current is applied, carbon electromigrates along the surface in the direction of the current and facets form at the anode. The carbon supersaturates at the cathode. (c) Carbon moving in the direction of the current along the catalyst pushes the catalyst against the current, driving further catalysis of the carbon source and growth of a nanotube. Changes in the carbon feedstock causes the facets to evolve. (d) By reversing the applied current, the reaction is reversed. Facets form at the new anode and the newly grown nanotube is consumed.

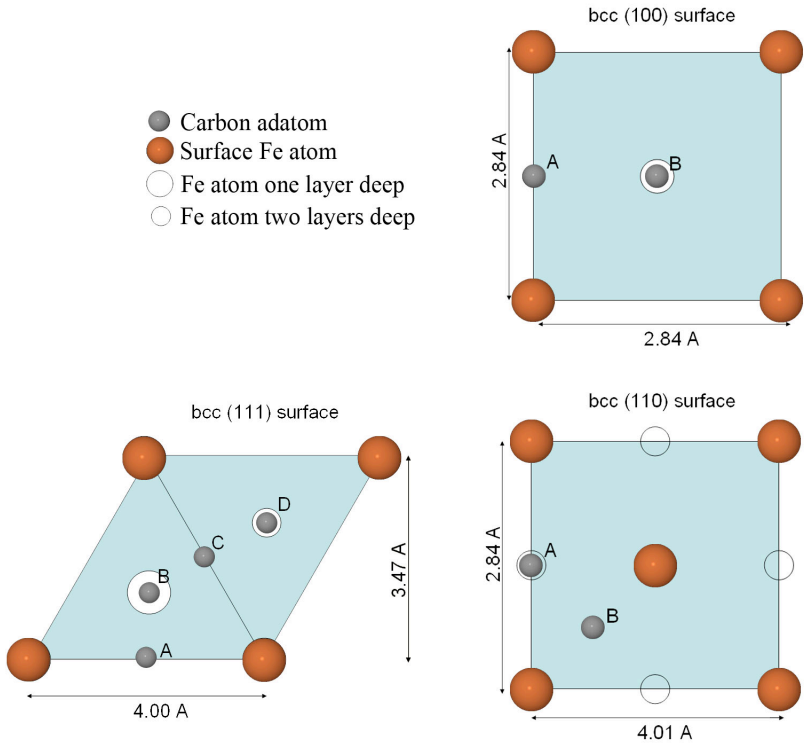

Figure 6.6: Binding Sites of Carbon on α-Iron for *ab initio* Calculations
Carbon adatoms are shown on (100), (110), and (111) α-iron surfaces. Sites are chosen at high symmetry points. Binding energies of Carbon atoms are given in Table 6.1. Illustrations not to scale.

In general, the equilibrium shape of the iron catalyst can be predicted by the Wulff construction using the calculated surface energies. However, accurate modeling of the shape of the catalyst requires consideration of the nature of the surface termination by carbon atoms, penetrating nanotube walls, etc. In our synthesis, the iron is contained by graphitic layers in the radial direction and is catalyzing carbon from penetrating graphitic sheets, not isolated carbon atoms on the catalyst's leading edge. To model our system accurately, we perform DFT calculations of iron surfaces interacting with graphene sheets impingent upon the surface as well as surfaces that are saturated with carbon atoms. To

Surface	Description	Energy (eV/Å^2)	Compare to Hong[97]
bcc 100	free	0.157	0.149
bcc 100	saturated with C	0.303	–
bcc 100	perpendicular graphene	0.218	–
bcc 111	free	0.166	0.160
bcc 111	saturated with C	0.292	–
bcc 111	perpendicular graphene	0.222	–
bcc 110	free	0.154	0.147
bcc 110	saturated with C	0.284	–
bcc 110	perpendicular graphene	0.237	–
bcc 110	parallel graphene	0.190	–

Table 6.2: Summary of Carbon-Iron Surface Energies
The surface energies of α-Fe surfaces with different surface carbon geometries: free (no carbon), saturated with carbon, impingent perpendicular graphene sheets, and a parallel graphene sheet.

simulate the containment by the MWCNT chamber, we calculate the surface energy of the iron (110) interacting with a parallel layer of graphene. The results are shown in Table 6.2. Using these calculations we are able to explain our observations of the evolution of the facet structure during nanotube growth.

Figure 6.7 shows the Wulff construction of the iron catalyst obtained using surface energies computed from the DFT calculations for two different conditions. In Figure 6.7a, we model the nanoparticle after the feedstock has been exhausted; the iron (111) and (100) facets are both saturated with carbon atoms, resulting in a Wulff structure with small (111) facets. In contrast, in Fig. 5b, to model the system during catalysis, we apply the surface energy of the iron (111) surface terminated by perpendicular graphene sheets (but keep the (100) facet saturated with carbon atoms). Because the (111) surface has lower energy when graphene-terminated than when carbon-saturated, the Wulff construction shows enhanced (111) facets when graphene-terminated, corresponding well to the behavior we observe in

the experiments. Although these calculations consider only several representative cases for carbon/Fe-surface termination structures, they nonetheless indicate that relative changes in surface energies for different surface terminations can explain the catalyst shape changes observed.

We note that the feedstock graphitic walls are never observed to intersect the (100) surface, even though its graphene-terminated surface energy is lower than that of the graphene-terminated (111) surface. In order to understand this, we first note that the nanotube walls are constrained to the outer edge of the chamber. We then compare the relative energies of two distinct particle shapes: (1) a flat faced catalyst with no (111) facets, with a portion of the (100) surface graphene-terminated and the remainder carbon saturated, and (2) a catalyst with (100) and (111) facets, with only the (111) surface graphene terminated. Comparing the relative energies of these systems at overall equal portions of graphene-termination, we find the total energy of the latter system (the structure that we observe in our experiments) to be lower for graphene-termination coverage below a critical threshold. Below the threshold, the equilibrium structure is predominately determined by a minimization of total surface area and (111) facets are stable; however, beyond the threshold, the lower surface energy of the (100) facet dominates, causing the (111) facets to disappear. Consistent with this prediction, our experiments take place in the former regime.

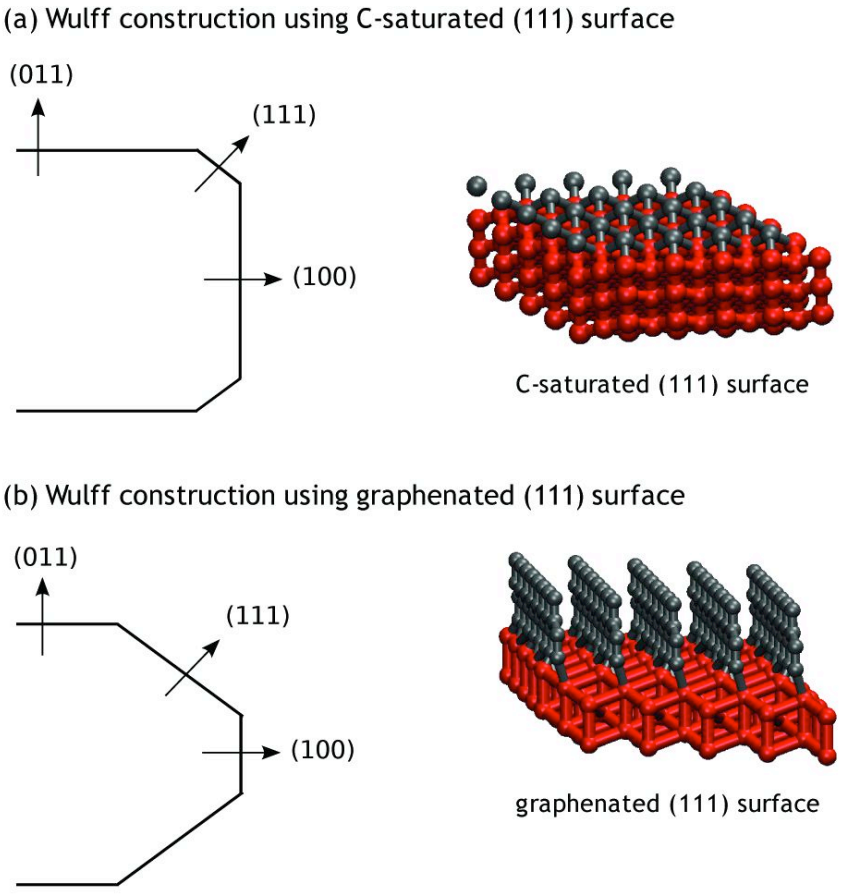

Figure 6.7: Catalyst Equilibrium Facet Structures
Wolff constructions are shown for the α-iron catalyst with different surface terminations. For both structures, the (011) surface is terminated with an overlying parallel layer of graphene. (a) Wulff construction obtained using carbon saturated (100) and (111) surface energies. (b) Wulff construction obtained using carbon saturated (100) and graphene-terminated (111) surface energies. The different facet structures correspond well with the changes observed in experiment as impingent graphene layers are consumed.

6.6 Diffusion of Carbon

Once the iron has catalyzed the dissociation of the carbon source, newly deposited carbon atoms on the leading catalyst surface must diffuse along the (110) plane to the trailing edge of the nanoparticle for CNT synthesis to proceed. We now consider two different models of the migration of carbon in the iron catalyst: bulk diffusion and surface diffusion.

For bulk diffusion to occur, carbon must dissolve into the iron catalyst. However, α-iron has very low carbon solubility, with a maximum at 0.028 weight percent, two orders of magnitude lower than that of γ (fcc) iron. As carbon solubility has been expected to predict catalyst suitability[98], confirmation of growth in bcc iron is surprising and perhaps unprecedented. Additionally, theoretical studies have found that the energy required for a carbon atom to penetrate into the center of a nanoparticle is prohibitively high[99]. The iron-carbon phase diagram shows that the solubility of carbon in bcc iron increases as the temperature rises in the relevant temperature range. Were bulk diffusion to dominate the carbon migration, the iron would be nearly saturated during synthesis. Rapid cooling of the system, and the resulting decrease in carbon solubility, would cause either precipitation of carbon out of the iron or the formation of a carbide phase. We quench the hot nanoparticle by zeroing the current, but we do not observe either of these phenomena. Since high resolution TEM and diffraction are more than sufficient to see these effects, we conclude that surface or subsurface diffusion of carbon on the iron dominates over bulk diffusion.

Chapter 7

A Nanoelectromechanical Memory Device

7.1 Forward

In this chapter we explore the properties and application of electromigration of metal encapsulated within a nanotube. A nanoparticle shuttle moves along the nanotube track and can be controlled with the application of current, much like a nanoscale model train. We exact precision control of a small payload and read out the position through the resistance of the device. This immediately lends itself to application as a memory element.

This work was performed with the help of Will Gannett. I thank Tom Yuzvinsky for help in interpreting the results and Vin Crespi for help with calculations.

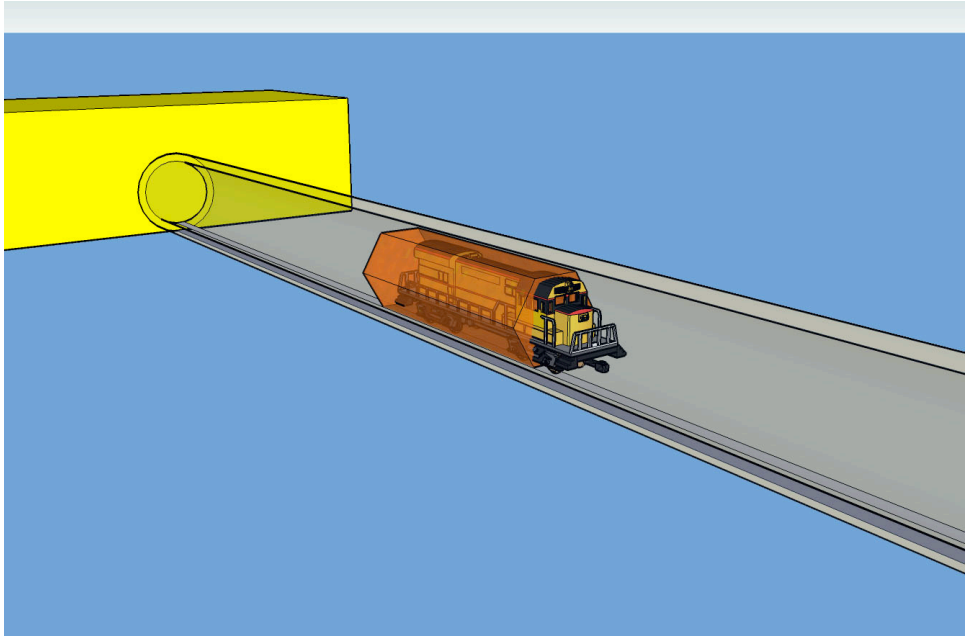

Figure 7.1: Author's Rendition of a Nanotrain Memory Device

7.2 Abstract

We report on a simple electromechanical nanotube based memory device in which an iron nanoparticle payload is controllably positioned along a nanotube track. The nanoparticle can be moved reversibly due to electromigration forces, and can be positioned with nanoscale precision. The movement of the shuttle can be read out with the use of only two contacts, allowing application as a nonvolatile memory element with potentially hundreds of memory states per device. The simple fabrication of these devices is suitable for large scale integration, with memory density $\sim$1 Tbit/in^2. We calculate the thermodynamic stability of these memory devices to be in excess of a billion years, indicating that they may be suitable for archival storage.

7.3 Introduction

The miniaturization of nonvolatile silicon-based memory devices has revolutionized the creation, access, and exchange of digital information. There exists great interest in continuing this miniaturization, with carbon nanotubes presenting an attractive alternative to silicon due to their intrinsic scale and excellent electrical and thermal properties. While substantial progress has been made in developing electromechanical nanotube memory devices[100, 25, 101], including a proposal (yet to be realized) for an encapsulated fullerene shuttling within a nanotube core[102], current implementations require multiple complicated fabrication steps that can drastically lower the ultimate yield of functional memory elements.

Here we demonstrate the realization of a nonvolatile nanotube-based memory element that utilizes mass transport of a metallic inner shuttle. When integrated in a planar geometry, our device is both easy to fabricate and compatible with standard silicon processing. The fabrication involves only one lithography step to form contacts and requires no post-processing of the device. Notably, the memory operates at low voltage and requires only two terminals, allowing high density large scale integration. The system differs from previous electromechanical nanotube memories in that it has no externally moving parts, decreasing environmental susceptibility.

Transition metals (including Fe[50], Co[51], In[48], Cu[52], and W[46]) can be transported along an electrically contacted carbon nanotube by applying a sufficiently large current to the nanotube. This mass transport has many potential applications for customizing nanotube devices and has already been used for zone refinement of nanotubes[51]

and nanoscale spot welding[52, 46, 50]. A limiting factor of the studies to date has been their dependence upon piezocontrolled nanomanipulators to make electrical contact to the nanotube. In order for nanotube mass transport to be broadly utilized in devices, a planar geometry compatible with large-scale integration must be used.

7.4 Design

Figure 7.2a shows a schematic of our mass transport memory device, whose primary element is an iron nanoparticle encapsulated within a multiwall carbon nanotube. These heterogeneous nanostructures are synthesized in a single step via pyrolysis of ferrocene in argon at 1000°C. They are then ultrasonically dispersed in isopropanol and deposited on a substrate. For diagnostic purposes, we use as a substrate a custom fabricated silicon nitride membrane compatible with transmission electron microscopy. The devices are created in one lithographic step; electrical contacts are patterned on the nanotube and 100 nm palladium is deposited and lifted off in acetone. The thin membrane is mounted inside a biasing stage that allows the planar device to be imaged with a high resolution TEM in real time while the system is probed electrically.

The iron nanoparticle acts as an internal shuttle that can move along the channel defined by the nanotube housing. The shuttle is moved controllably along this one-dimensional track by the application of an electrical current to the nanotube, similar to a model train that receives its drive from an electrical rail: when the current is reversed, the shuttle moves in the opposite direction. The direction of motion of the shuttle is opposite the applied current and is caused by electromigration, consistent with previous studies[50].

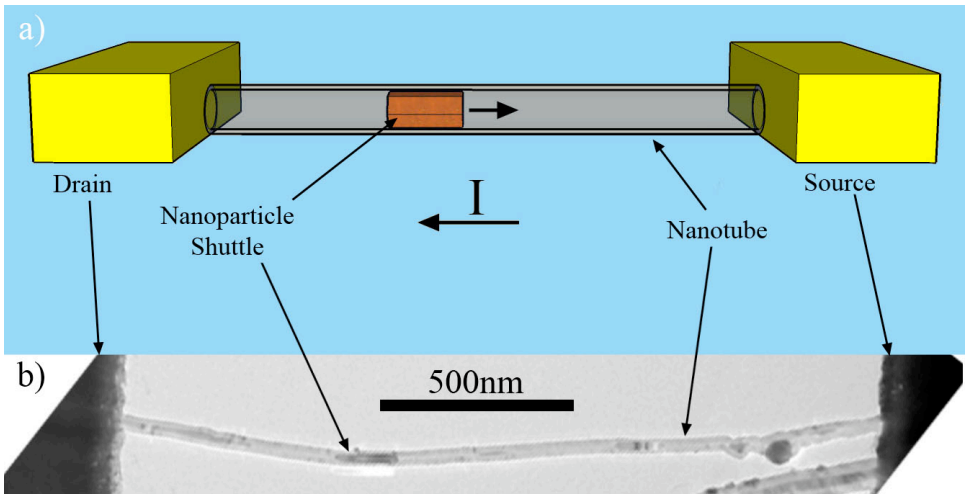

Figure 7.2: Mass Transport Memory Device Schematic
(a) An artistic representation of the memory device shows a nanoparticle encapsulated within a MWCNT. The nanotube is electrically contacted on the left and right. Application of current from right to left causes the nanoparticle shuttle to move from left to right due to electromigration. (b) a low resolution TEM image of a real device utilizing an iron filled nanotube as the memory element. The dark areas to the left and right are the palladium electrical contacts and the dark area near the center left is the iron nanoparticle shuttle. The light copy of the nanoparticle directly above it is a reflection indicating the crystalline state of the iron.

Figure 7.2b shows a low magnification TEM image of a real device. An iron nanoparticle is encapsulated within a MWCNT that is electrically contacted with palladium. The bright reflection of the nanoparticle indicates that the iron is crystalline. By observing the system in the TEM, the position and state of the iron shuttle can be measured concurrently with the electrical transport properties of the device.

7.5 Attogram Payload Delivery

7.5.1 Reversible Motion

Figure 7.3 shows the movement of the shuttle under applied bias. The nanotube shown is the same as that in Figure 7.2b, with the electrical contacts out of view to the left and right. Bias is applied and increased until an onset current on the order of a few hundred microamperes is reached, causing the nanoparticle to begin moving. In Figures 7.3a-c, the current is applied from left to right, causing the nanoparticle to shuttle to the left, against the applied current, for a distance of a few hundred nanometers. In Figures 7.3d,e, the bias is reversed, causing the nanoparticle to change direction and return to its original position. The shuttle can be moved across the entire length of the nanotube in a reversible and reproducible fashion. This process can be repeated over multiple iterations.

The speed of the shuttle can be tuned over several orders of magnitude by exploiting its strong dependence upon the applied bias. Figure 7.4 shows the shuttle speed as a function of bias for the device shown in Figure 7.3. At the onset of motion, occurring at a bias of 1.55 V, the shuttle moves at a rate of $\sim$1 nm/s, on the order of the speed of slow continental drift[103]. At 1.75 V, the highest bias applied to this device, the iron moves at

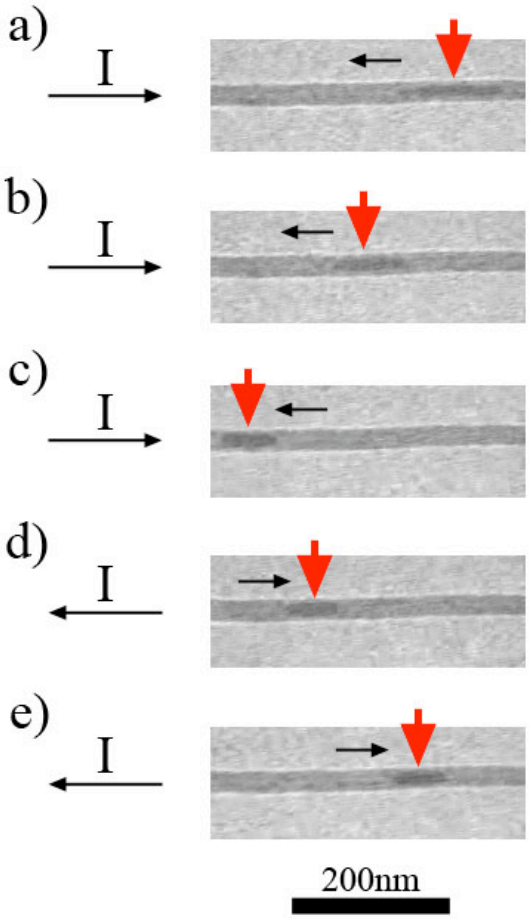

Figure 7.3: Long Range Reversible Mass Transport
TEM images showing the long range movement of the iron nanoparticle shuttle over a distance of ∼500 nm. The position of the iron nanoparticle is denoted in each frame by a red arrow. The nanoparticle always moves in the opposite direction of the applied current. (a-c) The current is applied to the right, and the nanoparticle moves to the left. (d and e) The current is reversed and the particle moves to the right.

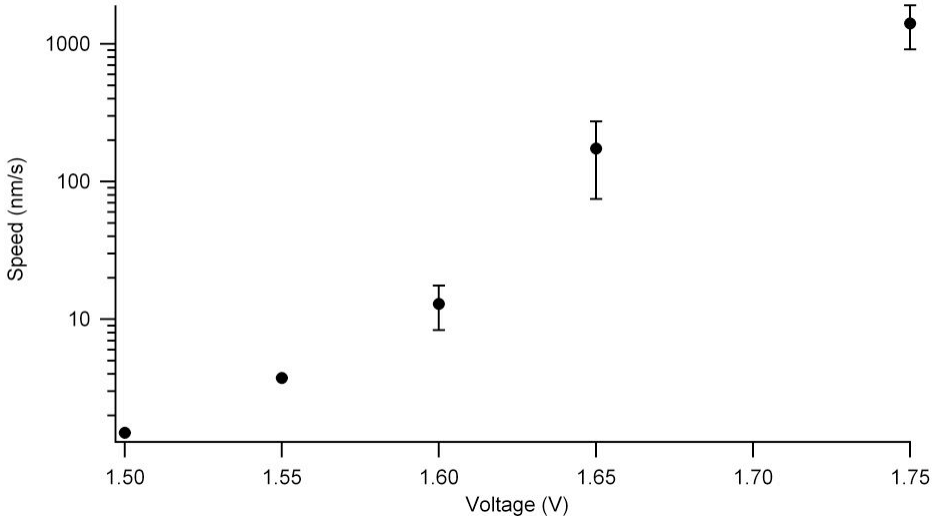

Figure 7.4: Shuttle Speed as a Function of Applied Bias
Adjusting the applied bias strongly affects the speed of the nanoparticle shuttle through the nanotube. The speed is shown plotted versus the bias for the nanotube shown in Figure 7.3. The highest speed measured (not shown) is limited by the speed of our video camera and is greater than 25 μm/s.

1.4 μm/s. As nanoscale motors are often compared to their biological counterparts, we note that this speed is close to that of the motor protein myosin[104]. With other devices we have observed that the shuttle velocity can be increased by at least four orders of magnitude, exceeding 25 μm/s, the maximum speed we can detect due to the frame rate of our TEM video camera. The true top speed could be considerably higher and may be limited only by the total current carrying capacity of the supporting nanotube.

We attribute the reversibility of our system to low device resistance (typically under 10 kΩ) enabled by our high quality electrical contacts. Among transition metal transport measurements, this low contact resistance is a feature unique to our experimental setup, as we employ intimately connected, evaporated metal contacts instead of nanomanipulation probes used in previous experiments. The low contact resistance causes a symmetric

temperature profile of the system[95], whereas large contact resistance could cause a highly one-sided thermal profile that could limit the total range of motion of the shuttle, with irreversible high thermal gradients overcoming the reversible electromigration force[105].

7.5.2 Nanometer Scale Precision

In addition to reversing the direction of transport, we are able to precisely position the nanoparticle shuttle along the nanotube. We apply a short (∼20 ns) voltage pulse on the order of 2V to the system and cause the shuttle to translate 3 nm. Successive pulses induce translation of the shuttle analogous to, but an order of magnitude more precise than, the walking motion of myosin VI, which moves in 36 nm steps along an actin filament[106]. The combination of these techniques, static biasing and pulsing, allows precision control of the shuttle position on a micro- and nanoscale.

7.6 Memory Device

7.6.1 Position Based Sensing

We can apply the precision delivery of a nanoscale payload to application as a memory device. In its simplest form, one could determine the memory state of such a device by simply observing the location of the shuttle. We accomplish this through bright field TEM. If the shuttle is below a threshold position, the state is '0'. Likewise, if the shuttle is above the threshold, the state is '1'.

Figure 7.5 shows the application of the shuttle as a position-based memory device. The system begins in a '1' bit with the shuttle toward the bottom of the device. A '0' write

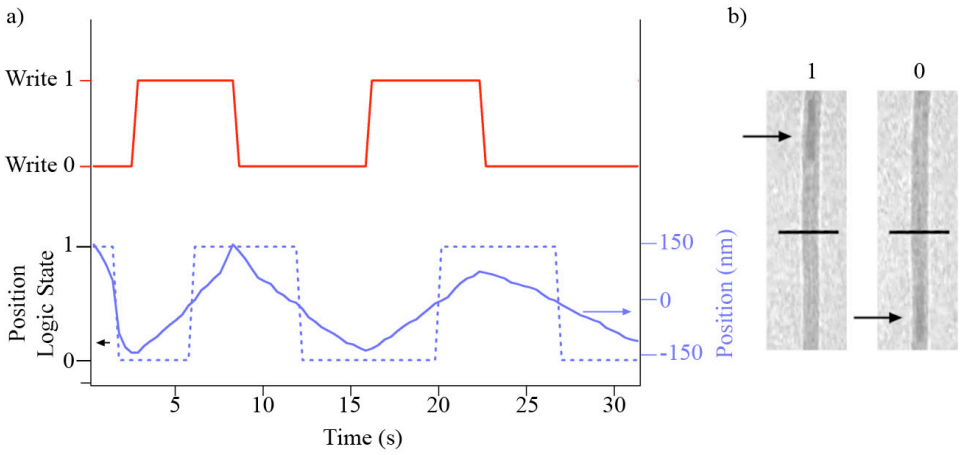

Figure 7.5: Position-Based Memory Device
The state of the memory device is here determined by the position of the nanoparticle shuttle, indicated at right. The plot shows the voltage write signal (top red line). Application of a '0' voltage causes the shuttle to move downward, creating a '0' state. Subsequent application of a '1' voltage causes the shuttle to move up, creating a '1' state. The bottom solid line is the measured position of the nanoparticle. The dashed line is the resulting memory state. The figures on the right show the device in the '1' and '0' state. The arrows identify the nanoparticle position. The solid line is the threshold between states.

signal causes the shuttle to move downward across the threshold position, yielding a '0' bit. The polarity of the write signal is switched in order to write a '1' bit. The shuttle moves upward and yields a '1' bit. The shuttle position is stable in the absence of a write signal, creating a robust non-volatile bit.

We note here that with our fine control of shuttle position, each memory device could potentially store much more than a single binary bit. For example, we could define a series of multiple thresholds along the nanotube, spaced ∼3 nm apart, and the position of the shuttle would thus determine which one of several hundred values is currently stored in the device. Unfortunately, for practical purposes, TEM observation is not a viable detection scheme. Thus, for this multiple-value memory device to be useful, a rapidly updating, on-chip position probe would be required.

7.7 Electrical Sensing

Fortunately, the electrical resistance of the nanotube device changes with translation of the shuttle, providing a means to read out the shuttle position without direct visual observation. This change in resistance is attributed to the iron nanoparticle's position-dependent contribution to the total device resistance, While this method is subject to noise and drift, it can repeatedly distinguish two extreme positions of the shuttle, confirming the viability of the device as an on-chip, binary memory storage element. Figure 7.6 inset shows the magnitude of the current as the shuttle moves back and forth (the data are concurrent with Figure 7.5). There is a clear correlation between the write voltage and the magnitude of the current. As the negative '0' write voltage is applied and the particle moves downward, the magnitude of the current increases. Likewise, as the positive '1' write voltage is applied and the particle moves upward, the magnitude of the current decreases. Therefore, the state of the bit can be probed with the electrical resistance.

Figure 7.6 shows the application of the shuttle as a two-terminal electrical read-out memory bit. As the system is constantly annealing during our high bias measurements[69], we consider a drift corrected resistance. Again, the system begins in a high resistance '1' state. We apply a '0' write voltage and the resistance drops with the downward movement of the shuttle until a resistance threshold is met and the bit flips to a low resistance '0' state. Reversal of the write bias causes the resistance to increase above the threshold and the bit flips back to the high resistance '1' state. In this measurement, the read and write voltage are the same. Alternatively, a low voltage could be used as a read voltage to non-destructively probe the state of the bit.

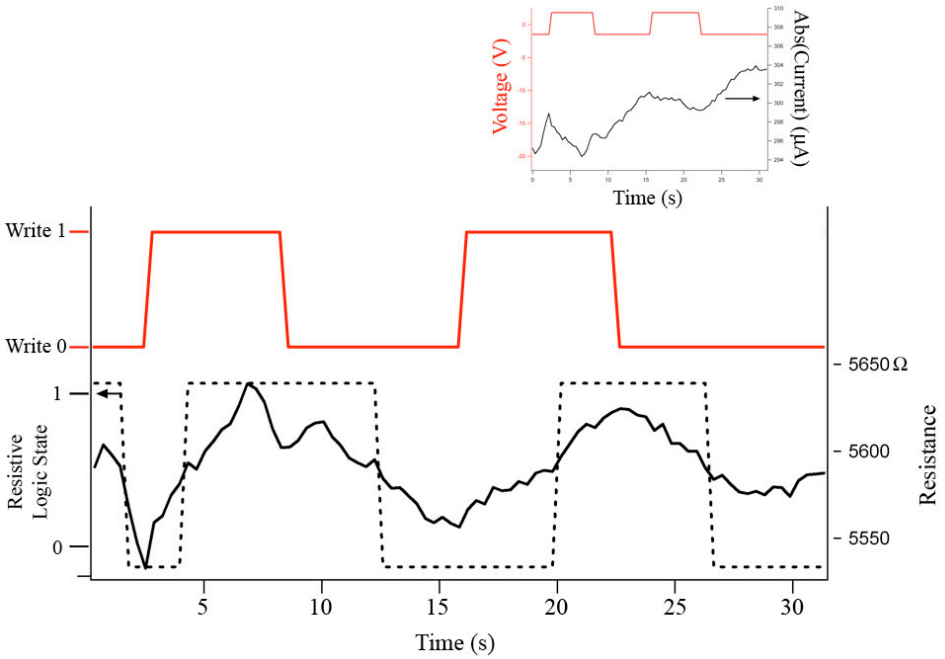

Figure 7.6: Resistance-Based Memory Device
The memory state is here determined by the drift corrected resistance of the device. In the main plot, the top red line shows the write signal, as described in figure 7.5. The solid black line shows the slope corrected resistance. High resistance is a '1' state and low resistance is a '0' state. The dashed line shows the memory state. The inset shows the magnitude of the current as the applied voltage the device is flipped. An overall drift in the magnitude is due to device annealing. However, even without slope correction, there is a clear correlation between the applied write voltage and the slope of the current.

7.8 Future Memory Devices

In order to achieve higher sensitivity read-out, one could employ a third probe, such as a gate electrode or a scanning probe similar to a hard drive read head. This third probe may be more sensitive to changes in the electrical properties of the nanotube system. Alternatively, a similar device could rely on the magnetic properties of the system [107, 108]. Application of current could be used to move the shuttle, as in this device, and therefore change the measured magnetic properties. It may be possible to write a new magnetic state in the presence of an external field. Such possible read-out mechanisms are depicted in Figure 7.7. With a variety of possible measurement types, electromigration based metal encapsulated nanoscale systems could form a new class of nonvolatile memory.

7.9 Archival Memory

Although there are tremendous benefits to continued miniaturization of memory to the nanoscale, there is an unfortunate general trend for memory storage, independent of medium, that device longevity decreases with increased memory density. For example, stone carvings in the Karnak Temple in Luxor with an approximate density of 2 bits/in^2 are largely readable after 3800 years, while information written with individual atoms by scanning tunneling microscopy manipulation[109] with a density $\sim$100 Tbits/in^2 have an estimated lifetime of only 10 ps at room temperature. Conventional digital memory configurations in use today, with densities of order 10-100 Gbits/in^2, have an estimated lifetime of only 10 to 30 years. Interestingly, the Domesday Book, the great survey of England commissioned by

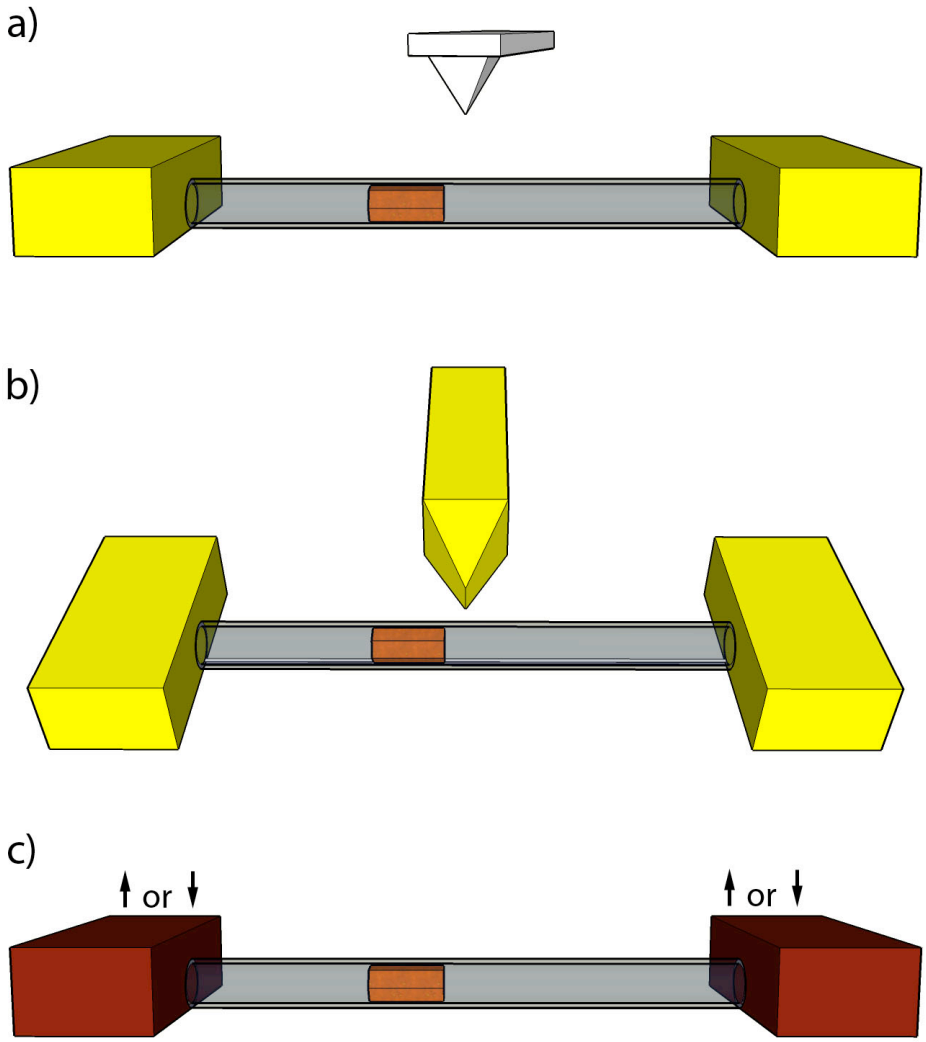

Figure 7.7: Future Memory Devices
(a) Readout of electrical or magnetic properties with an external scanning probe via MFM, EFM, KPM, or similar techniques. (b) Readout with local gate electrode. (c) Magnetic readout with magnetic contacts. Readout could be due to spin polarized transport. Applying current in an external field could be used to switch the state of the magnetic nanoparticle.

William the Conqueror in 1086 and written on vellum, has survived over 900 years, while the 1986 BBC Domesday Project, a multimedia survey marking the 900th anniversary of the original Book, required migration from the original high-density laserdiscs within two decades because of media failure[110].

The memory devices described here are both robust and high density. Such memory devices could be scaled to produce memory densities $\sim$1 Tbit/in^2, greater than current state of the art hard drive storage, with memory density $\sim$200 Gbit/in^2. The memory density could be increased by another order of magnitude or more by applying multiple thresholds to store many states per device. The memory unit can be written to and read out using two-terminal electrical leads operated at low voltages, facilitating large-scale integration, and is easily incorporated into conventional silicon processing. If the memory device is also extremeley stable, it could be suitable for archival storage applications.

7.9.1 Device Longevity

The unique geometry afforded by the encapsulated shuttle naturally yields a hermetically sealed system, immune to environmental contamination. In contrast to conventional memories, which may suffer from interaction between magnetic domains as well as material breakdown, the information in the shuttle memory is only compromised if the shuttle moves. We now turn to an examination of the expected lifetime of the memory device and written state.

Unlike most biological motor systems, the motion of the shuttle in the nanotube is not dominated by fluctuations (as in a Brownian ratchet), since a simple extrapolation

of the transport rate to $V \rightarrow 0$ shows that the undriven diffusive transport rate is negligible. A strong driving force from the external field/current is necessary to induce significant motion over experimental timescales. The interface between a well-ordered nanotube inner wall and a crystalline Fe nano-inclusion is expected to be relatively smooth for systems of this size, as required to obtain electromigratory motion at realistic currents, but it nevertheless should have kinetic barriers against stick-slip motion that are large compared to room-temperature thermal energies. (Even the extremely smooth interface between two incommensurate graphenic layers can develop some kinetic shear resistance due to structural relaxation and the iron-tube wall interaction is likely to be stronger than the interaction between two sp^2 carbon layers. Also, the iron lattice is more amenable to in-plane structural relaxation than is an extremely stiff sp^2 carbon lattice.[111]) For structurally well-ordered nanotube walls, the order-of-magnitude lengthscale L for this driven hopping is bounded below by the bcc iron or graphenic lattice constant, both on the order of 2 Å, since this distance sets the repeat distance for axial (achiral) or helical (chiral) motions of inclusions. For less-ordered tubes wherein motion of inclusions is pinned at structural imperfections, the characteristic step distance would be set by the separation between pinning sites; the ability experimentally to reduce the step size to less than 3 nm sets an upper limit on the importance of such disorder. Finally, depending on the elastic relaxation of the inclusion, hopping events may be identified with the motions of Frenkel-Kontorova domain walls that are internal to the iron inclusion.

We model the transport of the shuttle as occurring within a biased sawtooth potential, with thermally activated hops between local minima separated by a distance L,

assuming rapid equilibration within each local minimum. The unbiased (i.e. $V = 0$) barrier between minima is ΔE; the attempt rate is ω; the voltage across the tube is V. The length of the tube is D, so $\frac{V}{D}$ is the average electric field. The inclusion speed described by Equation 7.1 below.

$$v \sim \omega \cdot L \cdot e^{-\frac{\Delta E - \frac{1}{2} \cdot Q_{eff} \cdot V \cdot \frac{L}{D}}{kT}} \tag{7.1}$$

The effective charge Q_{eff} measures the strength of the coupling between the inclusion and the external electric field. Note that Q_{eff} embodies not just the direct (non-dissipative) coupling of charge to local electric field but also any effect of scattering events between the Fe inclusion and charge carriers in the nanotube. The local electric field near the inclusion may be larger than the average field between the electrodes if the vicinity of the inclusion experiences enhanced Ohmic dissipation. Therefore, although it has natural units of charge, Q_{eff} cannot be directly identified with the total charge on the inclusion. The observed exponential dependence of the speed on the applied voltage (shown in Figure 7.4), $\frac{\delta(log_{10} v)}{\delta V} \sim 30\ volt^{-1}$, sets the effective charge times the ratio of the step distance to the tube length (independent of ΔE, ω or kT): $Q_{eff} \cdot \frac{L}{D} \sim 1.5$ electron charges.

The attempt rate ω estimated from the characteristic center-of-mass vibrational mode of the inclusion ($\sim 10^9 s^{-1}$) is much lower than is typical for molecular-scale hopping events ($\sim 10^{12} s^{-1}$) since the inclusion is much heavier than a normal molecule. However, the dependence of the barrier height on the attempt rate (and the step length) is only logarithmic, and the other parameters are fairly well characterized, so the measured inclusion speeds allow one to estimate the lower bound of the barrier height as $\Delta E \sim 1.5 - 1.7 eV$.

The precise value of the barrier, and the resulting inclusion speeds, may be sensitive to the detailed structural parameters, such as the wrapping indices of the nanotube and the orientation of the Fe lattice with respect to the axis of the tube. Additional mechanisms for surmounting the kinetic barrier against motion, such as athermal fluctuations caused by instantaneous electron scattering events or a rapid ballistic passage over multiple successive barriers as facilitated by external fields, would tend to increase the estimate for the barrier size and hence further stabilize the system against purely thermal diffusive wandering.

To determine the lifetime of the memory device, we consider the motion of the iron shuttle at room temperature and zero bias over an appreciable enough distance to cause loss of information (here, 200 nm). The estimated barrier then yields a room-temperature dwell time greater than 3.3 x 10^{17} seconds. Thermodynamic stability in excess of a billion years demonstrates that the system should be extremely stable in the resting state and able to store information stably for any desired archival (even geologic) timescale. Nanoscale electromechanical memory devices such as those described here present a new solution to ultra-high density, archival data storage.

Part III

Ongoing Research

Chapter 8

Ongoing Research

8.1 Introduction

This chapter is dedicated to exploring some of the ongoing and future experiments related to the silicon nitride membranes. These studies are in preliminary phases, but will be continued by other members of the Zettl lab. Advances in membrane processing have allowed us to fully suspend nanostructures for highest resolution imaging. This allows *in situ* measurements of electromechanical devices such as nanotube resonators and rotational actuators as well as the fundamental studies of transport properties in SWCNT, DWCNT, and peapod structures. I also discuss new ways to engineer carbon nanotubes using applied current.

Many of these measurements will be especially fruitful when combined with the newly purchased liquid helium cold stage for the TEM. The stage was designed with transport measurements in mind and has electrical feedthroughs compatible with the membrane

devices.

8.2 High Resolution Imaging: Membrane Holes

For imaging and diffraction of small nanostructures, such as single- and double-walled nanotubes and peapods and silos, the thickness of the membrane causes too much interference to resolve important features, such as encapsulated buckyballs or individual walls. For higher resolution imaging and for measuring the properties of suspending structures such as for mechanical measurements, holes are etched in the membrane. We lithographically pattern holes (of any shape, here circles) as small as ∼10nm and then remove the Si_3N_4 with a SF_6 reactive ion etch. Nanostructures can then be suspended across the holes and contacted via standard lithography. The membranes are generally stable enough to withstand wet processing without the need for critical point drying.

Figure 8.1 shows the necessity for holes in membranes for high resolution imaging. Figure 8.1a shows a SWCNT and Figure 8.1b shows a DWCNT on and off of the Si_3N_4 membrane. Here the membrane is thinned, but it is still difficult to unambiguously determine the number of walls of the nanotube. These are relatively large nanotubes (d∼3-4nm). For smaller nanotubes (d∼1nm), it would difficult to resolve them at all.

8.2.1 Single- and Double-Walled Carbon Nanotubes

Figure 8.2 shows nanotubes grown across holes in a membrane. Catalyst is patterned or randomly dispersed on the membrane surface and the membranes are heated in a standard CVD process. This particular growth produced both single- and double-walled

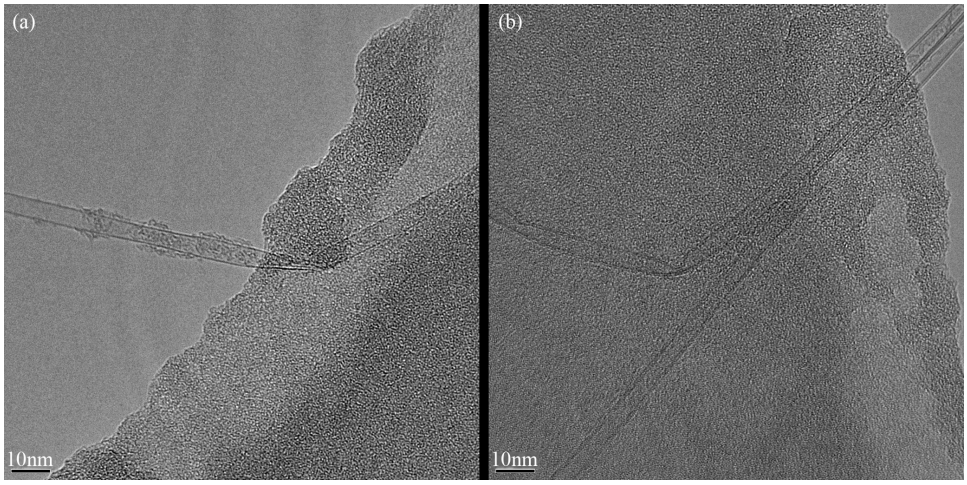

Figure 8.1: Effect of Membrane on TEM Resolution
(a) Single and (b) double-walled CNTs imaged on and off of the membranes, via the use of membrane holes. Notice that the membrane reduces the resolution of the imaging, which is especially critical for smaller nanostructures.

carbon nanotubes.

Figure 8.3 shows a SWCNT bridging a hole in a membrane. The diffraction pattern of this individual nanotube can be used to determine its chirality to be (36,12). However, due to distortions in our TEM and the nanotube's large diameter (d = 3.4nm), the assignment was not made conclusively. The effects of the distortions could be corrected by taking a reference pattern of the neighboring membrane.

Figure 8.4 shows two crossed DWCNTs and their diffraction pattern. In principle, the chirality of both nanotubes and all four walls could be independently determined. These nanotubes can be electrically contacted for a variety of experiments, including dynamics of crossed tube structures (e.g. cross-tube welding via electron irradiation and/or Joule heating) or electrical and mechanical coupling of nanotubes. Transport measurements of individual DWCNTs with determined chiralities could be used to probe the intrawall inter-

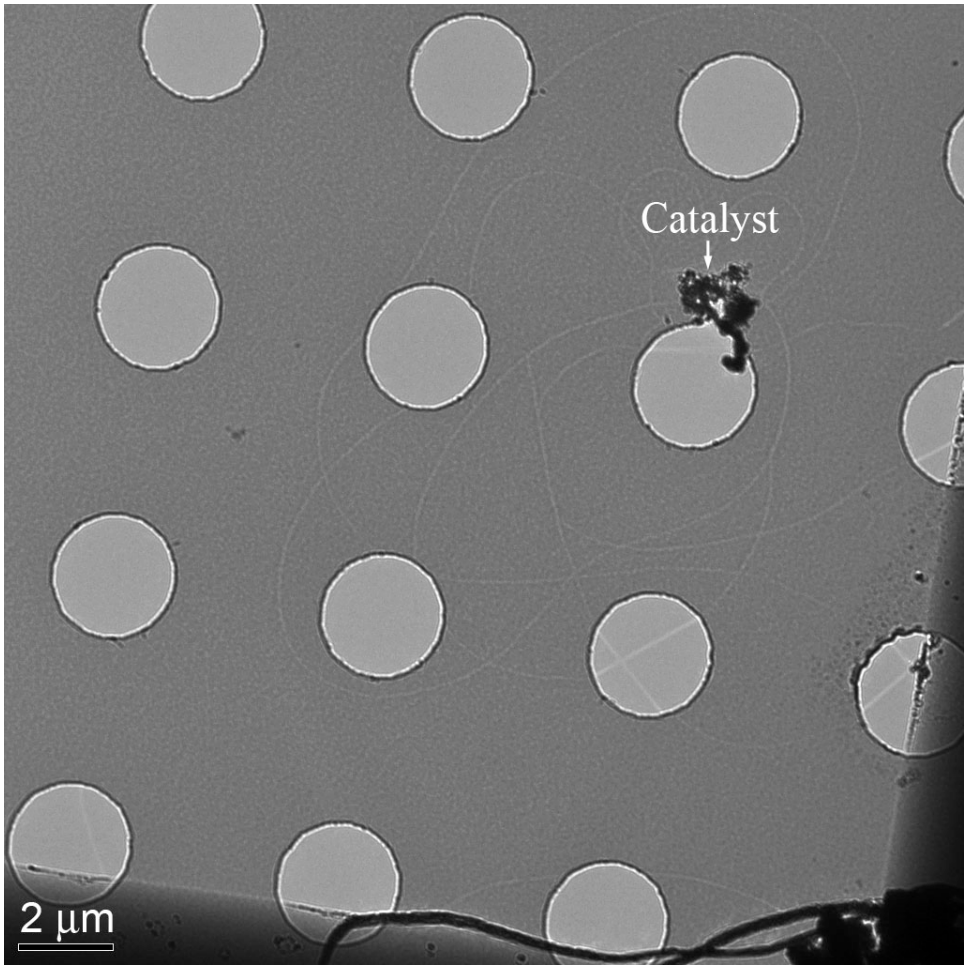

Figure 8.2: Nanotubes Grown via CVD on a Holey Membrane
The catalyst was randomly deposited and produces nanotubes that span the holes in the membrane.

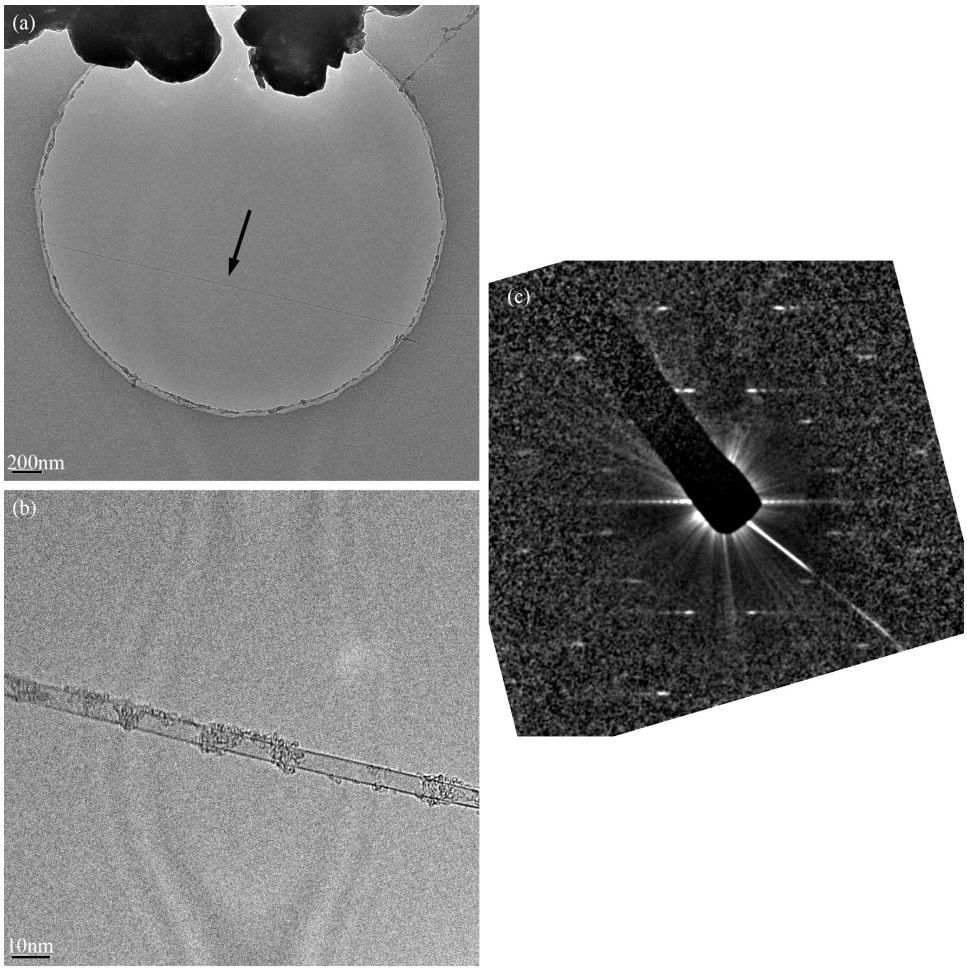

Figure 8.3: SWCNT Suspended Across a Hole
(a) Low resolution and (b) high resolution TEM images showing the single wall of a large diameter SWCNT. The accompanying diffraction pattern (c) can be used to determine the chirality of the nanotube, (36,12).

actions in a nanotubes. Specifically, the transport properties of the two interacting walls could be probed together and individually by removing the outer wall by electrical breakdown. This would yield important insight into the coupling between nanotube walls and their effect on multiwalled transport.

Similar studies could be performed on CNT peapods and BNNT silos, especially looking at the dynamics of the encapsulated buckyballs under applied electric field. These systems could have very interesting transport and mechanical properties. Additionally, the encapsulated buckyballs could be fused with the electron beam or with Joule heating

8.2.2 *In Situ* Rotational Actuators

Although etching holes in the membrane as described above allows high resolution imaging of suspended structures, it can be difficult to deposit nanostructures across the holes. Surface tension causes nanotubes to avoid the holes, prohibiting deposition by spin casting from liquid. To solve this problem, we use an alternative method to create holes. During the batch fabrication of the membranes (described in Appendix A), the final wet etch is stopped early to leave the supporting SiO_2 under the Si_3N_4 membrane. Now, holes etched through the Si_3N_4 layer are only ~10nm dimples in the surface. Nanostructures are deposited across these dimples and contacted without difficulty. The underlying SiO_2 layer is then etched away with a wet etch (either KOH or HF).

Suspended nanotube rotors are fabricated as described above. Figure 8.5 shows MWCNTs with gold contacts and a gold paddle before and after the wet etch of the SiO_2. The rotor can be actuated using the nearby side gates. By observing the nanotube and

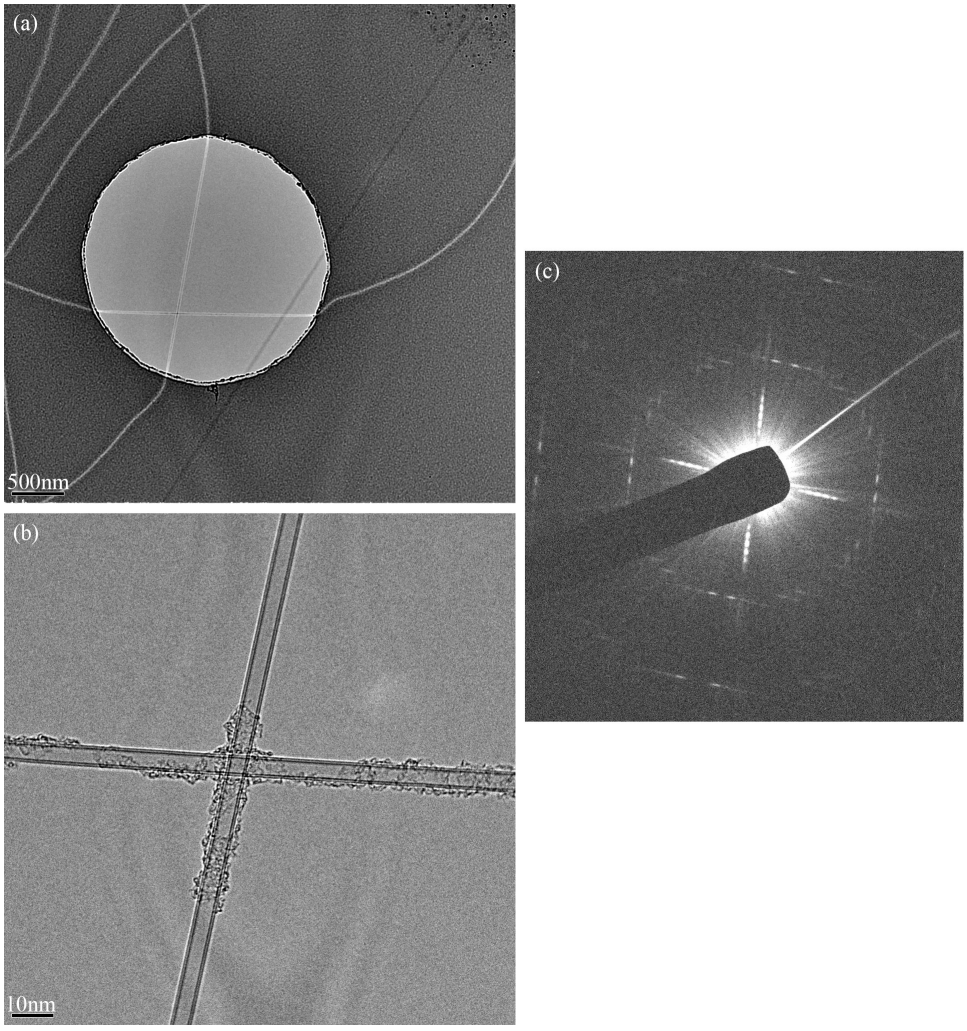

Figure 8.4: Crossed DWCNTs Suspended Across a Hole
(a) Low resolution and (b) high resolution TEM images showing two large diameter DWCNTs crossing. The individual walls can be observed. The accompanying diffraction pattern (c) shows diffraction spots from each of the walls from both nanotubes and could be used to determine the chirality of all the walls. Observation of the nanotubes and their diffraction pattern could be performed in real time with concurrent electrical measurements.

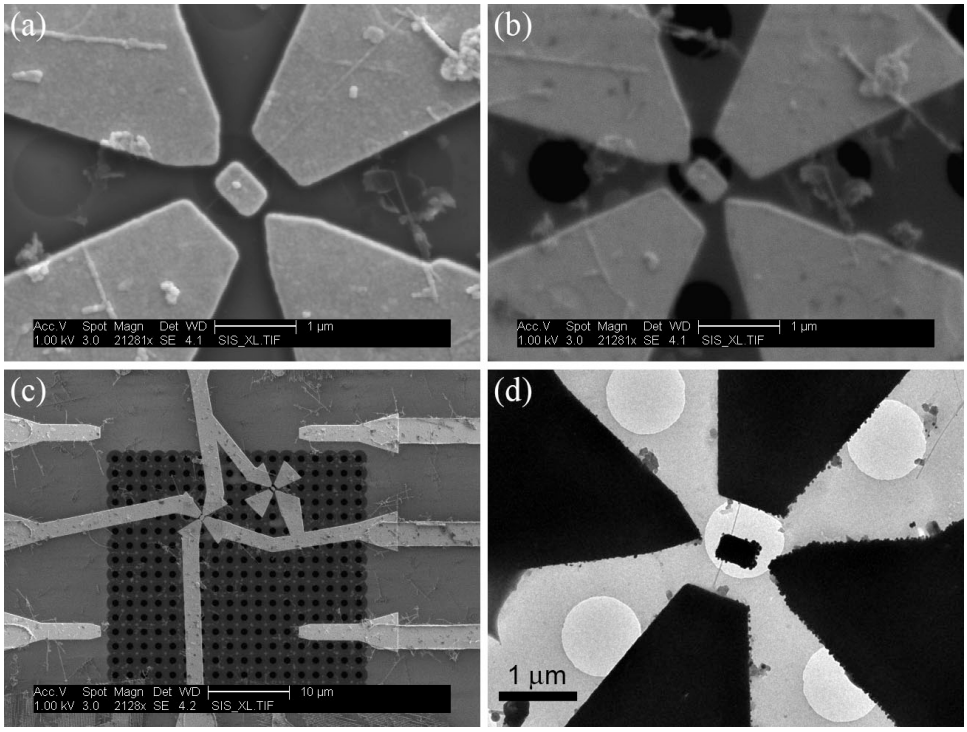

Figure 8.5: Rotational Actuators on a Si_3N_4 Membrane
SEM images of suspended rotors on a holey membrane (a) before and (b) after wet etching the supporting SiO_2. (c) Low resolution SEM image of the and entire membrane, showing multiple rotor devices. (d) TEM image of a fully suspended and electrically contacted rotor.

its diffraction in the TEM, we can study the twisting properties of a nanotube and the interaction between walls. For example, we could determine how many walls are actuated by a deposited paddle. If the rotors were built on SWCNTs, we could study the effect of torsion on transport properties and relate it to the effective change in chirality due to twisting. With a DWCNT, we could learn about the current carrying capacity of, and interaction between, each wall with correlation to their chiralities.

Similarly, Figure 8.6 shows a rotational actuators fabricated on Si/$Si0_2$ substrates and suspended by underetching the SiO_2 (not on a Si_3N_4 membrane). Such samples could be used to probe the transport properties of BNNT by flexing the rotor with applied elec-

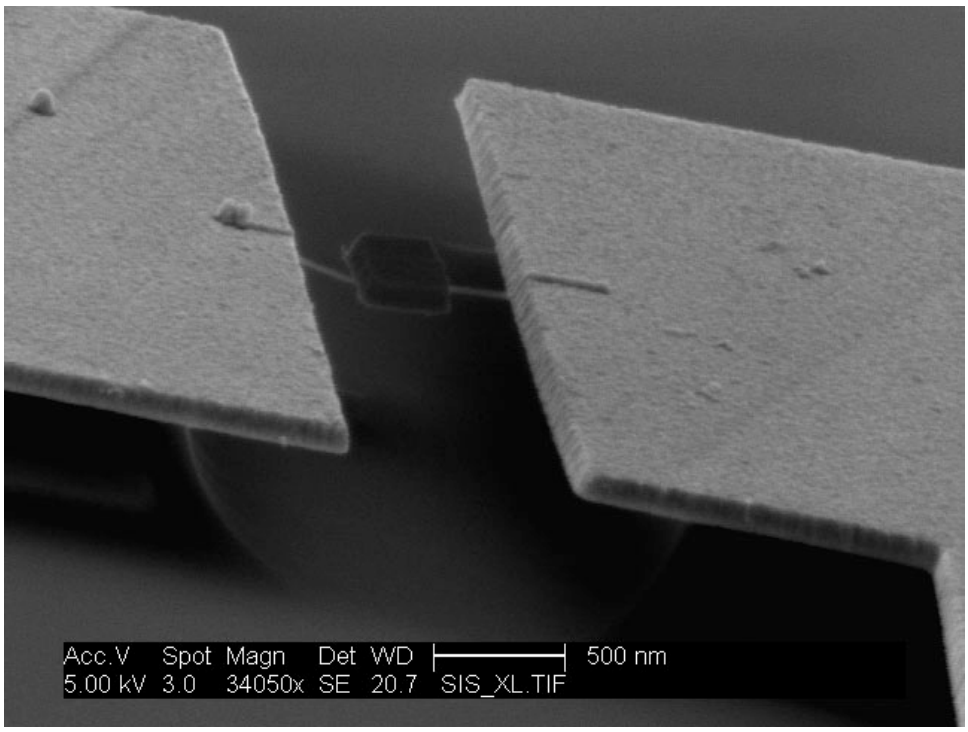

Figure 8.6: BNNT Rotational Actuator
This actuator can be used to study the electrical properties, and particularly the piezoelectric properties, of BNNTs.

trical field or by probing with a scanning probe. Measurements of the electrical properties during torsion and bending could produce insight into potential piezoelectric properties. We suggest that electrical measurements with a conducting SPM tip pushing on the paddle could especially provide insight. It may be best to position the rotor off-center on the nanotube, in order to avoid cancelation of the measured effect due to symmetry.

8.3 Tunable Resonators

The low density and high Young's modulus of carbon nanotube make them a good candidate for nanoscale resonators. There has been progress in the creation of CNT

resonator devices, but they generally operate at a fixed frequency, or can be tuned over a limited range such as by electrostatic tensioning[112, 24].

Kenneth Jensen has made progress in tuning a nanotube resonator over a broad range by employing the telescoping properties of MWCNTs[44, 47]. A single MWCNT is addressed in an *in situ* pizeomanipulation stage. The outer walls of the nanotubes are partially removed via field emission so that the inner walls can be spot welded to the movable contact. Moving the spot welded contact causes the inner walls to slide with respect to the outer walls of the nanotube. The effective length of the resonator can therefore be adjusted and the resonant frequency of the resonator can be tuned. This elegant approach is fundamentally different than previous designs, and is particularly interesting in that the effect can be understood by simple analogy to a guitar whose strings are artificially shortened temporarily to generate the correct note. However, the design requires specialized equipment and is not easily converted to scalable devices. We offer a similar approach inspired by this one that features simple fabrication.

By utilizing the electromigration of metals encapsulated within or deposited onto nanotubes (see Chapter 7), we can control the resonant properties of a nanotube resonator. This is illustrated in Figure 8.7b. An iron-filled nanotube device has been fully suspended by back etching the membrane with a SF_6 reactive ion etch (RIE) after device fabrication. The iron in the nanotube alters the local density of the resonator and therefore affects its resonant frequency. The iron can then be moved, changing the mass distribution of the resonator. If a small nanoparticle were used, it might act as a moveable node. For a large filling such as that shown in Figure 8.7b, the iron may act more like a moving clamp,

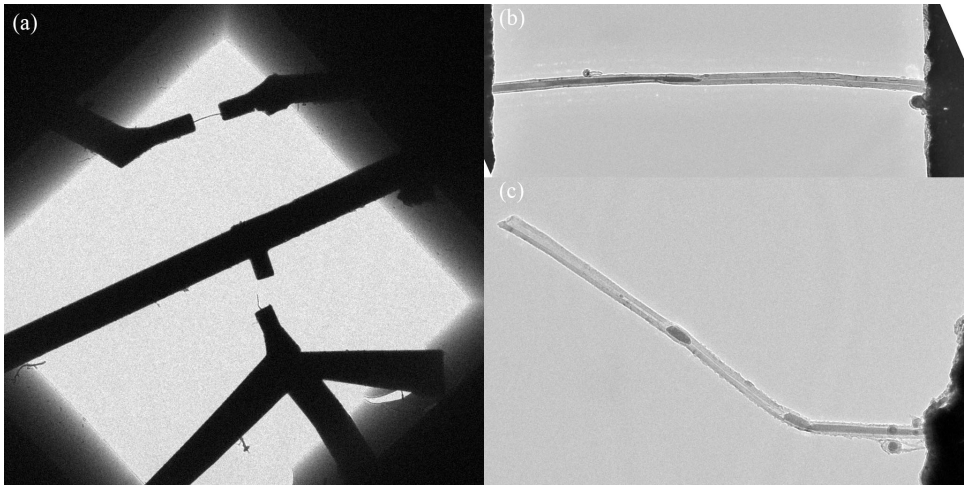

Figure 8.7: Electromigration Based Tunable Resonator Devices
(a) Two devices completely suspended by RIE of the Si_3N_4 membrane. (b) A suspended iron-filled MWCNT could be resonate with a tunable frequency by moving the iron filling. In a case such as this, with large filling, the iron would act like a clamp. With a single small iron nanoparticle, movement could be similar to moving a node. (c) A singly contacted iron-filled CNT with a local counter electrode can be operated in field emission mode. Movement of the iron could be used for non-destructive tuning with potential application in a nanotube radio.

changing the effective length of the resonator.

Figure 8.7c shows the application of an iron encapsulated as a tunable resonator in field emission mode. A nanotube with only one contact and a removed counter electrode is fully suspended via RIE. The iron could be moved via the field emission current and therefore be used for non-destructive tuning of a device similar to the nanotube radio[113]. This study is being continued by Kwanpyo Kim.

The advantage of an approach utilizing encapsulated metals for tunable resonators is that they could easily be made into standard devices. By wiring up the nanotubes as synthesized and using appropriate etching techniques to suspend them, these nanotubes would be tunable without further processing.

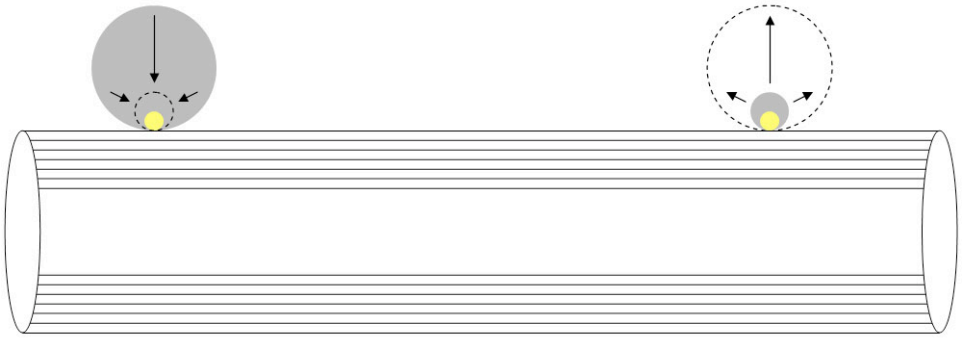

Figure 8.8: Controlled Nucleation site of In/Sn Electromigration for Tunable Resonators or Memory Devices
Small metal (e.g. gold) nanoparticles can be act as nucleation sites for electromigrating materials such as indium or tin on the outside of a nanotube. Patterning such nucleation sites would allow controlled multistate systems for tunable resonators or memory devices similar to those discussed in Chapter 7

Alternatively, metals could be deposited on the outside of the nanotube[48] (such as indium or tin) and shuttled to produce a similar effect. We have found that by using a high melting point metal, such as Gold, one could create stable nucleation sites for moving indium or tin. This is depicted schematically in Figure 8.8 in a configuration similar to a two state memory or two state resonator. The large indium shuttle will move back and forth along the MWCNT scaffold but will nucleate preferentially at the defined sites, which could be patterned, for example by lithography. This study is being continued by Will Gannett.

8.4 Engineering Carbon Nanotubes

Carbon nanotubes geometry can be engineered in many ways to suit the needs of an application. For example, one can cut through a CNT (partially or completely) with an electron beam[114] or scanning probe[115]. Figure 8.9 shows irradiation damage to a MWCNT and the supporting Si_3N_4 membrane from a concentrated electron beam.

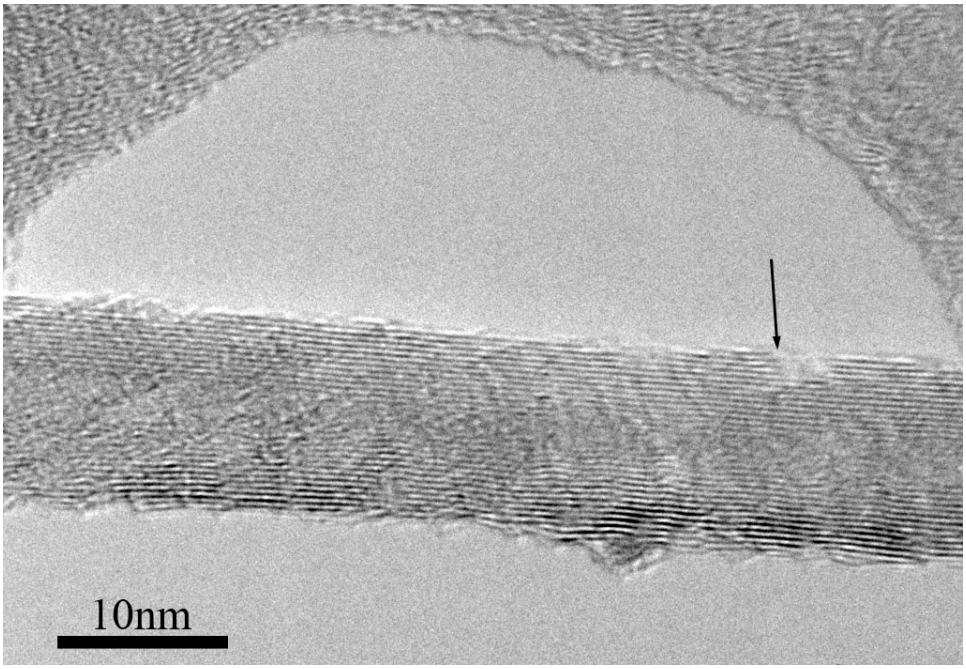

Figure 8.9: Electron Beam Irradiation Damage to a MWCNT and the Supporting Si_3N_4 Membrane
The arrow shows one location of damaged nanotube walls. The hole in the membrane is due to the irradiation.

Or, as has been discussed previously, one can use electrical breakdown to remove walls of a MWCNT. Here we show a method to create partially removed walls for increased surface area and a method to create nanoscale gaps for molecular transport measurements or enhanced field emission devices. We also suggest a method for selectively growing new walls on a nanotube.

Figure 8.10 shows three ways to engineer the number of walls in a MWCNT. In the first case, walls are removed by electrical breakdown. In the second case, walls are removed partially to increase the surface area of the nanotube. In the third case a wall is grown selectively on a MWCNT.

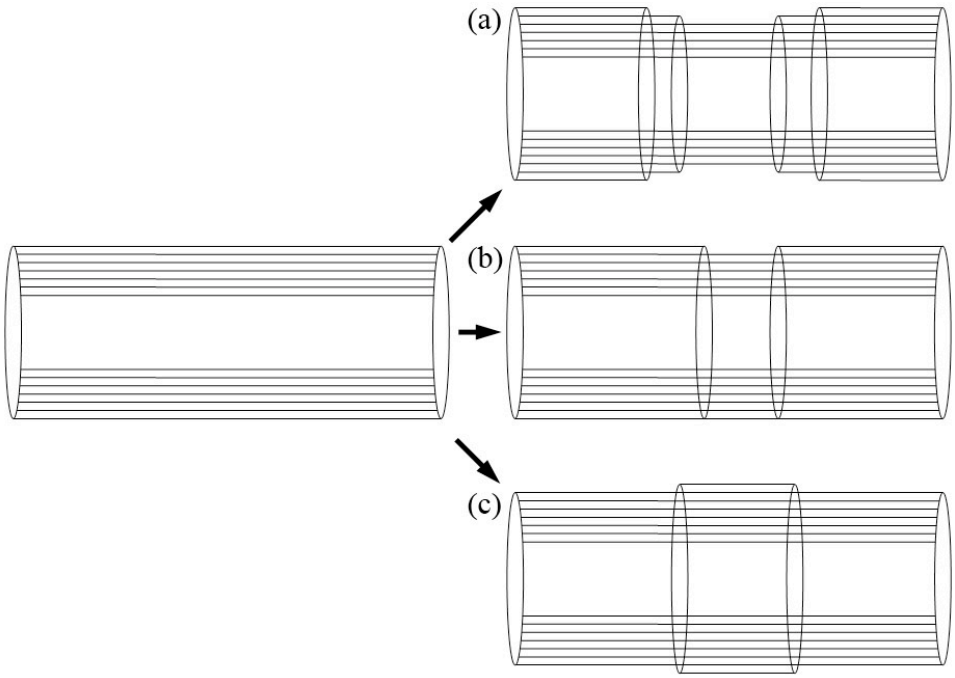

Figure 8.10: Engineering a Carbon Nanotube
Three routes to engineer the number of walls of a MWCNT. (a) Wall removal, as by electrical breakdown. (b) Partial wall removal. (c) Selective growth of a new wall.

8.4.1 Partial Removal of Nanotube Walls

Iron on the outside of a MWCNT can be used to selectively remove the outer walls of the nanotube. We coat a nanotube on a membrane device with a thin layer of iron (<10 Å) and apply bias to the MWCNT to cause Joule heating. Figure 8.11 shows how the nanotube becomes damaged by the iron. Iron nanoparticles move randomly on the surface but do not electromigrate as observed in encapsulated iron. The nanotubes remain conductive even when greatly damaged. It is expected that the iron is absorbing carbon from the walls of the MWCNT, thereby removing carbon from its sp^2 bonds. This might be confirmed by performing diffraction of the iron before and after heating.

This technique could be used to greatly increase the surface area of carbon nanotubes for such applications as chemical sensing and hydrogen storage. For such large scale application, high surface energy nanotubes could be synthesized by coating nanotube mats with iron or iron nanoparticles and heating them in a furnace.

8.4.2 Nanotube Gaps

Figure 8.12 shows the creation of small gaps in MWCNT devices. These are created by application of electrical pulses, which rapidly heat the center of the nanotube devices. This was discovered serendipitously when some of our samples suffered electrostatic discharge while loading into the TEM.

The nanotube breakdown is often accompanied by a small hole in the membrane. This self aligned pore allows unmitigated imaging in the TEM. If this system were used as leads for molecular transport measurements, one could unambiguously confirm that only

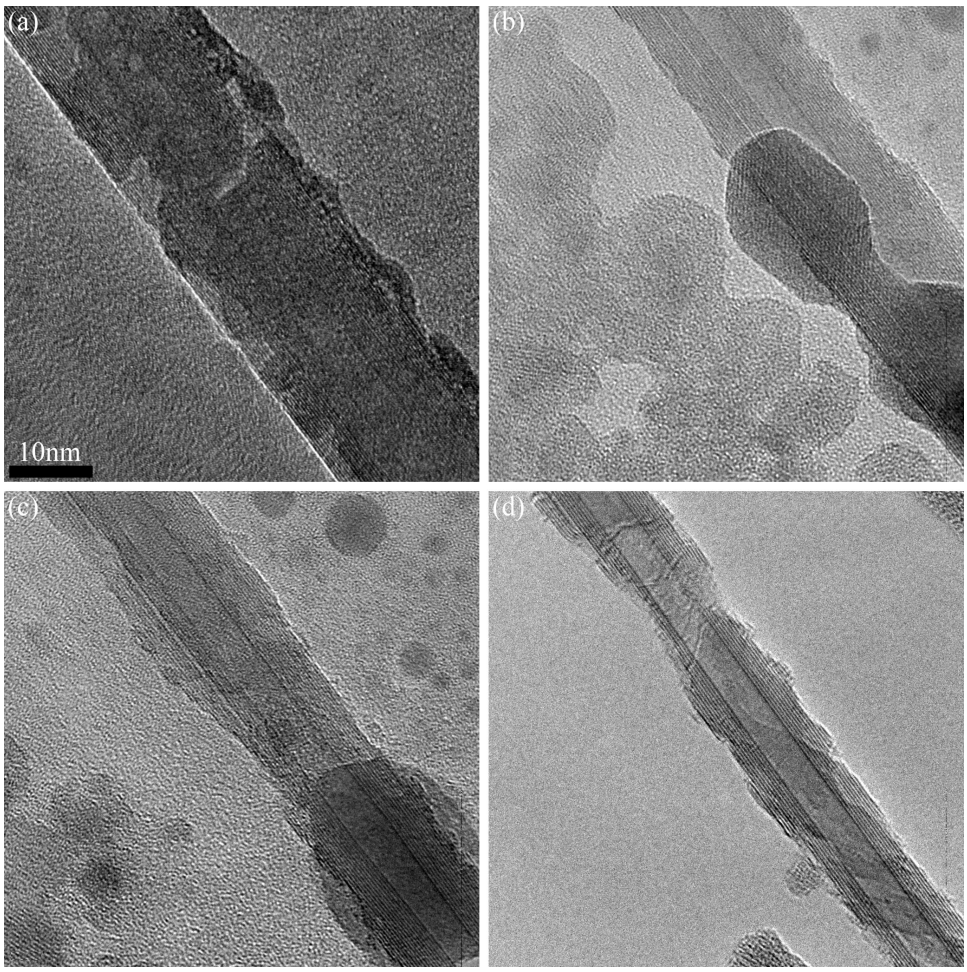

Figure 8.11: Partial Wall Removal of MWCNTs
(a) A pristine MWCNT coated with a thin layer or iron. (b-d) The MWCNT is Joule heated and the iron causes the removal of carbon from the walls. The nanotube is progressively modified resulting in a nanotube that still conducts but may be exhibit high sensitivity and surface area, with application for chemical sensors and hydrogen storage.

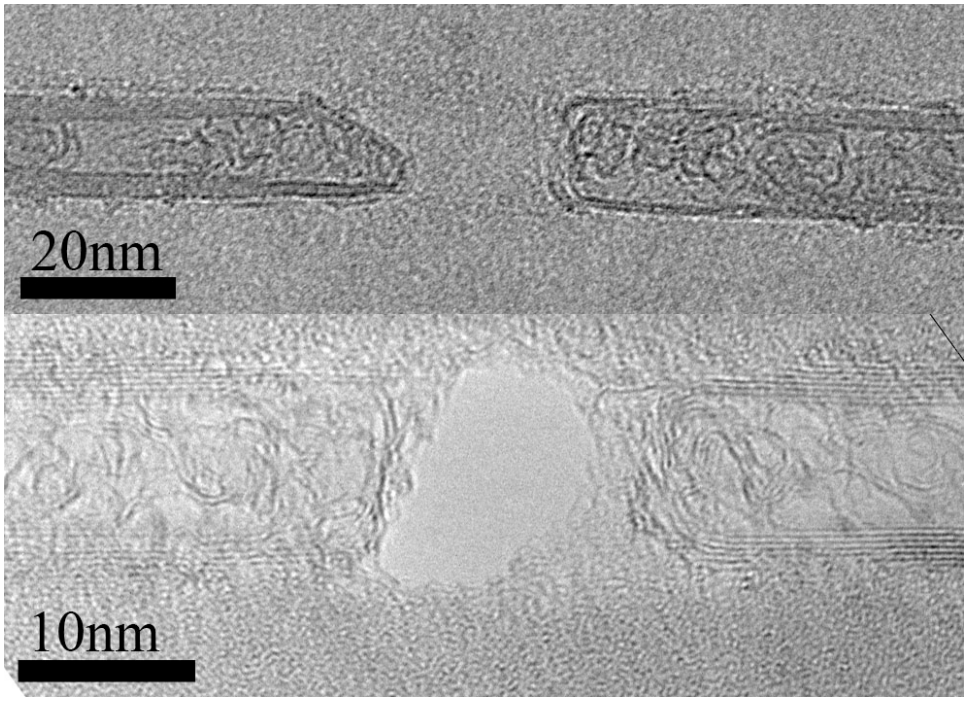

Figure 8.12: Nanotube Gaps
Small gaps in MWCNT devices caused by rapid electrical breakdown. These gaps have been created as small as a few nanometers and could be made smaller with SWCNTs. (b) A hole in the Si_3N_4 membrane caused by the breakdown is aligned to the nanotube electrodes. This is an ideal platform for nanofluidic measurements. Combined with organic linkers to the ends of the nanotubes, this platform could eb used for measuring specific biological or chemical targets.

one molecule was bridging the contacts. In order to create a device with a higher number of nanotube contacts, a cross-nanotube configuration could be employed, such as that shown in Figure 8.4. By applying an electrical pulse from one nanotube to the other, it is likely that both would blowout at the cross due to contact resistance between the nanotubes, creating a four terminal system. The potential resulting asymmetry of the leads would allow one set to be used as extremely local gate electrodes. Additionally, since this hole in the membrane is self-aligned to the contacts, this platform is suitable for nanofluidic measurements. By employing the great chemical versatility of the carbon nanotube, the leads could be designed to preferentially bind to biological or chemical targets. For example, such a system could be used to measure the electrical conductivity of a biological molecule (such as DNA) as it is pulled through the pore.

Additionally, these small gaps could be used as tip-to-tip field emission devices. Suspended in a standard device orientation through simple fabrication techniques, these devices could act on-chip sensors or nanotube radios.

8.4.3 Selective Growth of Nanotube Walls

In addition to removing carbon from a nanotube, we suggest a method to selectively grow partial walls on MWCNTs. Amorphous carbon can be selectively deposited on the outside of the nanotube using an electron beam[116] or via lithography. The sample is then heated in vacuum, for example with Joule self heating, in order to crystallize the amorphous carbon into a graphitic wall. These results are in early stages and are being explored by Will Gannett.

8.5 Graphene

Graphene is a new material that has generated great interest in the last few years. In addition to its unique electronic properties, it can serve as an ultrathin support for TEM, allowing imaging of light atoms[117]. *In situ* transport properties of graphene could yield great insight into its transport and mechanical properties as well as its potential applications. Due to it's low density (low TEM contrast) and electrical conductivity, electrically contacted graphene could be unparalleled as a support structure for the study of dynamics of nanostructures, molecules, and atoms. For example, the dynamics of defects in graphene or molecules adsorbed onto the graphene could be controlled with application of current and observed in real time. Additionally, the electrical properties and breakdown of the graphene itself could be studied, similar to our studies of nanotubes. The thin graphene membrane could also serve as a support for two-dimensional mass transport of metals.

We create a freestanding electrically contacted graphene membrane by transferring a graphene sheet onto a holey membrane with prefabricated contacts, as shown in Figure 8.13. The graphene is in contact with four gold leads and is fully suspended over a hole in the Si_3N_4 membrane. The membrane is prepared by patterning the electrical contacts and then patterning and etching the holes aligned to the contacts. The thin layered graphene is prepared by the well established "scotch tape" method. The graphene is located on a silicon oxide substrate using an optical microscope and lifted off onto a Quantifoil electron microscopy grids (200 Mesh Gold, 1.3 μm holes, Quantifoil Micro Tools GmbH, Jena, Germany) in liquid. The grid is then positioned over the membrane wetted with acetone to form intimate contact. After drying, the Quantifoil grid is pulled off, leaving the amorphous

carbon from the Quantifoil, which can be removed via oxidation.

The large hole in the membrane is aligned with the holes in the Quantifoil, creating a portion of the graphene that is completely suspended. In the sample, indium has been deposited on the graphene for mass transport studies. The indium should move along the graphene via electromigration. The use of four independent electrical contacts to the graphene allows two-dimensional control of the indium nanoparticle. Notice that the indium does not stick well to the clean graphene, as only a few dark particles can be seen. This may be indicating that the indium preferentially sits on defect locations. This is consistent with our observations in mass transport of indium on MWCNT, where we have attempted to create defect sites to control nucleation locations of indium during mass transport. As we are able to locate individual defects in graphene by TEM imaging, we could map the defects before depositing indium in order to confirm their role in nucleation. By controlling the location of defects (which could be created by electron beam irradiation and potentially moved controllably with application of current), we could create stable sites for indium. Such a multistate system could be used as a memory device, as discussed earlier.

The engineering of graphene is likely similar to that of MWCNTs. It is likely that through application of current, electron irradiation, and electron beam assisted deposition of amorphous carbon, we could create defects, heal defects, cut the graphene, or even create customizable multiple graphene layers.

This project is ongoing and is spearheaded by Brian Kessler.

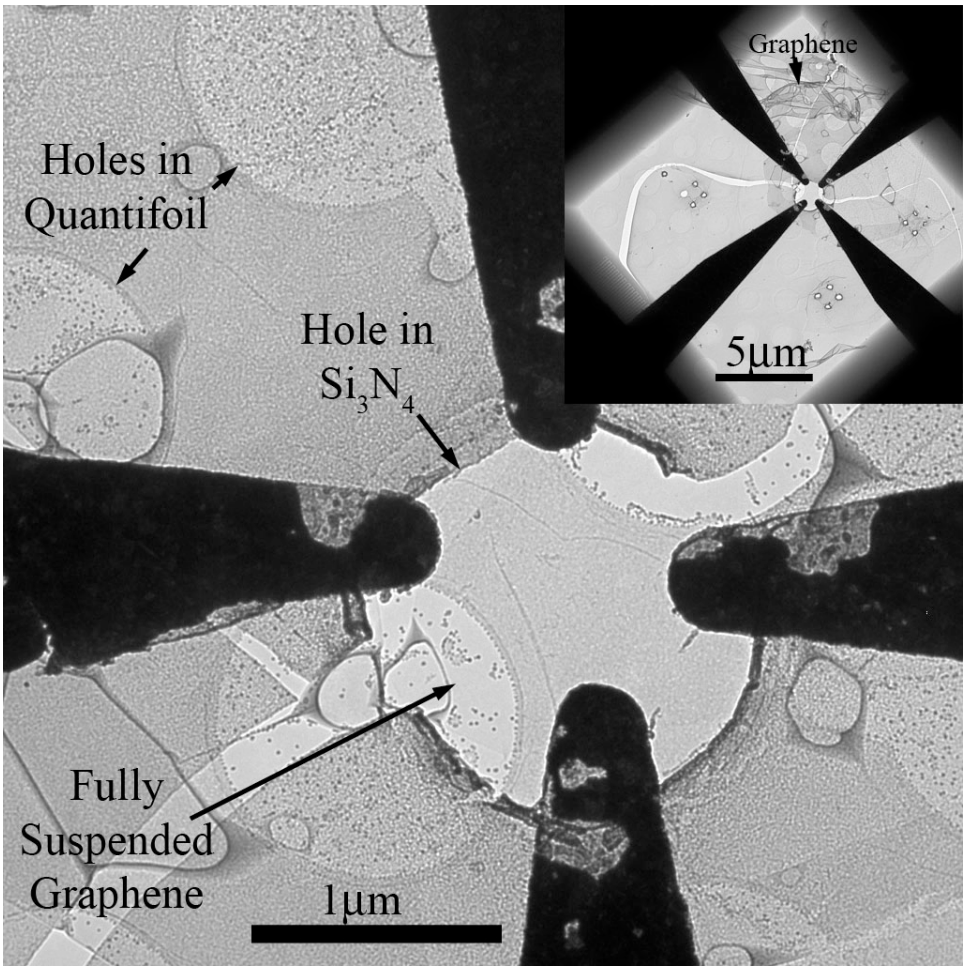

Figure 8.13: Electrically Contacted Suspended Graphene Sheet
Graphene has been deposited from a Quantifoil grid onto prefabricated contacts on a holey membrane. The inset shows a low magnification image of the entire membrane. The holes in the Quantifoil align with the hole in the membrane to produce a fully suspended graphene sheet. Indium has been deposited on the graphene to be used as a 2D mass transport system. Notice that the indium does not uniformly coat the graphene, but rather clusters, indicating probable locations of defects. Such a platform could be used for many studies of graphene and supported materials.

Bibliography

[1] R. Feynman, Microelectromechanical Systems, Journal of **1**, 60 (1992).

[2] A. M. Fennimore et al., Nature **424**, 408 (2003).

[3] S. Iijima, Nature **354**, 56 (1991).

[4] R. Saito, G. Dresselhaus, and M. S. Dresselhaus, *Physical Properties of Carbon Nanotubes*, Imperial College Press, London, 1998.

[5] N. G. Chopra et al., Science **269**, 966 (1995).

[6] M. Ishigami et al., Physical Review Letters **93** (2004).

[7] P. G. Collins, K. Bradley, M. Ishigami, and A. Zettl, Science **287**, 1801 (2000).

[8] T. Durkop, S. Getty, E. Cobas, and M. Fuhrer, Nano Letters **4**, 35 (2004).

[9] R. Moradian, S. Azadi, and H. Refii-tabar, Journal of Physics: Condensed Matter , 176209 (2007).

[10] L.-C. Qin et al., Nature **408**, 50 (2000).

[11] Z. K. Tang et al., Science **292**, 2462 (2001).

[12] T. Guo et al., Journal of Physical Chemistry **99**, 10694 (1995).

[13] T. W. Ebbesen and P. M. Ajayan, Nature **358**, 220 (1992).

[14] W. Z. Li et al., Science **274**, 1701 (1996).

[15] C. Journet et al., Nature **388**, 756 (1997).

[16] L. X. Zheng et al., Nature Materials **3**, 673 (2004).

[17] K. Hata et al., Science **306**, 1362 (2004).

[18] S. J. Tans, A. R. M. Verschueren, and C. Dekker, Nature **393**, 49 (1998).

[19] J. A. Misewich et al., Science **300**, 783 (2003).

[20] W. A. Deheer, A. Chatelain, and D. Ugarte, Science **270**, 1179 (1995).

[21] Q. H. Wang et al., Applied Physics Letters **72**, 2912 (1998).

[22] S. J. Papadakis et al., Physical Review Letters **93** (2004).

[23] H. B. Peng, C. W. Chang, S. Aloni, T. D. Yuzvinsky, and A. Zettl, Physical Review Letters **97**, 087203 (2006).

[24] V. Sazonova et al., Nature **431**, 284 (2004).

[25] T. Rueckes et al., Science **289**, 94 (2000).

[26] L. Langer et al., Journal of Materials Research **9**, 927 (1994).

[27] H. Dai, E. W. Wong, and C. M. Lieber, Science **272**, 523 (1996).

[28] T. W. Ebbesen et al., Nature **382**, 54 (1996).

[29] L. Langer et al., Physical Review Letters **76**, 479 LP (1996).

[30] A. Bezryadin, A. R. M. Verschueren, S. J. Tans, and C. Dekker, Physical Review Letters **80**, 4036 LP (1998).

[31] S. J. Tans et al., Nature **386**, 474 (1997).

[32] J. W. G. Wilder, L. C. Venema, A. G. Rinzler, R. E. Smalley, and C. Dekker, Nature **391**, 59 (1998).

[33] B. J. Leroy, I. Heller, V. K. Pahilwani, C. Dekker, and S. G. Lemay, Nano Letters **7**, 2937 (2007).

[34] A. Jorio et al., Physical Review Letters **86**, 1118 (2001).

[35] S. M. Bachilo et al., Science **298**, 2361 (2002).

[36] Z. Liu and L.-C. Qin, Chemical Physics Letters **408**, 75 (2005).

[37] J. C. Meyer, M. Paillet, G. S. Duesberg, and S. Roth, Ultramicroscopy **106**, 176 (2006).

[38] M. Gao, J. M. Zuo, R. Zhang, and L. A. Nagahara, Journal of Materials Science **41**, 4382 (2006).

[39] H. Zhu, K. Suenaga, A. Hashimoto, K. Urita, and S. Iijima, Chemical Physics Letters **412**, 116 (2005).

[40] J. C. Meyer et al., Nano Letters (2008).

[41] K. Suenaga et al., Nature Nanotechnology **2**, 358 (2007).

[42] B. W. Smith, M. Monthioux, and D. E. Luzzi, Nature **396**, 323 (1998).

[43] J. Cumings, P. G. Collins, and A. Zettl, Nature **406**, 586 (2000).

[44] J. Cumings and A. Zettl, Science **289**, 602 (2000).

[45] J. Cumings and A. Zettl, Physical Review Letters **93**, 086801 (2004).

[46] C. Jin, K. Suenaga, and S. Lijima, Nano Letters **8**, 1127 (2008).

[47] K. Jensen, C. Girit, W. Mickelson, and A. Zettl, Physical Review Letters **96** (2006).

[48] B. C. Regan, S. Aloni, R. O. Ritchie, U. Dahmen, and A. Zettl, Nature **428**, 924 (2004).

[49] D. Golberg et al., Advanced Materials **19**, 1937 (2007).

[50] K. Svensson, H. Olin, and E. Olsson, Physical Review Letters **93** (2004).

[51] K. Jensen, W. Mickelson, W. Han, and A. Zettl, Applied Physics Letters **86**, 173107 (2005).

[52] L. X. Dong, X. Y. Tao, L. Zhang, X. B. Zhang, and B. J. Nelson, Nano Letters **7**, 58 (2007).

[53] C. H. Jin, K. Suenaga, and S. Iijima, Nature Nanotechnology **3**, 17 (2008).

[54] Z. L. Wang, R. P. Gao, W. A. de Heer, and P. Poncharal, Applied Physics Letters **80**, 856 (2002).

[55] A. Kis, K. Jensen, S. Aloni, W. Mickelson, and A. Zettl, Physical Review Letters **97** (2006).

[56] J. C. Meyer, M. Paillet, and S. Roth, Science **309**, 1539 (2005).

[57] J. C. Meyer et al., Physical Review Letters **95**, 217401 (2005).

[58] J. C. Meyer, D. Obergfell, S. Roth, S. Yang, and S. Yang, Applied Physics Letters **85**, 2911 (2004).

[59] X. M. H. Huang et al., Nano Letters **5**, 1515 (2005).

[60] M. Y. Sfeir et al., Science **306**, 1540 (2004).

[61] B. Chandra et al., Physica Status Solidi B-Basic Solid State Physics **243**, 3359 (2006).

[62] J. Chen, M. A. Reed, A. M. Rawlett, and J. M. Tour, Science **286**, 1550 (1999).

[63] M. M. Deshmukh, D. C. Ralph, M. Thomas, and J. Silcox, Applied Physics Letters **75**, 1631 (1999).

[64] H. Tong et al., Nano Letters **4**, 283 (2004).

[65] J. Li et al., Nature **412**, 166 (2001).

[66] S. Chikkannanavar, D. Luzzi, S. Paulson, and A. Johnson, Nano Letters **5**, 151 (2005).

[67] T. D. Yuzvinsky, *Carbon nanotubes for nanoscale electronics and nanoelectromechanical systems*, PhD thesis, University of California, Berkeley, 2006.

[68] P. G. Collins, M. Hersam, M. Arnold, R. Martel, and P. Avouris, Physical Review Letters **86**, 3128 (2001).

[69] T. D. Yuzvinsky et al., Applied Physics Letters **87** (2005).

[70] T. D. Yuzvinsky et al., Nano Letters **6**, 2718 (2006).

[71] P. M. Ajayan et al., Nature **362**, 522 (1993).

[72] H. Y. Chiu et al., Physical Review Letters **95** (2005).

[73] T. Evans and P. F. James, Proceedings of the Royal Society of London. Series A, Mathematical and Physical Sciences **277**, 260 (1964).

[74] J. Haines and C. Tsai, *Graphite Sublimation Tests for the Muon-Collider/Neutrino Factory Target Development Program*, U.S. Department of Energy, Office of Science, 2002.

[75] Y. Miyamoto, S. Berber, M. Yoon, A. Rubio, and D. Tomnek, Physica B **323**, 78 (2002).

[76] X. Cai, S. Akita, and Y. Nakayama, Thin Solid Films **464-465**, 364 (2004).

[77] J. Y. Huang et al., Physical Review Letters **94**, 236802 (2005).

[78] P. Kim, L. Shi, A. Majumdar, and P. L. McEuen, Physical Review Letters **87**, 215502 (2001).

[79] K. Koga, T. Ikeshoji, and K. I. Sugawara, Physical Review Letters **92**, 115507 (2004).

[80] R. C. Weast, editor, *CRC Handbook of Chemistry and Physics*, CRC Press, Inc., Boca Raton, FL, 66 edition, 1985.

[81] J. Hone, M. Whitney, C. Piskoti, and A. Zettl, Physical Review B **59**, R2514 LP (1999).

[82] M. A. Osman and D. Srivastava, Nanotechnology **12**, 21 (2001).

[83] E. Pop, D. Mann, Q. Wang, K. Goodson, and H. Dai, Nano Letters **6**, 96 (2006).

[84] N. Mingo and D. Broido, Nano Letters **5**, 1221 (2005).

[85] M. Fujii et al., Physical Review Letters **95**, 065502 (2005).

[86] J. Hone et al., Applied Physics Letters **77**, 666 (2000).

[87] W. Yi, L. Lu, Z. Dian-lin, Z. W. Pan, and S. S. Xie, Physical Review B **59**, R9015 LP (1999).

[88] P. Pawlow, Zeitschrift Fur Physikalische Chemie–Stochiometrie Und Verwandtschaftslehre **65**, 545 (1909).

[89] Y. Chushak and L. Bartell, Journal of Physical Chemistry B **105**, 11605 (2001).

[90] S. Helveg et al., Nature **427**, 426 (2004).

[91] M. Lin et al., Nano Letters **6**, 449 (2006).

[92] R. Sharma and Z. Iqbal, Applied Physics Letters **84**, 990 (2004).

[93] J. A. Rodriguez-Manzo et al., Nature Nanotechnology **2**, 307 (2007).

[94] H. Nakajima and K.-i. Hirano, Journal of Applied Physics **48**, 1793 (1977).

[95] G. E. Begtrup et al., Physical Review Letters **99** (2007).

[96] J. Y. Raty, F. Gygi, and G. Galli, Physical Review Letters **95** (2005).

[97] S. Hong, Current Applied Physics **3**, 457 (2003).

[98] C. P. Deck and K. Vecchio, Carbon **44**, 267 (2006).

[99] S. Hofmann, G. Csanyi, A. C. Ferrari, M. C. Payne, and J. Robertson, Physical Review Letters **95**, 036101 (2005).

[100] V. Deshpande et al., Nano Letters **6**, 1092 (2006).

[101] S. Lee et al., Nano Letters **4**, 2027 (2004).

[102] Y. K. Kwon, D. Tomanek, and S. Iijima, Physical Review Letters **82**, 1470 (1999).

[103] P. Kumar et al., Nature **449**, 894 (2007).

[104] J. Sellers and B. Kachar, Science **249**, 406 (1990).

[105] A. Barreiro et al., Science **320**, 775 (2008).

[106] S. Nishikawa et al., Biochemical and Biophysical Research Communications **290**, 311 (2002).

[107] A. L. Elias et al., Nano Letters **5**, 467 (2005).

[108] T. Muhl et al., Journal of Applied Physics **93**, 7894 (2003).

[109] D. M. Eigler and E. K. Schweizer, Nature **344**, 524 (1990).

[110] J. Darlington, A. Finney, and A. Pearce, Microform and Imaging Review **32**, 113 LP (2003).

[111] A. N. Kolmogorov, V. H. Crespi, M. H. Schleier-Smith, and J. C. Ellenbogen, Physical Review Letters **92**, 085503 (2004).

[112] S. T. Purcell, P. Vincent, C. Journet, and V. T. Binh, Physical Review Letters **89**, 276103 (2002).

[113] K. Jensen, J. Weldon, H. Garcia, and A. Zettl, Nano Letters **7**, 3508 (2007).

[114] T. D. Yuzvinsky, A. M. Fennimore, W. Mickelson, C. Esquivias, and A. Zettl, Applied Physics Letters **86** (2005).

[115] J.-Y. Park, Y. Yaish, M. Brink, S. Rosenblatt, and P. L. McEuen, Applied Physics Letters **80**, 4446 (2002).

[116] J. C. Meyer, C. O. Girit, M. F. Crommie, and A. Zettl, Applied Physics Letters **92** (2008).

[117] J. C. Meyer, C. O. Girit, M. F. Crommie, and A. Zettl, Nature **454**, 319 (2008).

[118] A. M. Fennimore, *Experimental studies of the nanomechanical properties of nanotubes*, PhD thesis, University of California, Berkeley, 2005.

Part IV

Appendices

Appendix A

Microfabrication of Silicon Nitride Membranes

A.1 Introduction

The silicon nitride membrane project was conceived and pioneered by former Zettl graduate student Adam Fennimore. If I have performed great things, it is only that I stand on the shoulders of this fairly short man. The original design and fabrication of the membranes is outlined in Adam's dissertation, "Experimental Studies of the Nanomechanical Properties of Nanotubes,"[118] from which I borrow some of the fabrication descriptions.

The membranes in their current form are impressively versatile and robust. I have often literally dropped membrane devices on the floor without breaking or otherwise damaging them. The simple genius behind their design is the small size ($\sim$10 μm) of the suspended window. This allows stability that is hard to reach with commercial membranes

that are millimeters in width.

The fact that these membranes are stable at high temperatures and compatible with many forms of processing allows great versatility in application. Currently, these membranes have eight electrical contacts of identical material, but they could easily be fitted with varying contacts for superconductivity or magnetic measurements. Additionally, a micro heater or thermometer could be patterned on the window to allow more complex studies of thermal properties. The membranes can also be selectively etched to provide nanoscale pores for fluidic measurements (as is currently being pursued by Tom Yuzvinsky) or for higher resolution of suspended structures. Additionally, the membrane itself could be made of different materials, as was briefly explored with Silicon Dioxide. We have only reached the tip of the iceberg of possibilities for applications of these membranes.

A.2 Design

I will here describe the basic membrane design and fabrication. There are many possible alterations, some of which we have attempted to varying degrees, and some that we have considered but not yet implemented.

The basic membrane structure, when fully fabricated, consists of four important layers, as illustrated in Figure A.1. The substrate is a thin (200 μm) double side polished (DSP) Silicon wafer. On top of that is a layer (few hundred nm thick) of Silicon Dioxide (SiO_2, commonly referred to as 'oxide') that acts as a barrier to electrical breakdown to the Silicon. On top of the oxide is the membrane layer made of silicon nitride (Si_3N_4, commonly referred to as 'nitride'). This layer can vary in thickness with a minimum working thickness

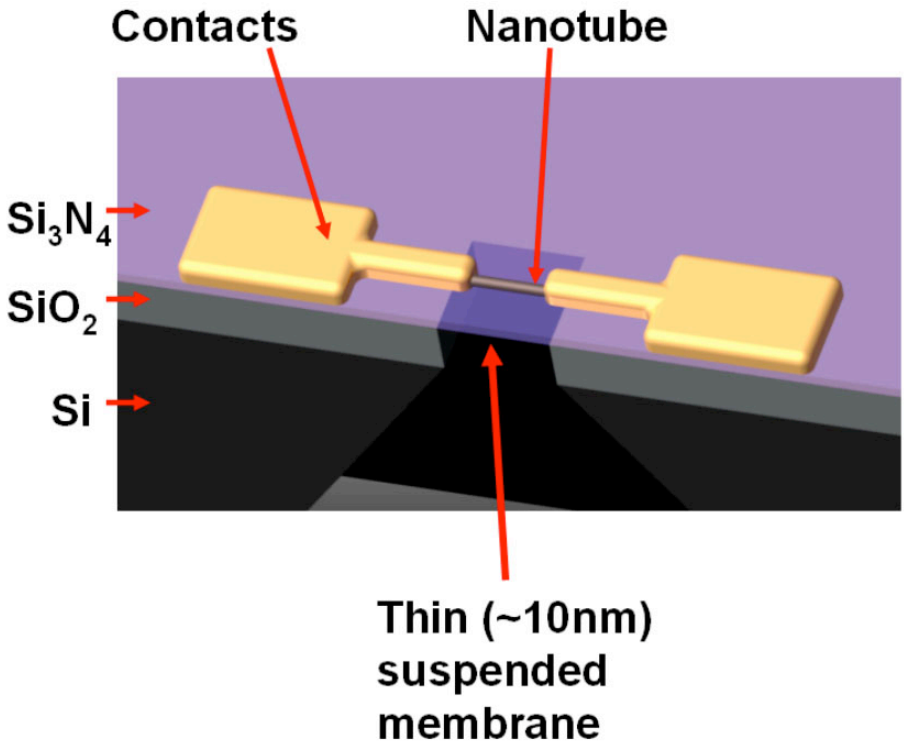

Figure A.1: Artistic Schematic of Silicon Nitride Membrane
A suspended silicon nitride membrane shown with an electrically contacted nanotube device. The supporting Silicon and Silicon Dioxide layers are indicated.

of ∼10 nm. Thinner nitride is preferable for higher resolution imaging in the TEM, but increases risk of membrane failure (typically tearing of the membrane). A thicker membrane (we have used up to 40 nm) can be used when necessary and especially when holes are to be etched in the membrane for maximum resolution. On top of the silicon nitride layer are usually deposited large metal contact pads that can easily be addressed by hand. The silicon nitride membranes are suspended by etching the supporting Silicon and Silicon Dioxide.

A.3 Membrane Fabrication

The simplified version of the membrane fabrication contains four steps and is illustrated in the Figure A.2, which shows a top and side view of the wafer during each step.

Step 1 Grow Oxide and Nitride Layers on Si.

The (100) Si wafer is 200 μm thick, the oxide is typically 200 - 500 nm, and the nitride is typically 10 - 40 nm thick.

Step 2 Pattern and Etch Backside Etch Mask

Step 3 Pattern and Deposit Electrical Contacts on Front Side

Step 4 Etch Through Wafer

A.4 Membrane Recipe

This section contains a step by step recipe for fabricating these membranes, specifically in the Berkeley Microfabrication Laboratory (Microlab, http://microlab.berkeley.edu/). All of the pieces of equipment (italicized in the recipe) in the Microlab requires qualification. Some also require written tests as noted below. This section is designed to allow a knowledgeable Microlab user to produce the membranes in their basic form. Three current members of the Zettl group (Keith Ray, Brian Kessler, and Will Gannett) have been personally trained by me to be able to fabricate these membranes. The process can be completed in as little as three days, but generally takes about a week.

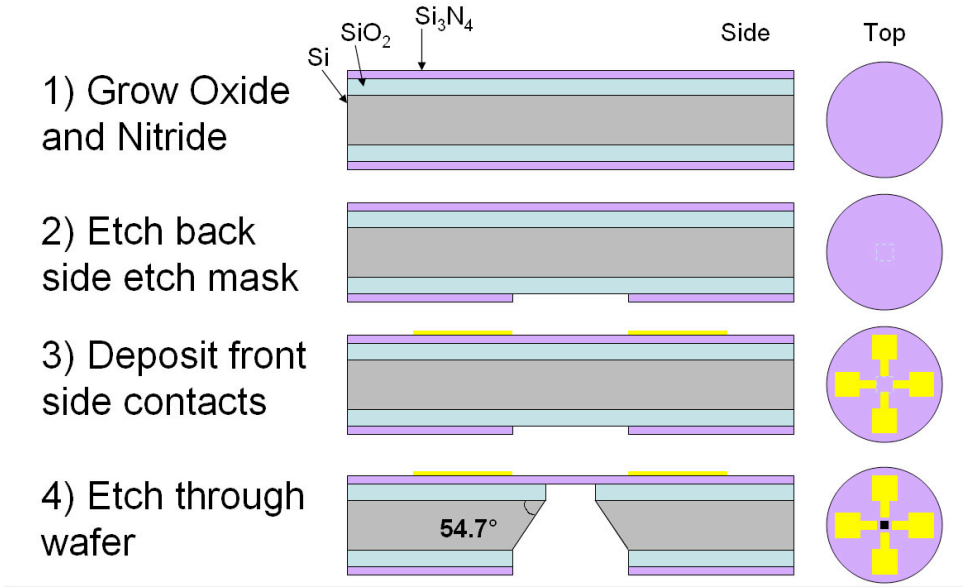

Figure A.2: Four Step Fabrication of Si_3N_4 Membranes

The total equipment necessary or useful to the membrane fabrication process are listed below:

- *Sink6* (requires written test)
- *Tystar2* (requires written test)
- *Tystar9* (requires written test)
- *NanoDUV*
- *OvenVWR*
- *Sink4* or *PrimeOven*
- *SvgCoat*

- *KSaligner* (requires written test)
- *SvgDev*
- *Technics-C* or *Lam2* (requires written test) or *PTherm*
- *Sink5*
- *Sink3*

Be careful while handling the thin wafers and use soft tweezers whenever possible! The wafers are easy to shatter. Also, any scratches incurred will become etch pits during the KOH etch.

A.4.1 Step 0: Substrate Specifications (Silicon Wafer)

For the current fabrication methods, the following are required specifications of the Si wafer.

- 100 mm in diameter
  - This is to allow processing on all the necessary equipment. The Microlab has many 6" pieces of equipment, and the membrane process could be ported to 6" when all the necessary equipment is available.
- 200 μm thick
  - This is required for compatibility of the current etch mask windows and presumably for proper fitting in the TEM biasing stage. One could create a new lithography mask for 500 μm (standard thickness) Si wafers.

  - The thinness of the wafers creates a serious concern for wafer breakage. *Handle the membranes carefully throughout the fabrication process!*

- Double Side Polished (DSP)
- <100> orientation
  - This is required for the anisotropic etch of the Si

The resistivity and other wafer parameters are not important for the membrane fabrication. However, one could use degenerately doped (n++) conducting wafers for electrical measurements.

A.4.2 Step 1: Grow Oxide and Nitride Layers

This step describes the initial growth of the oxide and nitride layers on the Si wafer.

Step 1.1 Clean Wafers (*Sink 6*) - standard process

This step is to remove organics from the wafers to allow them to be used in the MOS clean furnaces.

Follow standard Microlab recipe for Piranha clean, a 20 minute dip in Piranha followed by a DI water rinse and spin dry. This can be followed by a dip in diluted HF to remove any native oxide.

Perform this step on the 200 μm wafers as well as a couple 500 μm dummy wafers to be used as test wafers.

Step 1.2 Oxide Growth (*Tystar2*) - 2wetoxa 00:30:00

Use the standard recipe for 1000°C wet oxide growth, 2wetoxa. The deposition rate can be checked on the process monitor web page and is typically ∼6 nm/min. The standard target thickness of 2000Åis achieved with run time of ∼00:30:00.

Include two clean dummy wafers, one for etch testing and another for thickness measurements. The thickness of the oxide should be measured with the *NanoDUV* on the test wafer, as the growth rate varies from run to run.

If the *Tystar2* is down, the *Tystar1*, generally reserved for dry gate oxide growth, can be used as a backup. *Tystar3* and *Tystar4* are **not** MOS clean and therefore cannot be used if the wafer is then to be used with *Tystar9*.

Step 1.3 Nitride Growth (*Tystar9*) - 9snita 00:02:30

Use the standard stochiometric nitride growth recipe, 9snita. The deposition rate can be checked on the process monitor web page and is typically ∼4 nm/min. The standard target thickness of 100$\mathring{A}$ is achieved with a run time of 00:02:30.

Typically the nitride growth is performed on all wafers from the previous growth. Additionally, include the oxide coated dummy for etch tests and a clean (HF dipped to remove oxide) dummy wafer for measuring the nitride thickness, as it will not be possible to accurately measure the thin nitride thickness on top of the oxide. Measure the nitride thickness on the dummy with the *NanoDUV*.

Alternatively, *Tystar17* can be used as a backup to *Tystar9*. It can be used for stochiometric or low-stress nitride.

A.4.3 Step 2: Create Backside Windows

This step describes the creation of the etch mask that will later be used to suspend the nitride membranes.

Step 2.1 (Optional) Coat with HMDS (*Sink4*) - 2 min

In order to improve photoresist adhesion, the nitride surface is primed with Hexamethyldisilazane (HMDS). First, heat the sample on a hot plate at 120 °C or in *OvenVWR* to remove any residual moisture if the wafers have not come directly out of the tube furnaces. Then follow standard procedure to coat the sample in *Sink4* for 2 minutes. Alternatively, the *PrimeOven* can be used.

Step 2.2 Coat the Wafer Backside (*SvgCoat1,2*) - recipe 1,1

At this point, the two sides of the wafer are identical. The side that is patterned with the etch windows is referred to as the "backside."

Use the standard recipe coat=1, bake=1. This will coat the substrate with OiR 10i (I-Line) photoresist at 4100 RPM with a 60s bake at 90°C, resulting in a thickness of $\sim$1.1 μm.

It is extremely important at this point that you are careful with handling the wafers. The tracks of the *SvgCoat* and *SvgDev* are not gentle and have a propensity for breaking the thin 200 μm wafers. Make sure to warm up the tracks with dummy wafers and run any spare thin wafers to check the alignment of the tracks.

Step 2.3 Expose the Backside Windows (*KSaligner*) - Soft Contact, 100 μm gap, $\sim$92 mJ

Use the mask labeled, "GB Mem April 2007 - Windows." This is the most current window mask with 290 μm windows and wafer alignment marks. When properly etched, these should create ~10 μm suspended membranes. The etch windows are large enough that we need not be concerned about the resolution of the lithography. We therefore use the least invasive contact mode, Soft Contact, with a 100 μm alignment gap (there is no alignment in this first step). Scratches caused by the *KSaligner* will become etch pits during the KOH etch, so be careful when handling.

Be certain to center and straighten the chuck before exposing the wafer. This will save time in aligning the second lithography step.

Check the alignment pins to make sure they are not higher than the thin wafer. If so, they will cause an overcurrent and the *KSaligner* will need to be restarted.

The necessary exposure time varies. Check the lamp power. For a power of 19.1 mW, an exposure time of ~4.8 s is appropriate (~92 mJ). However, the correct exposure time can only be determined by running test wafers.

Step 2.4 Develop the Windows (*SvgDev*) - recipe 1,1

Use the standard recipe of develop=1, bake=1. This will develop the wafer with OPD 4262 developer for 60s and then post-exposure bake (PEB) at 120°C for 60s. If you are not yet certain about the exposure level, skip the PEB by using bake recipe 8. This will make it easier to strip the wafer if you need to redevelop it. Use *Sink5* to strip wafers as necessary. As with *SvgCoat*, be sure to warm up

and test the tracks to reduce the likelihood of breaking a wafer.

Step 2.5 Hard Bake (*OvenVWR*) - 30 minutes

Hard bake the photoresist to increase the resistance to the upcoming RIE etch. Heat at least 30 min at 120°C.

Step 2.6 RIE Etch Windows (*Technics-C*) - SF_6 100W 60s

This etch is designed to remove the backside nitride in order to create a hard mask for the KOH silicon etch. As KOH etches oxide at a reasonable rate, it is not necessary to remove all of the backside oxide. However, if TMAH is to be used for etching the silicon, the backside oxide must be completely removed, as TMAH does not etch oxide.

Use the standard Oxygen Scourge recipe to warm up the system: oxygen plasma at 300 W for 20 - 30 min (51.1 sccm O_2, 300 mTorr). Use the standard Descum recipe to remove any residual scum from the pattern (this could also be performed before hard bake): oxygen plasma 50 W for 1 min (51.1 sccm O_2, 300 mTorr).

Use the standard nitride etch to remove nitride (SF_6 13.0 sccm, He 21.0 sccm). We observe the following etch rates:

100 W	Nitride 50 nm/min Oxide 25 nm/min
200 W	Oxide 50 nm/min
300 W	Oxide 70 nm/min

Table A.1: SF_6 Reactive Ion Etch Rates

To ensure removal of the ∼10 nm nitride layer, etch 30s @ 100 W, then rotate wafer and etch again 30s. Longer etch times can be used to remove the entire oxide layer.

Alternatively, this etch could be performed with the *Lam2* or *PTherm* systems. The *Lam2* has a complicated track loading and unloading system that frequently breaks wafers. I have therefore stopped using it altogether. The *PTherm* could be used, but the etch is extremely uneven across the wafer.

Step 2.7 Remove Residual Resist (*Technics-C* and *Sink5*) - O_2 300 W 7 min

To ensure complete removal of residual resist, use the standard *Technics-C* Resist Ashing recipe: oxygen plasma 300 W 7 min (51.1 sccm O_2, 300 mTorr).

Further cleaning is achieved with a dunk is *Sink5*, which consists of a 80°C PRS-3000 bath. A 20 minute soak may be sufficient, but longer soaks may be required to completely clean the surface. Follow with a DI rinse and spin dry.

A.4.4 Step 3: Create Front Side Contacts

The exposure and patterning of the front side contacts is similar to the backside window. However, backside alignment must be used, and higher resolution is required. Additionally, PEB is skipped in order to make liftoff easier.

Step 3.1 (Optional) Coat with HMDS (*Sink4*) - 2 min

In order to improve photoresist adhesion, the nitride surface is primed with Hexamethyldisilazane (HMDS). First, heat the sample on a hot plate at 120°C or in

OvenVWR to remove any residual moisture if the wafers have not come directly out of the tube furnaces. Then follow standard procedure to coat the sample in *Sink4* for 2 minutes. Alternatively, the *PrimeOven* can be used.

Step 3.2 Coat the Wafer Front Side(*SvgCoat1,2*) - recipe 1,1

Make sure that you load the wafers appropriately to coat the front side, which is the side with no patterning on it.

Use the standard recipe coat=1, bake=1. This will coat the substrate with OiR 10i (I-Line) photoresist at 4100 RPM with a 60s bake at 90°C, resulting in a thickness of $\sim$1.1 μm.

As before, make sure to warm up the tracks with dummy wafers and run any spare thin wafers to check the alignment of the tracks and avoid breaking wafers.

Step 3.3 Expose the Front Side Contacts (*KSaligner*) - Vacuum Contact, 100 μm gap, $\sim$92 mJ

Use the mask labeled, "GB Mem Feb. 2006 - Contacts." This is the most current contacts mask with wafer alignment marks to match the backside windows. This mask has 8 contacts per membrane. Here, unlike with the windows mask, the feature size (specifically the individual membrane alignment marks) is at the resolution limit of the *KSaligner* (2 μm). We therefore use a more intimate contact mode, Vacuum Contact, with a 100 μm alignment gap. Here, especially, care must be taken to avoid scratching the wafer.

Be certain to center and straighten the chuck before starting. This will save time

in the backside alignment.

Check the alignment pins to make sure they are not higher than the thin wafer. If so, they will cause an overcurrent and the *KSaligner* will need to be restarted.

Use backside alignment to align the wafer alignment marks on the contacts mask to the wafer alignment marks etched into the backside of the wafer. Expose with Vacuum Contact. If you have problems with the wafer sticking, use Hard Contact instead. The necessary exposure time varies. Check the lamp power. For a power of 19.1 mW, an exposure time of ∼4.8s is appropriate (∼92 mJ). However, the correct exposure time can only be determined by running test wafers.

If contacts pads are not desired, but individual membrane alignment marks are (e.g. for catalyst patterning and nanotube growth), use the mask labeled "GB Mem April 2007 - Alignment."

Step 3.4 Develop the Contacts (*SvgDev*) - recipe 1,8

Use the standard recipe of develop=1, bake=8. This will develop the wafer with OPD 4262 developer for 60s and then skip the (PEB). As with *SvgCoat*, be sure to warm up and test the tracks to reduce the likelihood of breaking a wafer.

Step 3.5 (Optional) Descum the Contacts (*Technics-C*) - O_2, 50 W, 1 min

Use the standard Descum recipe to remove any residual scum from the pattern in order to make sure there are no organics below the contacts: oxygen plasma 50 W for 1 min (51.1 sccm O_2, 300 mTorr). We have had problems with liftoff that may be attributed to this step.

Step 3.6 Deposition of Contacts

The contact material can be chosen to suit the desired application. Typically, gold or palladium contacts are chosen for their high electrical conductivity. A sticking layer is suggested, typically chromium, is used to order to ensure that the contacts do not peel off of the wafer. The evaporation is typically performed in the Zettl group e-beam evaporator, though depending on the material could also be thermally evaporated (in the Zettl group or the *NRC* or *Veeco*), sputtered (in the Zettl group or the *Randex* or *Edwards*), or e-beam evaporated in the Microlab (*Edwards3eb*). Typical contacts are 1 nm Cr, 30 nm Au. Thicker contacts can be used, especially when wire bonding will be used, as it can punch through thin contacts. However, thinner contact pads mean that the smaller contacts to the nanostructures can be thinner.

Step 3.7 Liftoff

Liftoff is performed in Acetone. Depending on the contact deposition step, this can take from minutes to hours. Thin Cr/Au deposition suggested above will lift off easily. High temperature metals such as Pt and Pd or W will be more difficult. With gentle agitation, the metal contacts should start to peel or 'lift' off of the surface. They can be sprayed with a squirt bottle or syringe, but do not allow the sample to dry. Once dried, the photoresist will be very difficult to remove. If necessary, hot acetone can be used (be mindful of flammability), or the samples can be sonicated (remember that membranes cannot be sonicated once they are suspended). Additionally, liftoff can be accomplished with Piranha,

which consists of 70% sulfuric acid and 30% hydrogen peroxide. (Please note: Piranha is dangerous. Use with proper safety precautions.) The sample is then rinsed in IPA and blow dried.

A.4.5 Step 4: Etch Through Wafer

Step 4.1 Etch Windows (*Sink3*) - 80°C, 2:1 KOH, 5 hrs

Etch the wafers in 80°C 2:1 (by weight) H_2O:KOH. Be sure to use the air bubbler to agitate the liquid. The etch rates of KOH for these parameters are roughly 50 μm/hour for Silicon (100) and 400 nm/hour for Silicon Dioxide. The etch rate of silicon nitride is negligible (which is why we use it as a mask).

To etch through the 200 μm Si and the 200 nm oxide on both sides, we etch for five hours. Slightly overetching is acceptable and will only slightly widen the membranes. Clean the wafers with a DI rinse and carefully blow dry with the N_2 gun. The wafers are done etching when you can easily see from the front side pinpoints of light through with your bare eye.

The membrane wafers are now fabricated and ready to use (Figure A.3). They can be diced down to the desired chip size by hand or with a dicer

Be extremely careful with the wafers as they are now very fragile!

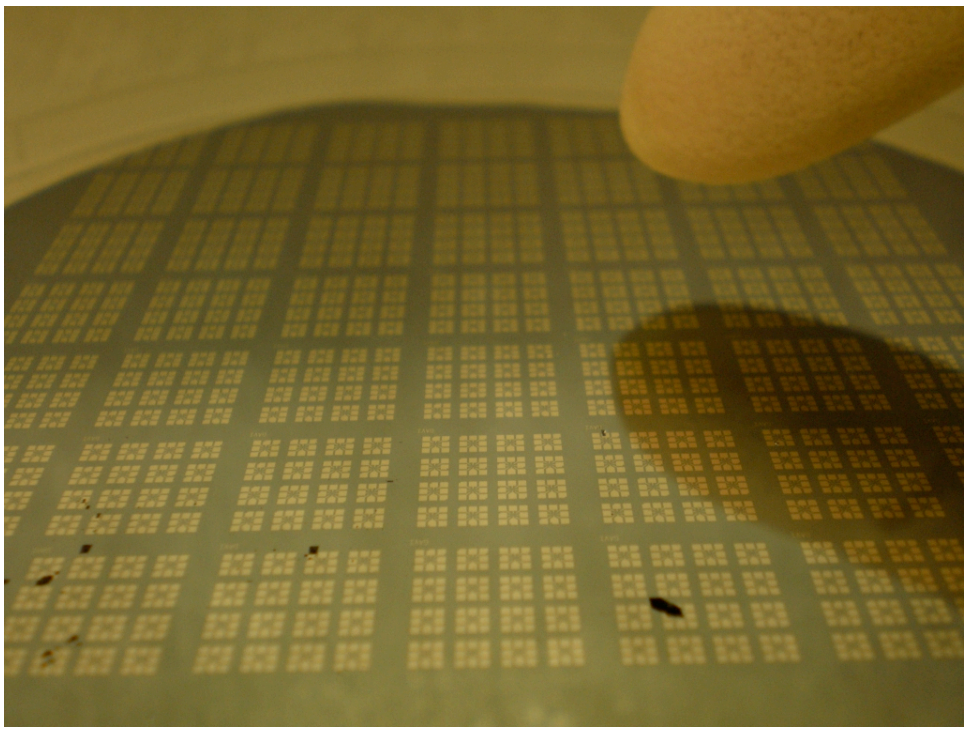

Figure A.3: Wafer of Membranes

A.5 Membrane Fabrication Summary

The following is a quick recap of the fabrication steps that can be used for reference. The accompanying Figure A.4 depicts the stages of the fabrication.

Step 1 - Grow Oxide and Nitride Layers

Step 1.1 Clean Wafers (*Sink 6*) - standard process

Step 1.2 Oxide Growth (*Tystar2*) - 2wetoxa 00:30:00

Step 1.3 Nitride Growth (*Tystar9*) - 9snita 00:02:30

Step 2 - Create Backside Windows

Step 2.1 (Optional) Coat with HMDS (*Sink4*) - 2 min

Step 2.2 Coat the Wafer Backside (*SvgCoat1,2*) - recipe 1,1

Step 2.3 Expose the Backside Windows (*KSaligner*) - Soft Contact, 100 μm gap, $\sim$92 mJ

Step 2.4 Develop the Windows (*SvgDev*) - recipe 1,1

Step 2.5 Hard Bake (*OvenVWR*) - 30 minutes

Step 2.6 RIE Etch Windows (*Technics-C*) - SF_6 100W 60s

Step 2.7 Remove Residual Resist (*Technics-C* and *Sink5*) - O_2 300 W 7 min

Step 3 - Create Front Side Contacts

Step 3.1 (Optional) Coat with HMDS (*Sink4*) - 2 min

Step 3.2 Coat the Wafer Front Side(*SvgCoat1,2*) - recipe 1,1

Step 3.3 Expose the Front Side Contacts (*KSaligner*) - Vacuum Contact, 100 μm gap, $\sim$92 mJ

Step 3.4 Develop the Contacts (*SvgDev*) - recipe 1,8

Step 3.5 (Optional) Descum the Contacts (*Technics-C*) - O_2, 50 W, 1 min

Step 3.6 Deposit Contacts

Step 3.7 Liftoff

Step 4 - Etch Through Wafer

Step 4.1 Etch Windows (*Sink3*) - 80°C, 2:1 KOH, 5 hrs

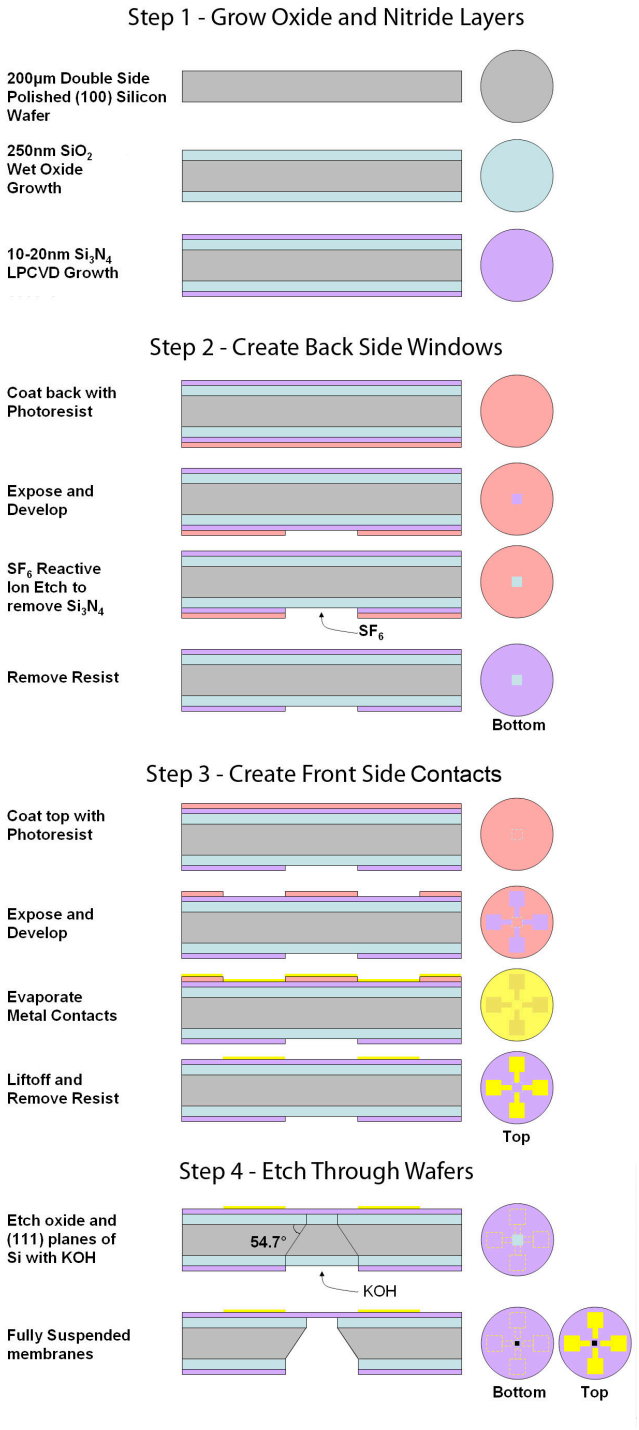

Figure A.4: Membrane Fabrication Summary

A.6 Fabrication Comments

Although it has been suggested that wafer etch could be performed before contacts pads are patterned, this does not work well in practice. The wafers are too fragile at this point to be put through tracks.

This process, in this order, is considerably friendlier than the previous generation of membranes. In the past, the oxide on the backside was etched through in the RIE step and the KOH etch was used only to etch through the silicon, leaving the oxide and nitride on the front side untouched. The oxide was then etched individually for each sample using an HF etch. Unfortunately, HF etch rates are highly uncontrollable, and many of the samples were destroyed during this step. This was particularly distressing when the samples had been through additional fabrication steps. Newer membranes that I made were more robust and could better withstand the HF etch (the etch rate for nitride should be slow). However, this method should be avoided.

Using the KOH to etch through the oxide as well as the silicon, as I suggest in this recipe, is a seemingly obvious solution. However, it was not immediately obvious since oxide is often used as a hard mask for a KOH etch in that the etch rate of oxide in KOH is two orders of magnitude slower than that of Si. However, the etch times for Si and oxide for our membranes is comparable, since the oxide layer is significantly thin compared to the Si wafer. Albeit a slight advance, this change in the recipe made the membranes much more robust and reliable.

It has been my experience that the higher risk steps should be as early in a process as possible, whether in microfabrication or elsewhere. It is much more distressing to have

a sample that has been through days or weeks of processing fail in the final step before the experiment than to have things break only hours in. If there is one lesson I wish to convey to the younger students, it is this.

Appendix B

Device Fabrication

B.1 Introduction

The membranes are incredibly robust and versatile. My hope is that the number of projects heretofore completed is soon eclipsed by the many new applications of this adaptable platform. In this Appendix I describe the fabrication of individual devices, including some details of nanotube synthesis.

B.2 Nanotube Synthesis

As mentioned in the introduction to this dissertation, there are multiple approaches to nanotube synthesis. The choice of approach is in large part due to the desired product. CVD techniques can produce a variety of nanotubes, including ultralong SWCNTs, MWCNTs of various wall number and thicknesses, and filled nanotubes. However, arc discharge can produce high purity MWCNTs without a catalyst.

B.2.1 Arc Discharge Synthesis of MWCNTs

For the study of the breakdown properties of MWCNTs, the highest purity nanotubes are desired. We therefore chose to use arc discharge nanotubes. The nanotubes used in Chapter 5 were from a batch labeled 'HG17,' produced by Henry Garcia. The synthesis was performed in a Helium/Hydrogen mixture with a graphite rod without catalyst. The arc was stable for 16 minutes without extinguishing. The growth parameters are as follows:

Current (A): 75
Average voltage (V): 26
Voltage range (V): 25-27
Initial pressure (mTorr): 150
He pressure (inHg): 17.5
H pressure (inHg): 2.5
Final pressure (inHg): -9.0
Growth Time: 16 minutes

B.2.2 Synthesis of Iron Encapsulated MWCNTs

Iron nanoparticle encapsulated MWCNTs were synthesized with a simple CVD process, the pyrolysis of ferrocene. I personally synthesized the nanotubes used for the studies described in Chapters 6 and 7.

Ferrocene ($C_{10}H_{10}Fe$) is a member of a group of chemicals known as metallocenes, a type of organometallic chemical consisting of a metal atom sandwiched between two cyclopentadienyl rings. As ferrocene sublimes easily, contains carbon, and contains a transition metal that is a good catalyst for nanotubes (iron), it is a suitable choice for nanotube synthesis. The large ratio of iron to carbon causes the resultant nanotubes to contain large amounts of iron.

The synthesis is very simple. Ferrocene powder is loaded into a quartz tube in a

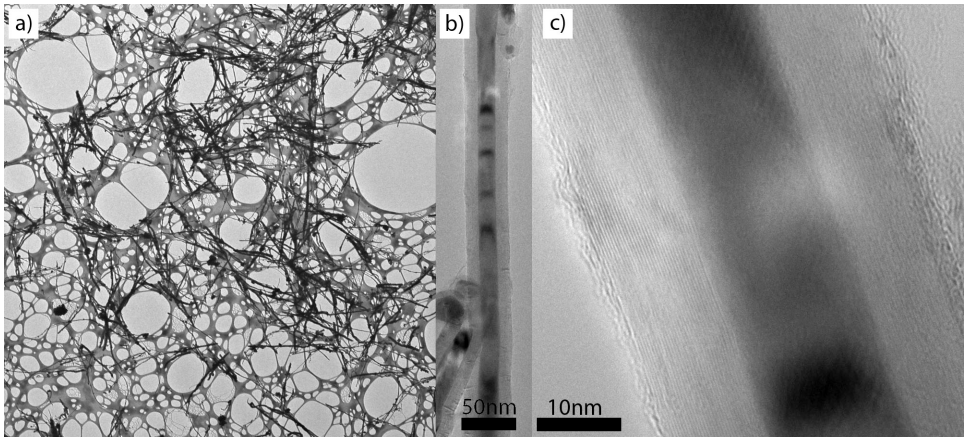

Figure B.1: Iron Filled MWCNTs Grown Via Pyrolysis of Ferrocene
TEM images with successively higher magnification. Individual nanotube walls can be seen in (c)

tube furnace and is then heated to 900 - 1000 °C under flow of an inert gas, such as argon. A mixture of argon and hydrogen can be used to reduce oxidation caused by moisture in the gasses. The subliming ferrocene creates a plume of interesting colors that can be observed before the downstream of the quartz tube becomes coated in black. The entire synthesis is over in minutes, and the resulting mass of black scraped from the quartz tube contains large quantities of iron filled nanotubes, shown in Figure B.1.

Low reaction temperature produces many carbonaceous products. Therefore, it is sometimes advantageous to heat the furnace to the reaction temperature and then introduce the ferrocene by either sliding the hot tube or moving an internal boat containing the ferrocene. A two zone furnace (or inside and outside the hot zone of a single zone furnace) can be used such that the ferrocene in the cooler zone sublimes and is carried in gas phase to the reaction zone.

To adjust the properties of the product, additional carbon can be supplied to the

reaction via organic gases, such as methane or ethylene. This could be used to try and decrease the amount and size of Fe nanoparticles encapsulated in the nanotubes. It also may change the diameter of the nanotubes, which are typically quite large.

Instead of collecting the product on the side of the quartz tube, substrates can be placed downwind of the reaction to collect the nanotubes. Additional catalyst can be introduced in the form of a thin (<10Å) layer of Fe on a Si substrate, which has been explored to some extent by Benji Alemán in the Zettl group.

We have not fully explored the parameter space of this reaction because the simplest of approaches yields nanotubes worthy of many experiments.

B.3 Wiring Up an Individual Nanostructure

This section describes the basic e-beam lithography (EBL) process of patterning electrical contacts on individual nanostructures, specifically on membranes, as performed in the majority of our experiments.

On a membrane wafer are 49 (7x7) square chips spaced 10060 μm apart. This distance was chosen to be compatible with the *GCaws6* wafer stepper, in case integration was required in the future. Each ∼1 cm chip contains a 4x4 square array of individual membranes spaced 2200 μm apart. Each membrane on the wafer is individually labeled with two sets of numbers located to the left and right of the membrane. The number to the left indicates the chip number and is shared by all the membranes on a 4x4 chip. This number is determined by the row and column of the chip in the 7x7 array. The number on the right indicates the location of the membrane within the 4x4 chip, in row column

format. This is individual for each membrane on a chip, but is shared by 49 membranes on the wafer. Together, these four numbers comprise an individual identifier for each of the 784 membranes on a wafer. Be careful, however, because membranes from different wafers may share the same identifier.

The specific steps are for processing a 4x4 chip. A 2x2 chip (a quarter of a 4x4 chip) is the smallest chip easily patterned. The device fabrication is illustrated shown in Figure B.2. The resists used are available from MicroChem. The fabrication steps are:

Step 1 Map the Nanostructures

Map the position of the nanostructures with respect to the individual membrane alignment marks using the SEM. NPGS allows automation of mapping with a simple 3+ point alignment. Use nanostructures near those to be contacted for focusing and alignment. Make sure that the membranes are correctly oriented and as horizontally aligned as possible. Use "Align Feature" to minimize rotation errors by aligning the top edge of the top left and top right contact (11 and 14) by moving from 6600 μm to the right. A map file exists to easily map membranes. By convention, images are numbered from left to right, top to bottom, starting with 11 (the top left membrane). The best imaging parameters must be determined for each nanostructure by experimentation. For MWCNTs, 1 keV spot 3 works well. Higher energy (5 keV spot 3) is used for mapping iron encapsulated within MWCNTs.

Step 2 Design the Contacts

Design contacts with DesignCad. Templates exist for the membranes. Typically, spot 1 is used to contact the individual nanostructures, and spot 2 is used for the connection of these contacts to the large contact pads. Designing contacts is a laborious task and is best relegated to a young grad student or undergrad.

Step 3 Spincoat E-beam Resist

Typically a bilayer is used to promote liftoff. For sufficiently thin depositions, this may not be necessary. Spincoat a copolymer MMA (8.5) MMA EL6 (6% in Ethyl Lactate) at 3000 RPM for >30s, producing a layer of thickness ∼120 nm. Bake at 185°C for 3 min. Spincoat top e-beam resist PMMA A4 (4% in Anisole) at 3000 RPM for >30s, producing a layer of thickness ∼250 nm. Bake at 185°C for 3 min. Deposit drops of colloidal gold (20 nm) on corners of the chip to facilitate focusing.

Step 4 Pattern the Contacts

NPGS allows the entire 4x4 array to be patterned automatically with a 3+ point alignment. Use the colloidal gold at the corners of the device for focus alignment. Perform a feature alignment using the tops of the 11 and 14 contact (spaced 6600 μm apart). Perform a global rotation correction using the top left corners of 11, 14 (6600,0), and 44 (6600,-6600). Template run files for the membranes have a start location in the top left corner of the top left contact (11). Typical dosage is ∼300 C/cm^2 but should be checked depending on application. Typically 30 keV spots 1 and 2 are used for membrane devices. Higher spots can be used for larger features but require frequent alignment. Check spot currents with the faraday cup

to ensure proper exposure. I have written a program integrated into NPGS that allows you to enter the new spot currents and update your run files.

Step 5 Develop the Resist

Soak chip in MIBK:IPA 1:3 for 2 minutes. This long development time is used because I am usually more concerned with underdeveloping than overdeveloping. For high resolution patterning, the development time can be carefully controlled and the solution can be held at a fixed temperature in a bath. Rinse chip thoroughly in IPA and blow dry.

Step 6 Deposit Contact Layer

This is typically performed in our Thermionics e-beam evaporator, but can be done elsewhere. Typically no adhesion layer is needed. The best contact to nanostructures is widely debated, as is the best evaporation parameters. For nanotubes, we find that Pd makes very good contacts. Keep in mind, the thickness of these contacts must be greater than the thickness of the large contact pads. Otherwise shadowing effects may cause disconnects.

Step 7 Liftoff the contacts

In the past we have used acetone for liftoff. However, we are now switching to NMP, which produces cleaner liftoff. Soak the sample in 65 °C for as long as necessary. When care is taken to not overheat the resist (which can easily happen when evaporating high temperature metals such as Pt), the liftoff will be completed within minutes. It is best to gently agitate the sample periodically and leave the

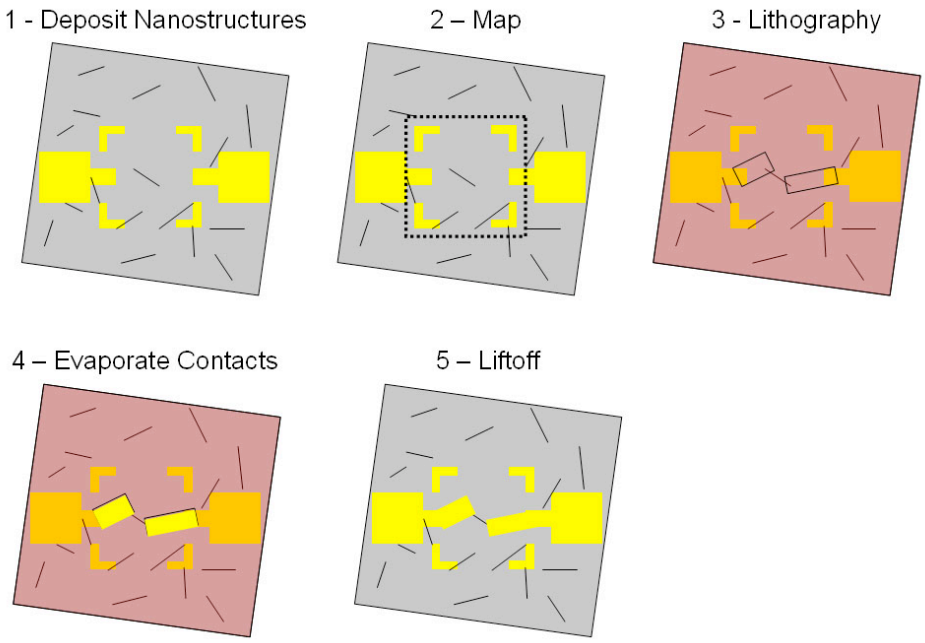

Figure B.2: Fabrication of an Individual Nanotube Device

liftoff overnight. Liftoff can be assisted by spraying. *Do NOT sonicate*, as this will destroy the membranes. When complete, rinse in IPA and blow dry.